Radboud Repository

Radboud University Nijmegen

PDF hosted at the Radboud Repository of the Radboud University Nijmegen

The following full text is a publisher's version.

For additional information about this publication click this link.
http://hdl.handle.net/2066/18670

Please be advised that this information was generated on 2017-12-05 and may be subject to change.

Nonlinear optical study of ultrafast carrier dynamics in GaAs

ISBN 90-9012311-3

Druk: Ponsen & Looijen BV, Wageningen

Nonlinear optical study of ultrafast carrier dynamics in GaAs

een wetenschappelijke proeve op het gebied van
de Natuurwetenschappen, Wiskunde en Informatica

Proefschrift

ter verkrijging van de graad van doctor aan
de Katholieke Universiteit Nijmegen,
volgens besluit van het College van Decanen
in het openbaar te verdedigen op
donderdag 21 januari 1999,
des namiddags om 3.30 uur precies

door

Willem de Jong

geboren op 28 oktober 1969
te Stolwijk

Promotor : prof. dr. Th.H.M. Rasing
Co-promotor : dr. P.J. van Hall,
Technische Universiteit Eindhoven

Manuscriptcommissie:
prof. dr. M. Aeschlimann University of Essen, Germany
prof. dr. ir. J.C. Maan

Het werk beschreven in dit proefschrift maakt deel uit van het onderzoeksprogramma van de Stichting voor Fundamenteel Onderzoek der Materie (FOM) en is mede mogelijk gemaakt door financiële steun van de Nederlandse Organisatie voor Wetenschappelijk Onderzoek (NWO).

Aan Rieneke
Aan mijn moeder

Voorwoord

Het voorwoord mag dan voorin een proefschrift staan, het is meestal het onderdeel dat het laatst wordt geschreven en biedt dus een prima gelegenheid om terug te kijken. Op het moment dat dit proefschrift verschijnt is het zes jaar geleden dat ik voor het eerst kennis maakte met de groep EVSF-II. Als student die op zoek is naar een promotieplaats, ontmoet je dan de mensen die, volgens mij, vooral verantwoordelijk zijn voor het reilen en zeilen van een vakgroep. Riki, Herman en Theo, hartelijk bedankt dat jullie mij de mogelijkheden boden om onderzoek te doen. Niet alleen toen ik solliciteerde, maar ook gedurende de vier jaren die daar op volgden. Vanaf het moment dat ik daadwerkelijk in dienst trad hebben Albert en Adriaan geprobeerd mij vertrouwd te maken met lasers. Of dat gelukt is mogen zijzelf beoordelen. In ieder geval waren zij onmisbaar om op de juiste momenten steeds kortere pulsen uit de laser te krijgen. Naast optica deskundigen, waar je alle mogelijke spiegeltjes en lenzen van kunt lenen, heb je voor het slagen van een onderzoek ook nog andere specialisten nodig. Het te bestuderen sample moest bijvoorbeeld netjes kunnen roteren. De andere technici in de groep en de mensen van de werkplaats hebben veel nuttige adviezen en noodzakelijk werk geleverd.

Voor de samples hebben mensen uit de halfgeleidergroep van professor Wolter aan de TU Eindhoven gezorgd. Willem van der Vleuten, die dit helaas niet meer kan lezen, groeide de gewenste lagen GaAs en AlGaAs. Peter Nouwen en Kees van Es dampten een goudlaagje op en maakten er draadjes aan zodat het soms, maar soms ook niet, een werkend Schottky barrière sample werd.

Degenen die mij, naast Theo, wegwijs gemaakt hebben op het gebied van tweede harmonische generatie zijn Harald en Kees. Omdat zij ook gedurende korte, respectievelijk erg lange, tijd mijn kamergenoten waren heb ik hen ook in die hoedanigheid leren kennen en niet alleen fysica van hen geleerd. Bij die kamergenoten horen natuurlijk ook nog Maurice en Lieve die ons gezeur over bijvoorbeeld jonge promovendi die niets kunnen of over het correct gebruik der Nederlandse taal moesten aanhoren. Ik hoop dat het niet al te vervelend was.

Als, na lang ploeteren, het experiment uiteindelijk resultaten oplevert is de interpretatie natuurlijk niet direkt duidelijk. Ondanks het feit dat Theo het altijd druk heeft vindt hij altijd wel tijd om over de resultaten en de nieuwe vragen te praten en komt hij meestal met nieuwe ideeën. Theo, je enthousiasme voor de fysica werkt aanstekelijk. Ik heb daarvan in ieder geval geleerd dat je de resultaten ook enthousiast moet verkopen. Pieter van Hall zei na iedere verbetering aan het simulatiemodel dat het nu wel mooi genoeg was en dat hij er niet meer aan ging sleutelen. Als er dan weer nieuwe meetresultaten waren die er toch iets anders uitzagen ging hij meestal toch weer verfijningen aanbrengen, met als resultaat dat het model de werkelijkheid nu een stuk nauwkeuriger beschrijft. Pieter, ik denk met plezier terug aan de vele discussies over de dynamica van ladingsdragers, andere interessante fysica, en vele niet-natuurkundige onderwerpen. Daarnaast zijn er nog veel meer mensen die een nuttige bijdrage geleverd hebben aan het onderzoek, maar die zal ik hier niet allemaal met name noemen.

Ook tijdens het tot stand komen van dit boekje hebben meerdere mensen een onmisbare bijdrage geleverd. Wilma zag heel wat keren haar mailbox vollopen met weer een stuk tekst wat ze dan geacht werd te printen en aan Theo te overhandigen. Theo en Pieter hebben meerdere versies kritisch doorgelezen en uitgebreid van aanwijzingen en suggesties voorzien. De leden van de manuscriptcommissie wil ik bedanken voor hun commentaar. Mijn huidige werkgever dank ik voor de materiële bijdrage.

Niet direkt terug te vinden in dit boekje, maar niet minder belangrijk, is de bijdrage van mensen die niet iets met natuurkunde te maken hebben. Ik kan niet iedereen noemen, maar allereerst wil ik mijn moeder bedanken dat ze me de mogelijkheid heeft gegeven om een studie te volgen, waardoor ik dit onderzoek heb kunnen doen. Vooral Rieneke zal heel blij zijn als het boekje eindelijk gedrukt is. Ze heeft heel wat avonden alleen gezeten omdat ik aan het meten was, of omdat ik aan mijn proefschrift wilde werken. Henriette hoeft nu ook niet meer te vragen of pappa netjes z'n poefschift af gaat maken. En Marijn snapt er nog helemaal niets van. Maar hij maakt wel duidelijk dat er gelukkig meer is in het leven dan natuurkunde. Mede hierdoor is dit werkstuk iets minder vlot voltooid dan theoretisch mogelijk zou zijn.

Wim de Jong
18 november 1998

Contents

Chapter 1

Introduction

Light has been used for communication since a long time. Sailors, for example, observed (and they still do) the flashes from the lighthouses along the coast to determine their position. Nowadays optical fibers are used for the main telephone connections instead of copper wires. A large difference between these two modes of optical communication is the frequency of the light flashes. The frequency of the lighthouse is of the order of one Hertz, while in optical fibers a frequency of the order of 1 MHz (1,000,000 Hz) is used. Optical communication via glass fiber cables has been made possible by the invention of light emitting diodes which can make the short light pulses necessary to reach the high frequencies. These diodes are made from semiconducting materials like Gallium Arsenide (GaAs). This GaAs has a direct bandgap which makes the material very useful for opto-electronic applications like optical switches and optical detectors. Since not only people communicate via telephone wires, but also computers, the transmission speed is an important issue. In the future this speed could be increased to frequencies of about a Tera Hertz (1 THz = 1,000,000 MHz).

When a thin transparent metal layer is evaporated on the GaAs surface a potential barrier is formed due to the difference in the Fermi levels of the metal and the semiconductor. Such a metal semiconductor contact has rectify-ing properties and is called a Schottky Barrier. A structure like this was the first diode, developed in 1948, for which Bardeen[1], Brattain and Shockley got a Nobel prize. Behind the metal semiconductor interface an electric field exists which varies from about 300 kV/cm at the interface to zero at a distance of about 300 nano meter (1 nm = 10^{-9} m) from the interface. When incident light is absorbed by the material, electrons are excited from the valence band to the conduction band. In the electric field the charge carriers, electrons and holes, are accelerated and will subsequently influence the electric field they move in.

If the intensity of the light is high enough, the density of excited charge carriers can reach values of 10^{18} per cubic centimeter. At these high densities the charge carriers can start oscillating, the so called plasma oscillations. These oscillations

---

[1] Bardeen is also well known from the BCS theory, that describes superconductivity.

have frequencies in the THz regime. Some of the lattice vibrations in GaAs, the optical phonons, have frequencies of the same order of magnitude and coupled plasma-phonon oscillations can be expected [1]. This coupling could drastically influence the behavior of a device.

The development of lasers which can produce light pulses with a duration of only 50 femto second (1 fs = 10^{-15} s) and a wavelength which is tunable from visible to infrared wavelengths, has revolutionized the opportunities for study of the above mentioned ultrafast dynamics in semiconductors. In time resolved experiments two or more light pulses are used with a time delay between them which is controlled carefully. In general the first pulse, the pump, makes an excitation and the second pulse, the probe, measures the effect. By changing the delay between the two pulses the time dependence of the effect can be measured on a femto second time scale.

The generation of coherent excitations in semiconductors like phonons have been extensively studied in recent years [2–4], partly due to promising applications as sources for coherent THz radiation [5]. Bulk plasmon-phonon modes have been studied by Cho *et al* [6] using a femto second electro-optical sampling technique, whereas Sha *et al* [3] have directly observed pure bulk plasma oscillations. Fischler *et al* [4] have found indications for plasma oscillations in transient reflectivity measurements on GaAs photo diodes.

In photo luminescence (PL) experiments charge carriers are excited in the semiconductor by a pump beam. After relaxation the electrons recombine with the holes in the valence band and emit a photon which can be measured. Time resolved PL experiments performed previously on a biased Schottky barrier sample showed a PL signal with an unexpectedly long decay time [7]. With the use of simulations this long time could be explained as the result of the instantaneous collapse, due to excited carriers, and subsequent recovery of the electric field behind the Schottky barrier interface. These simulations also predicted the possible occurrence of plasma oscillations, as have already been observed in bulk semiconductors [3]. However PL experiments probe this interface electric field in quite an indirect way, since the signal is integrated over a finite volume.

A more suitable method for measuring the electric field at the interface is the non-linear optical technique of second harmonic generation (SHG). When a light beam is reflected by a medium, the reflected light has in general the same wavelength as the incident beam. This is the linear case. At high light intensities however, as is the case with pulsed lasers, also light with a double frequency is generated and reflected by some media. This light is the second harmonic of the fundamental light which is incident on the medium. In media which are centro symmetric no second harmonic light is generated. At surfaces and interfaces of these media however the symmetry is broken and second harmonic light can be generated. Optical second harmonic generation has already been shown to be an effective method of probing the structure and symmetry of interface layers [8–13]. The surface c.q. interface sensitivity in those situations is based on the symmetry breaking at interfaces and the SHG-intensity is found to be strongly dependent on surface orientation, defect generation, adsorption, and so on. Since GaAs is not centro symmetric, bulk contributions to the SHG-intensity exist.

However also in GaAs, interfaces lower the symmetry further and can thus give extra, separable, contributions to the SHG-intensity. An electric field normal to an interface also breaks the symmetry. Qi *et al* [14] showed the capability of SHG to probe the band bending region of GaAs, using a tunable excitation source. Lantz *et al* [15] used SHG to probe the electrostatic fields at TiO_2 electrodes. This process is the so called electric field induced second harmonic generation (EFISHG). An advantage of such an optical method is the possibility of probing the electric field at buried interfaces, such as the metal semiconductor interface of a Schottky barrier sample.

1.1 Outline of this thesis

In this thesis we will report on SHG and EFISHG studies performed on Au-GaAs and Au-AlGaAs Schottky barrier (SB) systems. The most interesting are the dynamics of excited carriers behind the Schottky barrier interface which are happening on a femto second time scale.

Chapter 2 starts with a description of the Schottky barrier samples which have been used for the SHG measurements. In this chapter also the SHG setup is described which has been used to probe the electric field behind the Schottky barrier interface with a high time resolution.

Chapter 3 gives some basic theory concerning the time resolved SHG experiments. In the first section the metal semiconductor interface is described. The second section gives some brief information about the dynamics of charge carriers in GaAs and the Monte Carlo simulations which have been performed for a better understanding of the experiments. The third section offers a more detailed description of second harmonic generation and the detectability of a static electric field with this technique. The derivation of the tensor elements which play a role in the second harmonic generation process is discussed in Appendix A.

Chapter 4 gives the results of anisotropy measurements. These measurements, which are not time resolved, have been performed to determine how the SHG signal depends on the electric field behind the interface. The wavelength, the pulse width and the intensity of the probe beam have been varied to check their influences on the detectability of the electric field dynamics inside the semiconductor. The results have been used to determine the optimal experimental conditions for the time resolved SHG measurements which will be presented in the chapters 5 and 6.

In the last two chapters we discuss the time resolved experiments. Chapter 5 shows results of time resolved pump probe experiments at relatively low excitation intensities. These measurements have been performed with different sizes of the laser spot on the sample to check the influence on the recovery of the electric field after excitation. This influence is incorporated in the simulations via a recovery time constant which depends on the spot size.

The last chapter, chapter 6, describes the results for pump probe experiments at high excitation intensities. Under these conditions the expected plasma oscillations have been observed directly in the time domain. These oscillations have THz frequencies and couple to the LO-phonon oscillations. The simulations offer a very good description of the dynamical behavior of the electric field that has been observed experimentally, provided the plasmon phonon coupling is included. In these simulations the only adjustable parameter is the recovery time constant which was determined with the experiments described in chapter 5.

References

[1] A. Mooradian and A. L. McWhorter. Polarization and intensity of Raman scattering from plasmons and phonons in gallium arsenide. *Phys. Rev. Lett.*, **19**, 849–852, (1967).

[2] G. C. Cho, W. Kütt, and H. Kurz. Subpicosecond time-resolved coherent-phonon oscillations in GaAs. *Phys. Rev. Lett.*, **65**, 764–766, (1990).

[3] W. Sha, A. L. Smirl, and W. F. Tseng. Coherent plasma oscillations in bulk semiconductors. *Phys. Rev. Lett.*, **74**, 4273–4276, (1995).

[4] W. Fischler, P. Buchberger, R. A. Höpfel, and G. Zandler. Ultrafast reflectivity changes in photoexcited GaAs Schottky diodes. *Appl. Phys. Lett.*, **68**, 2778–2780, (1996).

[5] H. G. Roskos *et al.* Coherent submillimeter-wave emission from charge oscillations in a double-well potential. *Phys. Rev. Lett.*, **68**, 2216–2219, (1992).

[6] G. C. Cho *et al.* Generation and relaxation of coherent majority plasmons. *Phys. Rev. Lett.*, **77**, 4062–4065, (1996).

[7] P. C. M. Christianen *et al.* Ultrafast carrier dynamics at a metal-semiconductor interface. *J. Appl. Phys.*, **80**, 6831–6838, (1996).

[8] Y. R. Shen. Surface properties probed by second harmonic and sum frequency generation. *Nature*, **337**, 519–525, (1989).

[9] G. L. Richmond, J. M. Robinson, and V. L. Shannon. Second harmonic generation studies of interfacial structure and dynamics. *Progr. Surf. Sci.*, **28**, 1–70, (1988).

[10] H. W. K. Tom, T. F. Heinz, and Y. R. Shen. Second-harmonic reflection from silicon surfaces and its relation to structural symmetry. *Phys. Rev. Lett.*, **51**, 1983–1986, (1983).

[11] S. V. Govorkov *et al.* Inhomogeneous deformation of silicon surface layers probed by second-harmonic generation in reflection. *J. Opt. Soc. B*, **6**, 1117–1124, (1989).

[12] M. A. Verheijen, C. W. van Hasselt, and Th. Rasing. Optical second harmonic generation study of vicinal Si(111) surfaces. *Surf. Sci.*, **251-252**, 467–471, (1991).

[13] G. G. Malliaras, H. A. Wierenga, and Th. Rasing. Study of the step structure of vicinal Si(110) surfaces using optical second harmonic generation. *Surf. Sci.*, **287-288**, 703–707, (1993).

[14] J. Qi *et al.* Depletion-electric-field-induced changes in second-harmonic generation from GaAs. *Phys. Rev. Lett.*, **71**, 633–636, (1993).

[15] J. M. Lantz and R. M. Corn. Electrostatic field measurements and band flattening during electron-transfer processes at single-crystal TiO_2 electrodes by electric field-induced optical second harmonic generation. *J. Phys. Chem.*, **98**, 4899–4905, (1994).

Chapter 2

Experimental

This chapter describes the Schottky barrier (SB) samples and the experimental setup. With this setup the nonlinear optical experiments, namely optical second harmonic generation (SHG), have been performed to probe the electric field dynamics in the samples. The laser source, the signal detection and the different setups which have been used for these SHG experiments are described in this chapter. Before doing so we start in section 2.1 with a description of the layer composition of the different Schottky barrier samples which have been used in the experiments.

2.1 Sample composition

The Schottky barrier samples have been made from the semiconductor material Gallium Arsenide (GaAs), since this semiconductor has a direct bandgap (see figure 3.2), which makes it very useful for optical experiments. Three different kind of samples have been studied, they are shown schematically in figure 2.1. These samples have been grown with molecular beam epitaxy on a n^+ GaAs(100) substrate at the Eindhoven University of Technology. On the substrate first a heavily doped n-type superlattice buffer layer has been grown, to avoid the growth of dislocations into the actual barrier layer. In the first two samples the Schottky barrier is formed by a 300 nm-thick n-type GaAs layer and a gold film. The semi-transparent gold film has a thickness of only 10 nm to allow for laser excitation through this metal top contact. In the third sample the 300 nm-thick GaAs layer is replaced by a 4 μm-thick n-type $\mathrm{Al}_{.2}\mathrm{Ga}_{.8}\mathrm{As}$ layer. The main difference between sample 3 and the other two is the size of the direct bandgap, 1.66 eV for sample 3 versus 1.42 eV for the samples 1 and 2.

The first sample has a very thin (10 nm) intermediate undoped $\mathrm{Al}_{.4}\mathrm{Ga}_{.6}\mathrm{As}-$layer between the metal and the depletion layer, capped by a 10 nm-thick undoped GaAs-layer to avoid oxidation of the $\mathrm{Al}_{.4}\mathrm{Ga}_{.6}\mathrm{As}-$ layer. This sample is identical to the ones which have been used for the photo luminescence experiments performed by Christianen [1–3]. In these experiments a cap layer was necessary. However for SHG

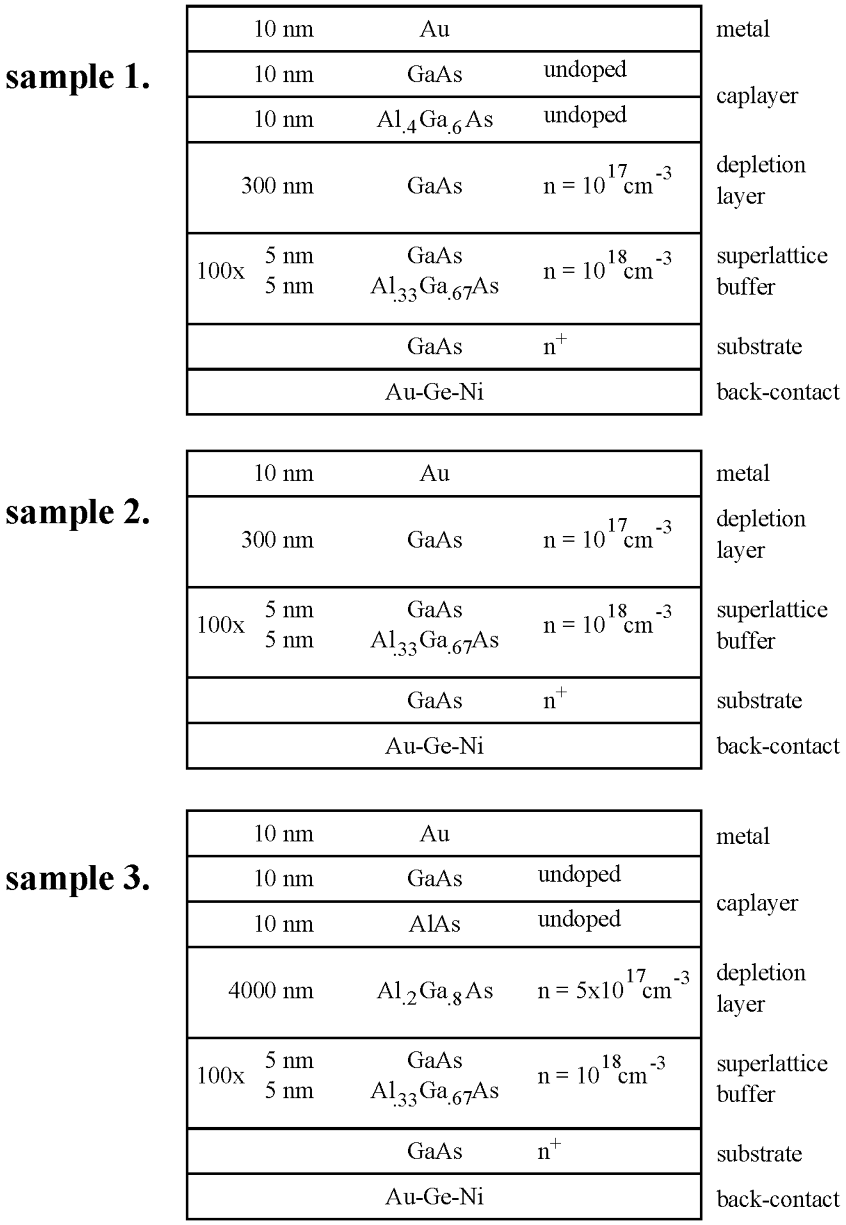

sample 1.

10 nm	Au		metal
10 nm	GaAs	undoped	caplayer
10 nm	$Al_{.4}Ga_{.6}As$	undoped	
300 nm	GaAs	$n = 10^{17} cm^{-3}$	depletion layer
100x 5 nm 5 nm	GaAs $Al_{.33}Ga_{.67}As$	$n = 10^{18} cm^{-3}$	superlattice buffer
	GaAs	n^+	substrate
	Au-Ge-Ni		back-contact

sample 2.

10 nm	Au		metal
300 nm	GaAs	$n = 10^{17} cm^{-3}$	depletion layer
100x 5 nm 5 nm	GaAs $Al_{.33}Ga_{.67}As$	$n = 10^{18} cm^{-3}$	superlattice buffer
	GaAs	n^+	substrate
	Au-Ge-Ni		back-contact

sample 3.

10 nm	Au		metal
10 nm	GaAs	undoped	caplayer
10 nm	AlAs	undoped	
4000 nm	$Al_{.2}Ga_{.8}As$	$n = 5x10^{17} cm^{-3}$	depletion layer
100x 5 nm 5 nm	GaAs $Al_{.33}Ga_{.67}As$	$n = 10^{18} cm^{-3}$	superlattice buffer
	GaAs	n^+	substrate
	Au-Ge-Ni		back-contact

Figure 2.1: Layer composition of the three different Schottky barrier samples. The doping concentration is written in the layers. The superlattice buffer consists of 100 alternating GaAs $Al_{.33}Ga_{.67}As$ layers.

such a cap layer is not needed and it is thus omitted in sample 2. Sample 3 is capped by a 10 nm-thick undoped GaAs-layer and a (10 nm) intermediate undoped AlAs-layer.

To manipulate the static electric field behind the SB interface (the so called depletion layer) a variable voltage bias can be applied across the samples between a AuGeNi backside-contact and the Au top contact. Capacitance-voltage measurements indicate a value for the Schottky barrier height of 0.90 V, which is a normal value for Schottky Barriers formed on GaAs and AlGaAs [4, 5].

2.2 Experimental setup

The generation efficiency of second harmonic light in transmission through special nonlinear crystals like BBO or KTP can be quite high [6]. However optical second harmonic generation in reflection from surfaces and interfaces is usually a very inefficient process [7], which is illustrated by the following numbers. The second harmonic intensity $I_{2\omega}$ is given by:

$$I_{2\omega} = \eta_0 \left|\chi^{(2)}\right|^2 I_\omega^2 \tag{2.1}$$

where I_ω is the intensity of the exciting laser beam at the fundamental frequency, and $\chi^{(2)}$ is the nonlinear susceptibility. The parameter η_0 contains the dielectric constants at both wavelengths and Fresnel factors. The product of η_0 and $|\chi^{(2)}|^2$ is of the order $10^{-18}\text{cm}^2/\text{W}$ [8]. For a fundamental laser power of 10 mW focused on a spot of 100 μm diameter, equation 2.1 gives a second harmonic power of 10^{-15}mW ($<$ 10 photons per second). In order to get nevertheless detectable SHG signals, high laser intensities are needed. Pulsed lasers, 100 fs pulses at a repetition rate of 82 MHz for example, have the advantage that the peak powers are high enough to generate a reasonable amount($>$ 10,000 photons per second) of light at the second harmonic frequency while the average laser power which causes heating of the sample, can be kept low enough. To detect the amount of generated light at the second harmonic frequency, which is still very small, one needs very sensitive detection setups like photomultiplier tubes combined with lock-in amplifiers or even single photon counters.

2.2.1 Titanium sapphire laser

In the experiments a mode-locked titanium sapphire laser, the Tsunami from Spectra Physics, has been used. This solid state laser has to be pumped by an other laser. In our experiments either an argon ion laser (Spectra Physics, 2040E with beamlock) has been used or an all-solid-state, diode pumped, frequency doubled, Nd:YVO_4 laser (Spectra Physics, Millennia)[1]. In figure 2.2 the laser setup with both pump lasers

---

[1] When the Ti:sapphire is pumped with the argon ion laser an average pumping power of 10 W is used and the average output power of the Ti:sapphire is then around 1 W. Since the maximum output power of the solid-state laser is only 5 W the average output power of the Ti:sapphire is then around 400 mW.

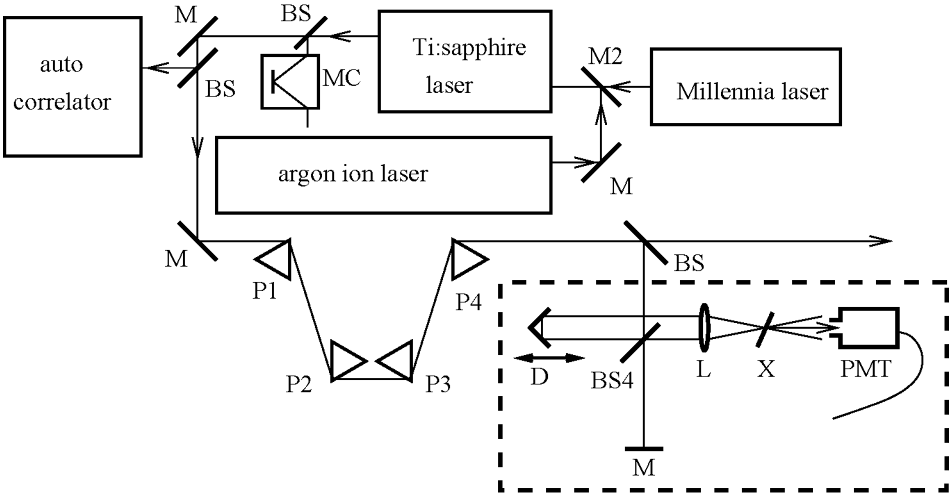

Figure 2.2: Schematic representation of the titanium sapphire laser set up. A removable beam splitter BS directs a part of the beam to a small monochromator MC to determine the wavelength of the laser light. M - mirror, BS - beam splitter, P - prism, D - delay line controlled by a step motor, L - lens, X - nonlinear crystal, PMT - photomultiplier tube. The Ti:sapphire laser can be pumped by the argon ion laser or by the solid-state laser (Millennia). When the Ti:sapphire is pumped by the solid-state laser, the mirror M2 is removed. The part of the set up in the dashed box is used to measure the temporal width of the laser pulses.

is shown. A beam with a Gaussian beam profile is generated by the Ti:sapphire laser with a repetition frequency of 82 MHz. These pulses have a Gaussian temporal profile of about 100 fs. Different mirror sets are available to vary the wavelength. With the 'short wavelength' mirror set the wavelength is continuously variable from 720 nm to 860 nm. With the 'long wavelength' mirror set in the Ti:sapphire laser it can be varied from 840 nm to 1000 nm. To monitor the stability of the pulses generated by the laser we use a homebuilt autocorrelator. This autocorrelator has been described in detail by Hollering in section 2.4 of his thesis [9].

For the time resolved experiments very short, ≈ 50 fs, pulses are needed, in order to get enough time resolution. The temporal width can be measured with the setup which is shown in the dashed box in the bottom right part of figure 2.2. The laser beam is split in two parts by the beam splitter BS4. The optical path length of one beam and thus the time delay between the pulses can be adjusted by the step motor driven delay line D. The lens L focuses both beams in a nonlinear crystal X. When the pulses overlap spatially and temporally in this crystal a Sum Frequency signal (SFG) is generated, which is detected by the photomultiplier tube PMT. The direction of the SFG signal is in between the two laser beams at the fundamental frequency, while the intensity is proportional to the spatial and temporal overlap in the crystal of the pulses from the two beams. The temporal overlap is adjusted by the delay line. Figure 2.3(a) shows a typical result of an SFG measurement.

A consequence of ultrashort pulses is a broadening of the energy width, which means that the wavelength is not sharply defined. The Fourier transform of a Gaussian wave packet with a finite width τ is a Gaussian with a finite frequency width [10], which corresponds to a finite wavelength width $\delta\lambda$ around the central wavelength λ_0 given by:

$$\delta\lambda = \frac{\lambda_0^2}{\pi \cdot c \cdot \tau} \tag{2.2}$$

where c is the speed of light. A laser pulse with a width of 40 fs in the time domain thus has a spectral width of at least 9.3 nm when the central wavelength is 840 nm.

If such a pulse with a finite spectral width[2] travels through a dispersive medium (i.e. the index of refraction n and the group velocity $\mathrm{d}n/\mathrm{d}\lambda$ are both a function of wavelength λ) like glass lenses or polarizers, different frequencies (wavelengths) will have different group velocities in the medium. For positive group velocity dispersion low frequencies travel faster than high frequencies. There fore, in a dispersive medium a pulse with pulse-width τ and thus a certain energy band-width, will broaden in time because of the differences in traveling time for the different wavelengths. To compensate for this positive dispersion and to compress the pulse we use a four prism[3] sequence as shown in figure 2.2. The prism sequence is a symmetrical arrangement specifically designed to introduce only negative group velocity dispersion, without any

---

[2] To make the pulses as short as possible the wavelength selection slit inside the laser can be opened further, thus making the spectral width larger.

[3] For the prisms SF10 glass is used.

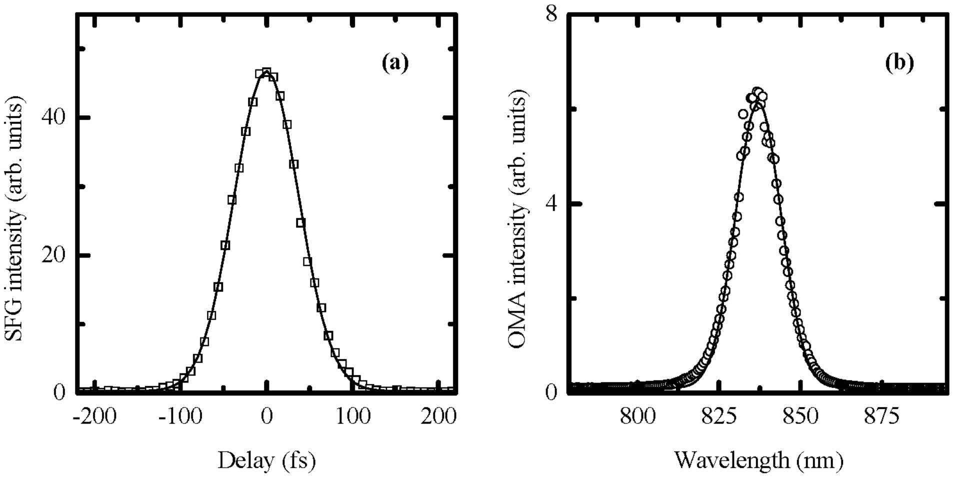

Figure 2.3: (a) Sum frequency signal measured with the setup in the dashed box in figure 2.2. The temporal width τ is 38 fs. (b) Spectrum of the laser pulse, measured with an optical multi channel analyser. The central wavelength λ_0 is 837 nm and the width $\delta\lambda$ is 9.82 nm.

net beam deviation [11][4]. This setup has the advantage that the losses are low and the group-velocity dispersion can be tuned. The distance between prisms P1 and P2 is about 30 cm. The prisms P1 and P4 are mounted on translation stages to tune the group-velocity dispersion and to be able to take them completely out of the original beam path. With this prism setup the width of the pulses could be kept $\approx$ 50 fs at the sample.

To check if the pulses are bandwidth limited, the spectral width and the temporal width have been measured before and behind the prism setup. The spectral width is measured with an optical multi channel analyser (Chromex monochromator with a Princeton Instruments CCD-camera). Figure 2.3(b) shows the result. Fitting with a Gaussian gives a central wavelength λ_0 of 837 nm and a width $\delta\lambda$ of 9.82 nm. With equation 2.2 the minimum possible temporal pulse width τ has been calculated to be 37.9 fs. Figure 2.3(a) shows the measured SFG signal. Fitting of these data gives a measured width of 38 fs, which means that within the experimental error the pulses are bandwidth limited after compression. Before compression the pulses are at least 25% longer.

---

[4] See the article of Fork *et al* [11] for more details on this part of the setup.

2.2.2 Signal detection

To detect the generated SHG light which has, as said before, a very low intensity, a photomultiplier tube (PMT) is needed. The photomultiplier tubes which have been used are most sensitive for light at the SHG-frequency (quantum efficiency of 25% at 400 nm) and relatively insensitive for light at the fundamental frequency (1% at 800 nm). The intensity of the reflected fundamental wavelength from the sample however is high enough to drive the photomultiplier tube irreversibly into saturation. Therefore BG39 color filters have been used which block the fundamental light very efficiently. However the transmission of light at the second harmonic frequency of a set of these filters is less than 50%. These filters thus reduce the SHG intensity at the entrance of the PMT further, and reduction of the noise level is thus very important. Great care has been taken to shield the experiments from daylight and other light sources in the visible region which are a main source of noise. To keep the detected background light as low as possible, the sample together with most of the optical components is placed in a box which only has a hole for the incoming beam (see figures 2.4 and 2.5).

2.2.3 Anisotropy measurements

As will be explained in chapter 3, anisotropy measurements give the possibility to separate different contributions to the SHG signal, which is necessary to determine the dependence on a static electric field. In these measurements the sample is mounted on a rotation stage and the SHG intensity is measured as a function of the rotation of the sample around an axis normal to its surface (see figure 2.4 for the setup). To manipulate the electric field in the sample, it is connected to an adjustable voltage source that can apply a bias on the sample. The power of the incoming laser beam has been reduced to the desired value of a few mW with neutral density filters. With the Soleil Babinet compensateur, used as an adjustable half wave plate, the polarization state of the incoming fundamental beam could be rotated from S to P[5]. The lens L1 focuses the laser beam on the sample to a spot diameter of about 100 μm. Color filter CF1, an OG570 filter, is opaque for wavelengths below 570 nm, and blocks all SHG light which could be generated in the optical components before the sample.

Great care has been taken to adjust the sample with its surface exactly perpendicular to the rotation axis of the rotation stage. In this way the reflected beam from the sample stays aligned while the sample is rotated during the measurement. When the sample, or the polarizer is not correctly aligned, it is very difficult to separate the different contributions to the SHG signal. The polarization of the measured second harmonic light is selected with the analyser. Lens L2 focuses the SHG light in the PMT.

---

[5] S polarization is with the polarization vector of the light perpendicular to the plane of the laser beams. P polarization is with the polarization vector parallel to this plane.

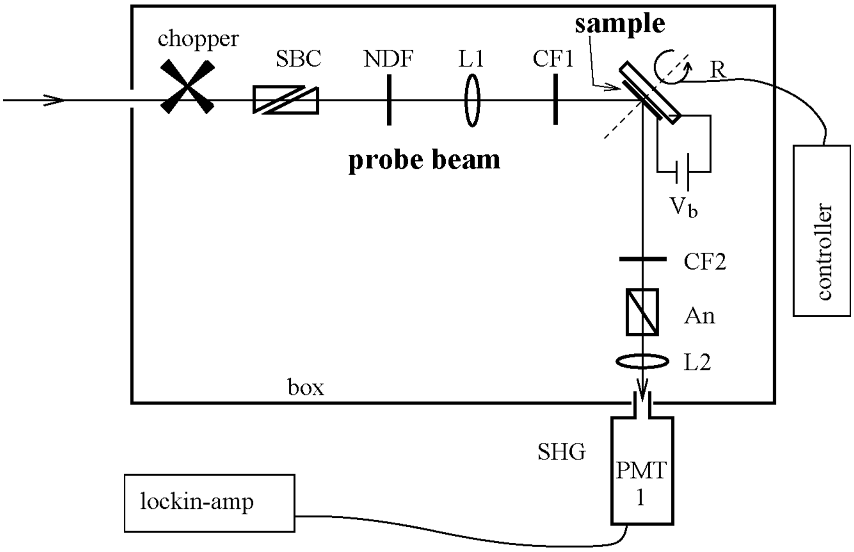

Figure 2.4: Optical setup for the anisotropy measurements. NDF - neutral density filter, SBC - Soleil Babinet compensateur, L - lens, CF - color filter, R - rotation stage, An - analyser, PMT - photomultiplier tube. The sample is mounted on the rotation stage and is connected to a voltage source which is denoted by V_b.

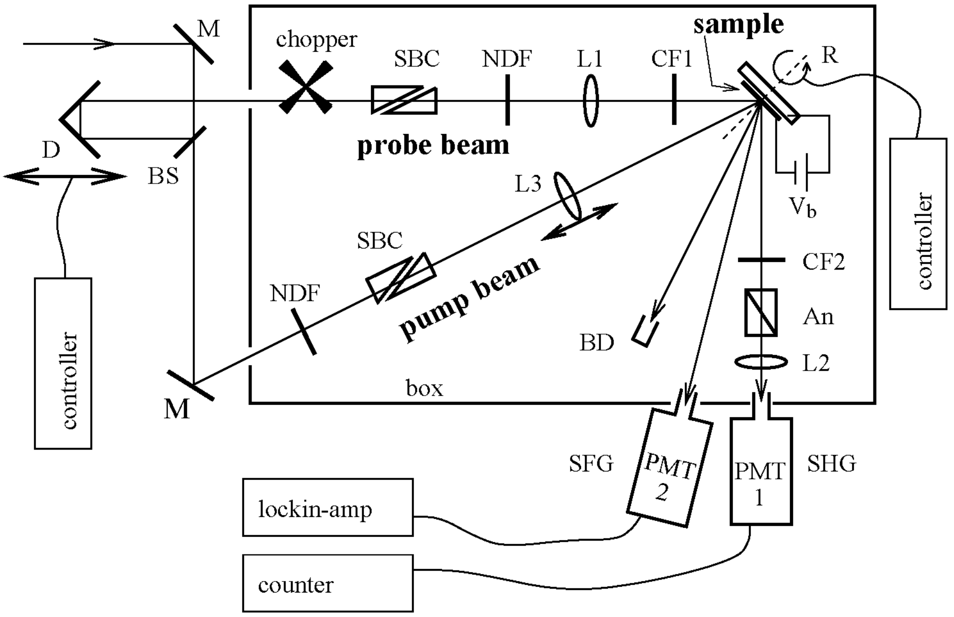

Figure 2.5: Setup for the time resolved pump-probe measurements. M - mirror, BS - beam splitter (BK7 window), D - delay line, NDF - neutral density filter, SBC - Soleil Babinet compensateur, L - lens, CF - color filter, R - rotation stage with sample, An - analyser, PMT - photomultiplier tube, BD - beam dump.

The signal of the PMT (Thorn EMI 9789B) is processed with a lock-in amplifier (SR 530)[6]. The computer which controls the rotation stage via a step motor driver reads the signal from the lock-in amplifier. Typical results of an anisotropy measurement are presented in figure 4.1 on page 36.

2.2.4 Time resolved measurements

For the time resolved experiments two beams, a pump and a probe, are needed with a controlled time delay between them. To get a pump beam, the setup of figure 2.4 has been extended as is shown in figure 2.5. The beam splitter BS splits the incoming laser beam in a transmitted pump beam which excites the carriers in the sample and a reflected probe beam to investigate the dynamics of these carriers by generating second harmonic light. To measure the time evolution of the probe

---

[6] The PMT is connected to a load resistance of 1 MΩ and the laser beam is chopped at a frequency of about 180 Hz.

SHG signal the probe pulses are delayed by a computer controlled delay line with a step size of 0.1 μm (which corresponds to a time step of 0.67 fs). The components in the probe beam are the same as in the anisotropy measurement setup of figure 2.4 except the PMT which measures the SHG signal. In the time resolved pump probe experiments an, up to ten times, lower laser power is used for the probe beam. Due to the quadratic dependence of the SHG signal on the probe laser power the SHG intensity becomes much lower and a cooled PMT (Thorn EMI 9893Q/350) in combination with a photon counter (SR 400) is needed. With the two Soleil Babinet compensateurs the polarization state of both the probe and the pump beam can be chosen independently. Also the intensity of both beams is independently adjusted with neutral density filters.

For the experiments which will be presented in chapter 5 a variable spot size of the pump beam is needed. Lens L3, which focuses the pump beam on the sample, is mounted on a micrometer translation stage to be able to vary this spot size. To determine the spot size at the sample surface, the SHG signal which is generated by the pump is measured. The beam dump BD in figure 2.5 is replaced by a BG39 filter and a PMT. The signal of this PMT is measured versus the position of the lens L3 and figure 2.6 shows typical results of such a measurement. Since the amount of SHG light is inversely proportional to the area of the laser spot [7], the maximum signal corresponds to the smallest spot size. The beam diameter in the focal point of the lens, which is the smallest possible spot size, is measured by replacing the sample with a razor blade mounted on a micrometer translation stage, and a laser power meter (Spectra Physics 407) behind it. With this translation stage the razor blade is moved perpendicular to the beam, and the laser power behind the blade is measured versus its position.

In our pump probe experiments it is necessary that pump and probe beams overlap, in space, at the sample surface. This overlap can be checked by measuring the sum frequency signal (SFG), which is generated at the sample surface when probe and pump pulses overlap in space and in time. Figure 2.5 shows that the direction of the SFG beam lies in between the reflected pump and the reflected probe beam. However this direction is not simply the bisector of the two reflected beams. The direction of the SFG beam can be calculated with the following equations which describe the component of the wavevector k parallel to the sample surface:

$$k_{||}(SFG) = k_{||}(probe) + k_{||}(pump) \tag{2.3}$$

and the total k:

$$k(SFG) = k(probe) + k(pump) \tag{2.4}$$

This SFG signal has been measured with PMT2 and a lock-in amplifier. The signal from the lock-in is used to optimize the spatial overlap of the beams. By measuring the SFG signal versus the position of the delay line, the zero-delay-point, and the width of the pulses can be determined very accurately. The results are similar to the curve presented in figure 2.3(a).

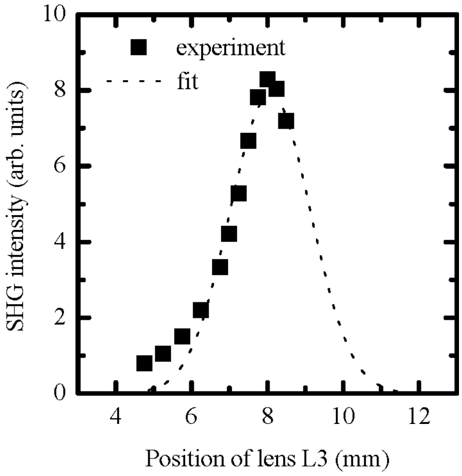

Figure 2.6: SHG-intensity versus the position of the focusing pump lens L3 in figure 2.5. The dotted line is a fit with a Gaussian.

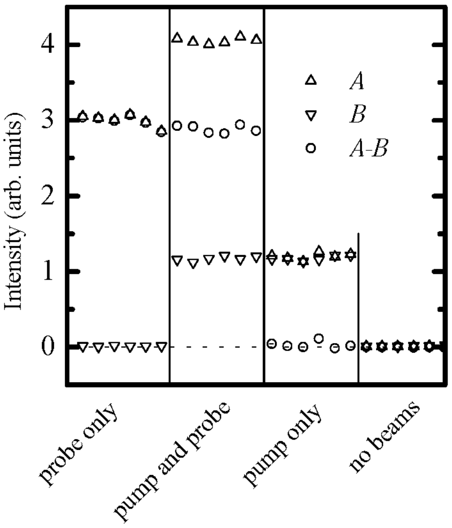

Figure 2.7: Results from the chopped counting technique with the chopper in the probe beam. Channel A is counting when the chopper is open, so it counts SHG-signal plus background. Channel B is counting when the chopper is closed, so it only counts the background signal. The length of both counting intervals is the same. The difference $A - B$ gives the background free SHG-signal. In this experiment the bias was -3 V. The first column shows that the background B is zero when the pump beam is blocked.

When the pump-beam power is increased to about 100 mW a background signal is detected by the PMT1 and the photon counting system, see figure 2.7 and figure 6.1 on page 64. This background is subtracted using a chopper in the probe beam and the two independent counters A and B of the photon counter. Channel A is counting when the chopper is open, so it counts SHG-signal plus background. Channel B is counting when the chopper is closed, so it only counts the background signal. The length of both counting intervals is the same. The difference between A and B gives the 'clean' SHG-signal. In the pump probe experiments with a low excitation intensity (chapter 5) this background is negligible. In the experiments with a high pump beam intensity which will be presented in chapter 6 this background is high and the above described method has been used to subtract it from the signal.

References

[1] P. C. M. Christianen, P. J. van Hall, H. J. A. Bluyssen, and J. H. Wolter. Ultrafast carrier dynamics at a metal-semiconductor interface studied by femtosecond luminescence spectroscopy. *Semicond. Sci. Technol.*, **9**, 707–709, (1994).

[2] P. C. M. Christianen *et al.* Ultrafast carrier dynamics at a metal-semiconductor interface. *J. Appl. Phys.*, **80**, 6831–6838, (1996).

[3] P. C. M. Christianen. *Ultrafast dynamics of hot carriers in GaAs (hetero)structures.* Ph.D. dissertation, Katholieke Universiteit Nijmegen, Nijmegen, 1993.

[4] S. M. Sze. *Physics of Semiconductor Devices.* John Wiley and Sons, New York, 2nd edition, 1981.

[5] E. H. Rhoderick and R. H. Williams. *Metal-Semiconductor Contacts.* Monographs in electrical and electronic engineering No. 19. Clarendon press, Oxford, 2nd edition, 1988.

[6] M. H. van der Mooren, Th. Rasing, and H. J. A. Bluyssen. Determination of type I phase matching angles and conversion efficiency in KTP. *Appl. Optics.*, **34**, 934–937, (1995).

[7] Y. R. Shen. *The principles of nonlinear optics.* John Wiley and Sons, New York, 1984.

[8] A. M. Malvezzi, J. M. Liu, and N. Bloembergen. Second harmonic generation in reflection from crystalline GaAs under intense picosecond laser irradiation. *Appl. Phys. Lett.*, **45**, 1019–1021, (1984).

[9] R. W. J. Hollering. *Picosecond photoluminescence studies on hot carrier energy relaxation.* Ph.D. dissertation, Katholieke Universiteit Nijmegen, Nijmegen, 1986.

[10] E. Hecht. *Optics.* Addison-Wesley Publishing Company, Reading, Massachusetts, 2nd edition, 1987.

[11] R. L. Fork, O. E. Martinez, and J. P. Gordon. Negative dispersion using pairs of prisms. *Optics Lett.*, **9**, 150–152, (1984).

Chapter 3

Theory

In this chapter a theoretical background is given concerning the time resolved SHG experiments which will be presented in this thesis. In the first section the metal semiconductor interface is described. The second section gives very briefly essential information about charge carriers in GaAs. In the next section the Monte Carlo simulations which have been performed for a better understanding of the experiments are described. The last section describes more extensively the second harmonic generation and especially the detectability of a static electric field with this technique.

3.1 Metal semiconductor interface

The issue of metal semiconductor contacts has been treated thoroughly at many places, among others in a textbook written by Rhoderick and Williams [1]. When a metal is making contact with a semiconductor, the Fermi levels in the two materials have to line up. In the case of an n-type semiconductor the Fermi level in the semiconductor is lowered relative to the Fermi level in the metal [1, 2]. This lowering is shown in figure 3.1. When the distance between metal and semiconductor decreases, an increasing negative charge is built up at the metal surface. An equal positive charge must exist in the semiconductor. This positive charge is distributed over a barrier region near the interface, and is delivered by the positive donor atoms. The width L_d of this depletion region depends on the doping density of the semiconductor. After making contact, a barrier is formed, the so called Schottky barrier. The height $e\phi_B$[1] of this barrier depends not only on the work function ϕ_m of the metal and the electron affinity χ of the semiconductor, which is an old model, but also on the orientation of the semiconductor surface, since for different orientations, the density of atoms at the interface is different [3]. Interfacial oxide layers will also influence the barrier height [1]. Finally different metals on GaAs always give a barrier height of about 0.9 eV [1, 2]. However the exact barrier height is not crucial in this thesis. The electric field in the

---

[1] The magnitude of the electron charge is denoted by e.

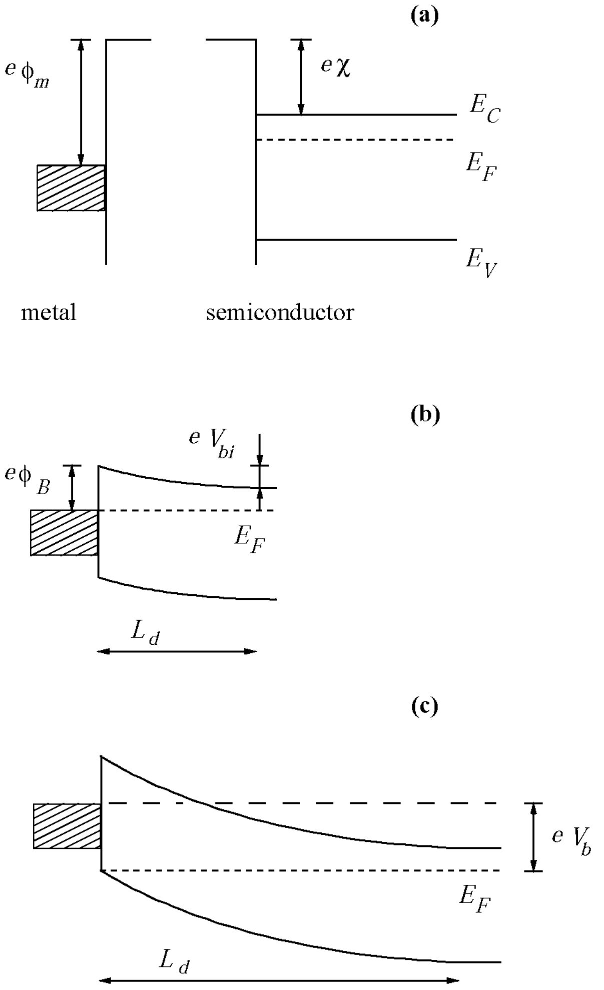

Figure 3.1: Energy band diagrams of the metal and the n-type semiconductor, (a) before making contact and (b) after making contact. In these figures ϕ_m is the metal work function, χ is the electron affinity, E_C is the conduction band energy, E_F is the Fermi energy, E_V is the valence band energy, e is the electron charge, V_{bi} is the built in potential, $e\phi_B$ is the barrier height and L_d is the depletion width. (c) Band bending and depletion width L_d with an applied bias V_b.

depletion region is important since this field is the driving force for the charge carrier dynamics.

In the depletion region approximation [1] the depletion width L_d is given by:

$$L_d = \sqrt{\frac{2\varepsilon_0\varepsilon_r}{eN_D}(V_{bi} - V_b - \frac{k_B T}{e})} \tag{3.1}$$

where $\varepsilon_0\varepsilon_r$ is the dielectric constant of the semiconductor, N_D is the doping concentration, $V_{bi} = e\phi_B - (E_C - E_F)$ is the built in potential (see figure 3.1(b)), V_b is the externally applied bias (see figure 3.1(c)), k_B is the Boltzmann constant and T is the temperature. The term $k_B T/e$ arises from the contribution of the mobile carriers to the electric field. This depletion region approximation assumes that the space charge $\rho = eN_D$ for $0 < z < L_d$ and $\rho = 0$ elsewhere, where $\hat{z}$ is the direction perpendicular to the interface. At the interface $z = 0$ and inside the semiconductor $z > 0$. The electric field in the depletion region ($0 < z < L_d$) is then given by [2]:

$$|E(z)| = \frac{eN_D}{\varepsilon_0\varepsilon_r}(L_d - z) = \sqrt{\frac{2eN_D}{\varepsilon_0\varepsilon_r}(V_{bi} - V_b - \frac{k_B T}{e})} - \frac{eN_D}{\varepsilon_0\varepsilon_r}z \tag{3.2}$$

From equations 3.1 and 3.2 it is clear that an externally applied bias V will influence both the depletion width L_d and the electric field $E(z)$ as is shown in the figures 3.1(b) and 3.1(c).

3.2 Charge carriers in GaAs

Since GaAs has a direct band gap it is a very useful material for opto-electronic devices. The electronic and optical properties of a material are determined by its band structure. We therefore examine the band structure of GaAs[2] as given in figure 3.2. The direct bandgap at the center of the Brillouin zone is formed by the Γ_6 and Γ_8 extrema of the conduction and valence band. The width of the bandgap E_g^Γ strongly depends on lattice temperature and varies from 1.52 eV at 0 K to 1.42 eV at 300 K [5, 7, 8]. The minima of the side valleys in the $< 111 >$ and $< 100 >$ direction, L_6 and X_6, are lying a few tenth of an eV above the minimum in the Γ valley, 0.28 eV for the L valley and 0.48 eV for the X valley respectively [9]. In the L valley the effective mass of the electrons is 1.6 times higher than in the Γ valley. In the X valley it is even 4.8 times higher. The band structure of $\mathrm{Al}_x\mathrm{Ga}_{1-x}\mathrm{As}$ is similar, only the bandgap at the Γ point is increasing with increasing x [10]:

$$E_g^\Gamma = 1.424 + 1.45x - 0.25x^2 \qquad \text{for } x \leq 0.45 \tag{3.3}$$

More important is that for $x \geq 0.45$ the bandgap is no longer direct since then the Γ valley lies higher than the X valley.

When the semiconductor is exposed to light with a photon energy higher than the bandgap, electrons will be excited from the valence band to the conduction

---

[2] See reference [4] for a review of the properties of GaAs.

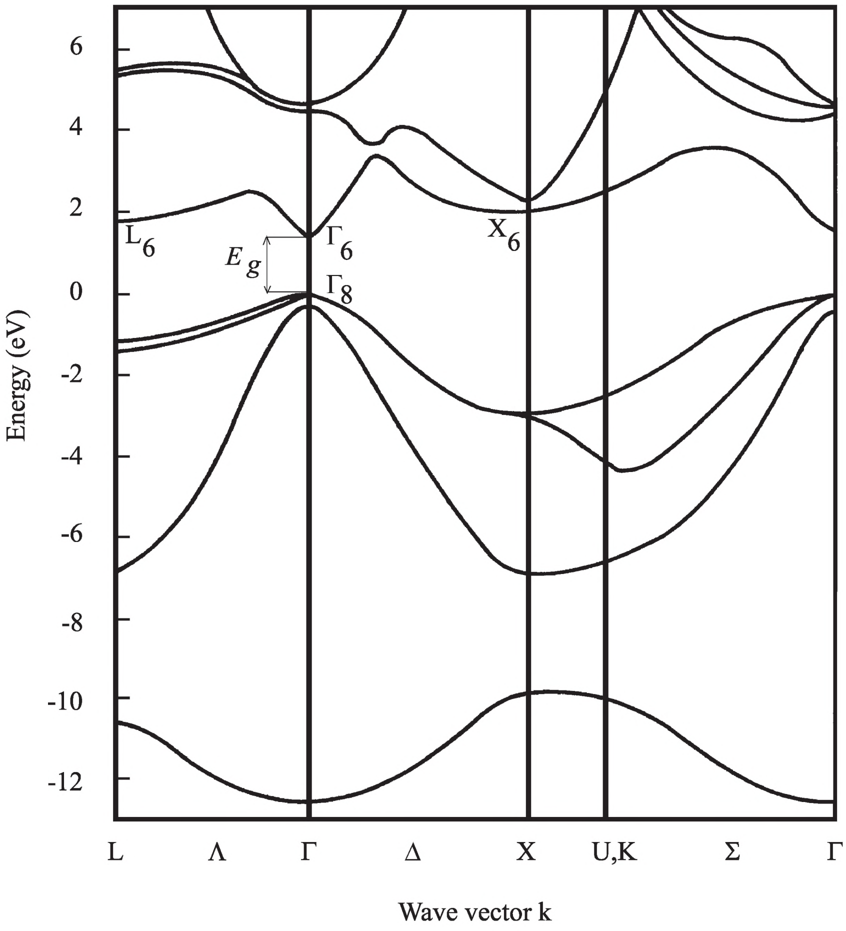

Figure 3.2: Part of the band structure of GaAs [5, 6]. The width of the direct bandgap at the Γ-point is denoted by E_g.

band, leaving holes in the valence band. The difference between the photon energy and the bandgap energy is the excess energy of the excited carriers. If this excess energy is larger than the separation between the central Γ valley and the satellite L and X valleys, the electrons can scatter immediately to these side valleys. In the presence of an electric field, as is the case at a Schottky barrier interface, the excited charge carriers will be accelerated by the field, leading to a spatial separation of electrons and holes. This charge separation again influences the driving electric field in the semiconductor. As a result the electric field will become time and position dependent. Moreover, in the case of a strong field the electrons may gain enough energy to reach the L and X side valleys.

Several scattering mechanisms (for example carrier-carrier, carrier-optical phonon or carrier-acoustic phonon) exist via which the carriers relax to the minimum of the conduction band, and subsequently recombine with the hole in the valence band. All these have characteristic time scales.

Different techniques are available to measure these processes which all probe different properties, like time resolved photo luminescence (PL), reflective electro optic sampling (REOS) or THz emission [11–13]. To measure the electric field dynamics at a metal semiconductor interface, optical second harmonic generation (SHG) is more suitable since it is able to probe properties at buried interfaces [14–17]. On the other hand, if the main effect occurs in the bulk (more than 20 nm from the surface) SHG may not be the most suitable method.

3.3 Monte Carlo simulations

Monte Carlo simulations have been performed by Van Hall from the Eindhoven University of Technology to calculate the time evolution of the electric field in the Schottky Barrier sample after excitation of charge carriers. This technique gives the possibility to calculate the average positions and velocities of a set of charge carriers in such complex situations as described above. This method has been well established and various reviews have been published [18–22]. In a Monte Carlo calculation one follows a large number of representative particles. These particles are subjected to the force of the electro-magnetic fields and to the various scattering mechanisms. Ensemble averages then give such quantities as average velocity, energy position etc., if necessary time dependent.

In these simulations the device is modeled schematically with a parabolic band bending. The 0.3 μm-thick GaAs depletion layer is separated from the thin Au film by the Schottky barrier. At the backside, the depletion layer is bounded by the superlattice (see figure 2.1). Due to its heavy n-type doping the superlattice is assumed to form no barrier for the electrons and a large one for the holes. When no bias, or a reverse bias, is applied, as is the case in most of the experiments, the superlattice has no influence on the transport of holes since the holes move towards the interface and the electrons towards the sample substrate. When a reverse bias is applied a negative interface charge is created at the Au film which is compensated for by a constant intrinsic space-charge throughout the whole depletion layer, giving rise to a linear decreasing electric field and a parabolic potential like in figure 3.1(c). In the model which is used in the simulations the depletion width is constant and equal to the GaAs layer thickness[3], whereas the doping concentration is varied with the applied bias voltage. However in an actual Schottky device the doping level is constant and the depletion width changes with bias voltage [2] as given by equation 3.1 and shown in figures 3.1(b) and 3.1(c). When a reverse bias of 3.0 V is applied to the Schottky barrier sample the depletion region approaches the GaAs layer thickness. We therefore believe that although this model is rather schematic it nevertheless contains the basic physics needed for describing semi-quantitatively the experimental results for the high (3 V) reverse bias voltages.

In the calculations the carriers are created in the depletion layer according to the absorption length in GaAs for the incident laser light, which is about 1 μm. The temporal width of the laser pulse (< 200 fs) which excites the carriers is also taken into account. The subsequent transport and energy relaxation of both electrons and holes in the GaAs layer are computed in a Monte-Carlo simulation [18], accounting for the various scattering mechanisms such as optical and acoustic phonon-, ionized impurity-, intervalley-, and carrier-carrier scattering [19, 21]. Both electron-heavy- and -light-hole pairs are considered, including hole inter-band transitions [22] and the Pauli exclusion principle. In most cases 10^5 electron-hole pairs were used for the simulations. The material parameters have been taken from the review paper by Adachi [9].

The diameter of the laser spot, 100 μm, is much larger than the thickness of the depletion layer, 300 nm. The carrier dynamics in the semiconductor can thus be treated in one dimension perpendicular to the interface. To calculate the net electric field after excitation of the charge carriers the Poisson equation is solved in one dimension every time step of the calculation, resulting in a time-dependent space charge field in addition to the applied field. Since the space charge field varies strongly in time and position, it turned out to be necessary to make the time steps as small as 1 fs.

To compare the measured SHG intensity with the results of the Monte Carlo simulations the finite escape depth of the SHG light should be taken into account. First the electric field is calculated as a function of the position z in the depletion layer. Then the field is multiplied by a factor $\exp(-z\alpha)$ (where α is the absorption coefficient of the SHG light in GaAs), and summed over the whole depletion layer. This procedure is identical to the integration of equation A.19 in appendix A.

In these, quite standard, simulations two new features have been incorporated: first a decoupling of the electron-hole plasma from the outside world after excitation and second a plasmon-phonon coupling. The excited charge density in the illuminated part can be much higher than the charge density, due to the applied bias, on the gold layer. For example the photo-excited charge density can exceed the intrinsic one by a factor of 20, inevitably leading to serious consequences for the carrier sweep-out [11], as will be shown in the following. In a reverse biased Schottky Barrier sample the very thin gold layer is negatively charged. After excitation of charge carriers

---

[3] For our samples this thickness is 300 nm.

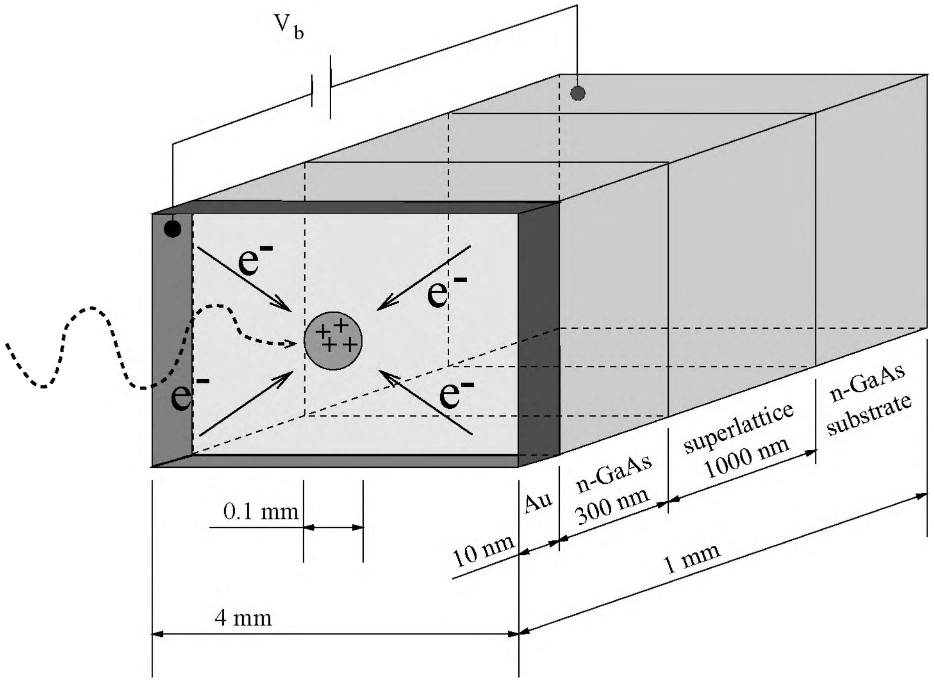

Figure 3.3: Drawing of the device (not to scale), with the sizes of the different layers and the laser spot. It also shows the charge flow in the gold layer.

by the laser pulse the holes are driven by the electric field to the gold layer and will compensate the negative charge. A circular area with the diameter of the laser beam will become positive (this area is indicated in figure 3.3). To recharge this positive area electrons have to flow through the very thin (100 Å) Au-layer, which will take some time. Obviously this re-charging time depends on the diameter of the area and the resistance of the metal layer. This time can be estimated by the RC-time constant of a disc with the same diameter as the laser spot and the thickness of the metal-layer[4]. During this re-charging time the field inside the semiconductor is collapsed, and possibly inverted. When the field is inverted the charge carriers can start oscillating. In order to investigate the consequences of such a re-charging time for the carrier sweep-out, we introduced a so-called regeneration time constant τ_{reg}. The latter indicates how long it takes to transfer charge to the illuminated part of the top contact in order to keep the total voltage across the depletion layer constant. However, it should be noted that also in the case holes are pinned in the band bending region, eg. due to an oxide layer at the Au-GaAs interface or the cap layer in case of the samples '1' and '3' of figure 2.1, an extra amount of charge has to be transferred to the top contact in order to keep the voltage at its original value. From the recovery of the SHG signal in the experiments at low excitation densities which will be described in chapter 5 we deduced a value of about 25 ps for this regeneration time, which has been used for all the calculations. The effect of this regeneration time is a temporary decoupling of the photo excited electron-hole plasma from the outside world.

With this decoupling included in the Monte Carlo simulations oscillations appear in the electric field when the density of excited carriers in the simulation is increased. These oscillations are visible in the lowest curve of figure 3.4. In this figure the electric field dynamics is plotted for different values of the excitation intensity[5]. These oscillations have frequencies in the THz regime. The bulk LO and TO phonon frequencies in GaAs are in the same regime and thus the coupling between the plasma and phonon oscillations has to be taken into account.

To obtain the plasmon-phonon coupling we partially followed the procedure of Scholz and Stahl [23]. There are two contributions to the dielectric constant [24]: $\varepsilon_r(\omega = \infty)$, due to polarization of the electron clouds and $\varepsilon_r(\omega = 0) - \varepsilon_r(\omega = \infty)$, resulting from the polarization of the ion positions i.e. the lattice. The latter has the LO phonons as eigen modes. In the presence of an electric field the lattice is polarized with a polarization P_L. After excitation of charge carriers the electric field changes abruptly due to the charge separation, as shown above, and can start oscillating at the plasma frequency. The lattice polarization P_L cannot follow instantly. We then have to separate the equation of motion of the lattice from the Poissons equation and solve [23]:

$$\frac{d^2}{dt^2}P_L + \gamma\frac{dP_L}{dt} + \omega_{LO}^2 P_L = \omega_{TO}^2 \varepsilon_0 (\varepsilon_r(0) - \varepsilon_r(\infty)) E_0 \tag{3.4}$$

---

[4] C-V measurements indicated a capacitance per area of 5.2 × 10^{-4} Fm^{-2}, with a diameter of 100 μm and a square resistance of a few Ohms for the gold layer the RC-time is about 30 ps [11].

[5] In chapter 6 these results are presented and discussed in more detail.

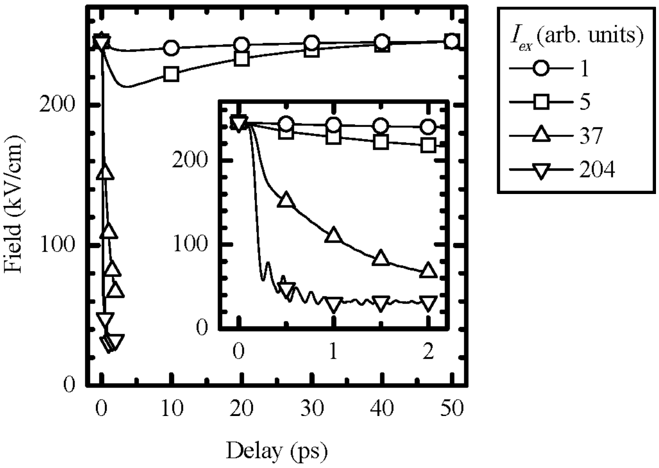

Figure 3.4: Typical results from the Monte Carlo simulations for different values of the excitation intensity. Intensity '1' corresponds to a density of excited carriers of 10^{16} cm^{-3}. In the inset the dynamics of the electric field in the first 2 ps has been plotted in more detail. In these curves the finite escape depth of the SHG is already taken into account. As a consequence the field is not inverted in this figure. See chapter 6 for more details.

Here E_0 is the field due to the space charge, calculated via Poissons equation, which starts oscillating at the plasma frequency and the ω_{LO} and ω_{TO} are the frequencies of the optical phonons, where

$$\omega_{TO} = \omega_{LO} \frac{\varepsilon_r(0)}{\varepsilon_r(\infty)} \tag{3.5}$$

The damping constant γ is the inverse lifetime of the LO phonon. Its value is about $(4 \text{ ps})^{-1}$. On the time scale we are interested in (< 2 ps), its effect is of minor importance. Due to our microscopic description of the plasmon, the mutual coupling between the lattice and plasma oscillations is asymmetric. The oscillations of the P_L are driven by the space charge field E_0. On the other hand P_L contributes to the total driving field $E = E_0 - P_L/\varepsilon_0$ and thus affects the motion of the carriers i.e. the plasmon. It should be noted here, that in the macroscopic description of the plasmon as employed by others [23, 25] with an equation analogous to equation 3.4, one has to introduce a very strong plasmon damping term - a common value is $(0.1 \text{ ps})^{-1}$. In our simulations, however, the damping is accounted for automatically by the scattering processes.

3.4 Optical second harmonic generation

In this section we follow the very extensive description of second harmonic generation and other nonlinear optical effects which has been given by Shen in *The principles of nonlinear optics* [14].

The optical response of a medium is described by the induced polarization **P**. For relatively weak applied electromagnetic fields, the relation between **P** and the macroscopic electric field **E** is given by:

$$P_i = \sum_{j=x,y,z} \chi_{ij} E_j \tag{3.6}$$

The susceptibility $\overset{\leftrightarrow}{\chi}^{(1)}$ is a second rank tensor of first order, having nine elements. For stronger fields higher order contributions become important. Within the electric dipole approximation the fields are assumed to be spatially homogeneous, and the induced polarization can be written as an expansion of the electric field:

$$\mathbf{P} = \overset{\leftrightarrow}{\chi}^{(1)} \cdot \mathbf{E} + \overset{\leftrightarrow}{\chi}^{(2)} : \mathbf{EE} + \overset{\leftrightarrow}{\chi}^{(3)} \vdots\, \mathbf{EEE} + ... \tag{3.7}$$

If only laser fields at a frequency ω play a role, the above formula can be split in its harmonics:

$$\mathbf{P} = \mathbf{P}(\omega) + \mathbf{P}(2\omega) + \mathbf{P}(3\omega) + ... \tag{3.8}$$

where the subsequent terms describe the linear response, second harmonic generation (SHG) and third harmonic generation (THG). These polarizations act as the source of radiation at the corresponding frequencies.

The number of independent and nonzero components of the susceptibility tensors $\overleftrightarrow{\chi}^{(\mathrm{n})}$ is restricted by the actual symmetry of the material under consideration. For centro-symmetric media, i.e. media which have centers of inversion symmetry like gases, liquids and metals, $\overleftrightarrow{\chi}^{(\mathrm{n})}$ is zero for all even-n. As a second order nonlinear optical effect, SHG is, under the electric-dipole approximation, forbidden in such media. [14]. It is evident however that at interfaces of these media the inversion symmetry is necessarily broken. For this reason the process is highly surface specific for interfaces between two centrosymmetric media, which is also true for buried interfaces [15, 16]. GaAs is not centrosymmetric and thus bulk contributions exist, but also in this medium interfaces give a reduction of the symmetry resulting in a larger number of independent and/or nonzero tensor elements.

GaAs belongs to the $\bar{4}3$m symmetry class and the crystal structure is shown in figure 3.5(a). In $\bar{4}3$m, six of the 27 bulk elements χ_{ijk} of $\overleftrightarrow{\chi}^{(2)}$, are nonzero. These elements are given by equation A.1 in appendix A. Figure 3.5(b) shows the (001) face of GaAs which has mm2 symmetry. In its own coordinate system[6], mm2 symmetry gives 7 independent tensor elements[7] of the interface susceptibility tensor $\overleftrightarrow{\Delta}^{(2)}$. In second harmonic generation the second and third index of all tensor elements can be interchanged since the generating fields, **EE** in the second term of equation 3.7, are identical. This reduces the number of independent elements as is shown in appendix A.

In principle higher order terms like the quadrupolar term [27]:

$$P_i(2\omega) = \Gamma_{ijkl} E_j(\omega) \nabla_k E_l(\omega) \tag{3.9}$$

can contribute to the SHG signal, however this contribution is expected to be below the detection limit of our setup and will not be taken into account.

For electric field induced second harmonic generation (EFISHG) not only optical electric fields at the frequency ω play a role, but also quasi static electric fields at zero frequency or a frequency much lower than the optical frequency. Now the induced polarization at the second harmonic frequency can be written as an expansion of the static electric field $\mathbf{E}(0)$ as [14]:

$$\mathbf{P}(2\omega) = \overleftrightarrow{\chi}^{(2)} : \mathbf{E}(\omega)\mathbf{E}(\omega) + \overleftrightarrow{\chi}^{(3)} \vdots \mathbf{E}(\omega)\mathbf{E}(\omega)\mathbf{E}(0) + \overleftrightarrow{\chi}^{(4)} \mathbin{\vdots\!\!\vdots} \mathbf{E}(\omega)\mathbf{E}(\omega)\mathbf{E}(0)\mathbf{E}(0) + .. \tag{3.10}$$

Where $\overleftrightarrow{\chi}^{(3)}$ and $\overleftrightarrow{\chi}^{(4)}$ have symmetry properties of the $\bar{4}3$m bulk crystal[8]. The mm2 interface of the crystal can also contribute to this process[9].

---

[6] $\hat{x}'$ and $\hat{y}'$ in figure 3.5(b) are the basis vectors usually associated with the mm2 group [26]. The basis vectors $\hat{x}$ and $\hat{y}$ that are also shown in this figure are identical to the basis vectors of the $\bar{4}3$m system.

[7] See equation A.2.

[8] See equations A.6 to A.8 for the relevant tensor elements.

[9] The corresponding tensor elements are given by the equations A.9 and A.10.

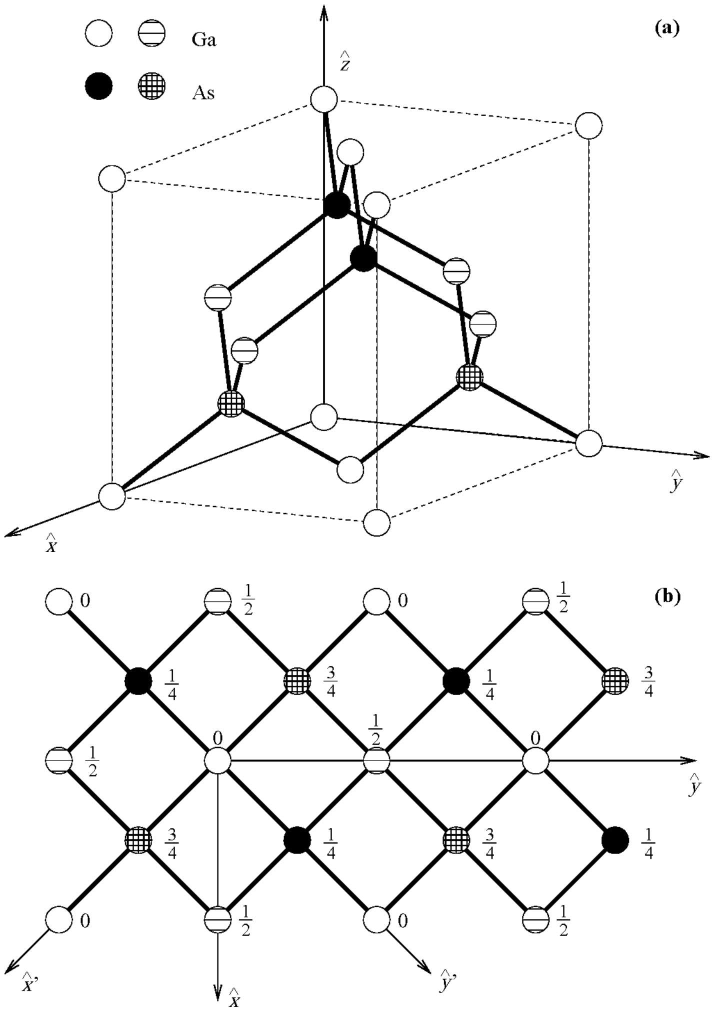

Figure 3.5: (a) Crystal structure of GaAs with the $\hat{x}$, $\hat{y}$ coordinate system natural to the $\bar{4}3$m symmetry class. (b) The (001) plane which also shows the $\hat{x}'$, $\hat{y}'$ coordinate system associated with the mm2 symmetry. The atomic positions of the Ga and the As are projected on a cube face; fractions denote the distance below the surface in units of a cube edge.

Taking equations A.1, A.4, A.7, A.8, A.9 and A.10 together, the effective susceptibility elements can be determined[10]. The equations for the effective susceptibility elements show that for the bulk elements the linear electric field dependence and the quadratic electric field dependence (respectively the second and the third term in equation 3.10) appear in different tensor elements and can thus be separately measured in an experiment. For the interface elements the linear and quadratic dependence appear in the same elements and can thus not be separated.

The total field radiated by the nonlinear polarization $\mathbf{P}(2\omega)$ will depend on the orientation of the crystal, the polarization state of the incoming radiation, the angle of incidence, and the dielectric properties of the crystal. For linearly polarized input fields incident on a GaAs(001) surface, it can be shown that the radiated second harmonic fields $E_{in,out}$[11] are given in terms of the input electric fields E_p and E_s measured outside the material[12]. The detected Second Harmonic Intensity $I_{in,out}$ is proportional to this second harmonic field $E_{in,out}$ squared. Using the expressions for $E_{in,out}$, $I_{in,out}$ can be parameterized by:

$$I_{in,out} = \left| a_{io} + \sum_{m=1}^{4} \left[b_{io}^{(m)} \sin m\psi + c_{io}^{(m)} \cos m\psi \right] \right|^2 \tag{3.11}$$

where ψ is the angle between the plane of incidence and the (100) axis of the GaAs. In so called anisotropy measurements $I_{in,out}$ is measured as a function of the angle ψ. Fitting with equation 3.11 gives the possibility to determine the a_{io}, $b_{io}^{(m)}$ and $c_{io}^{(m)}$ terms. For the $\bar{4}3$m and mm2 symmetries only even m terms contribute to the sum (see appendix A), and a_{io} is zero for s-out experiments. Table 3.1 reviews the tensor elements which contribute to the parameters a_{io}, $b_{io}^{(m)}$ and $c_{io}^{(m)}$. Γ_{ijkl} refers to the bulk quadrupolar terms of equation 3.9 [28]. Comparison of this table with equation A.11 shows that the bulk elements which depend linearly on the static electric field, only appear in the parameter a_{io}. The bulk elements which depend quadratically on the electric field appear in the terms $b_{io}^{(2)}$ and $c_{io}^{(2)}$. By choosing the right polarization combinations in the experiment the parameters a_{io}, $b_{io}^{(m)}$ and $c_{io}^{(m)}$, and thus the electric field dependence (linear or quadratic) of the bulk terms can be measured independently. For the interface terms this separation is not possible since both the linear and the quadratic dependence appears in all terms.

---

[10] Given by the equations A.11 and A.12.

[11] '*in*' is the polarization state of the incoming light and '*out*' the polarization state of the generated light at the second harmonic frequency. For both only 'P' and 'S' polarization has been measured in the experiments.

[12] Equations A.13 to A.17.

$\chi^{(eff)}$ io	P-in P-out pp	P-in S-out ps	S-in P-out sp	S-in S-out ss
$\chi^{(eff)}_{xxz}$	a_{pp}	-	-	-
$\chi^{(eff)}_{zxx}$	a_{pp}	-	a_{sp}	-
$\chi^{(eff)}_{zzz}$	a_{pp}	-	-	-
$\chi^{(eff)}_{xyz}$	$b^{(2)}_{pp}$	$c^{(2)}_{ps}$	-	-
$\chi^{(eff)}_{zxy}$	$b^{(2)}_{pp}$	-	$b^{(2)}_{sp}$	-
Γ_{ijkl}	$a_{pp}, c^{(4)}_{pp}$	$b^{(4)}_{ps}$	$a_{sp}, c^{(4)}_{sp}$	$b^{(4)}_{ss}$

Table 3.1: Contributions to the different elements of $\chi^{(eff)}$ for different polarization combinations.

References

[1] E. H. Rhoderick and R. H. Williams. *Metal-Semiconductor Contacts.* Monographs in electrical and electronic engineering No. 19. Clarendon press, Oxford, 2nd edition, 1988.

[2] S. M. Sze. *Physics of Semiconductor Devices.* John Wiley and Sons, New York, 2nd edition, 1981.

[3] J. Tersoff. New empirical approach for the structure and energy of covalent systems. *Phys. Rev. B*, **37**, 6991–7000, (1988).

[4] J. S. Blakemore, editor. *Gallium Arsenide.* Number 1 in Key papers in physics. American Institute of Physics, New York, 1987.

[5] O. Madelung, W. von der Osten, and U. Rössler. Gallium arsenide. In O. Madelung, editor, *Landolt-Börnstein, Numerical Data and Functional Relationships in Science and Technology*, volume 22, Semiconductors, Subvolume a, Intrinsic Properties of Group IV Elements and III-V, II-VI and I-VII Compounds of *New Series Group III: Crystal and Solid State Physics*, chapter 2.10. Springer-Verlag, Berlin, 1987.

[6] J. R. Chelikowsky and M. L. Cohen. Nonlocal pseudopotential calculations for the electronic structure of eleven diamond and zinc-blende semiconductors. *Phys. Rev. B*, **14**, 556–582, (1976).

[7] C. D. Thurmond. The standard thermodynamic functions for the formation of electrons and holes in Ge, Si, GaAs, and GaP. *J. Elchem. Soc.*, **122**, 1133–1141, (1975).

[8] J. S. Blakemore. Semiconducting and other major properties of gallium arsenide. *J. Appl. Phys.*, **53**, R123–R181, (1982).

[9] S. Adachi. GaAs, AlAs, and $\mathrm{Al}_x\mathrm{Ga}_{1-x}\mathrm{As}$: Material parameters for use in research and device applications. *J. Appl. Phys.*, **58**, R1–R29, (1985).

[10] R. J. Deri and M. A. Emanuel. Consistent formula for the refractive index of $\mathrm{Al}_x\mathrm{Ga}_{1-x}\mathrm{As}$ below the band edge. *J. Appl. Phys.*, **77**, 4667–4672, (1995).

[11] P. C. M. Christianen *et al.* Ultrafast carrier dynamics at a metal-semiconductor interface. *J. Appl. Phys.*, **80**, 6831–6838, (1996).

[12] R. R. Alfano, editor. *Semiconductors Probed by Ultrafast Laser Spectroscopy.* Academic Press, Orlando, 1984.

[13] P. F. Barbara, J. G. Fujimoto, W. H. Knox, and W. Zinth, editors. *Ultrafast Phenomena X*, volume 62 of *Springer Series in Chemical Physics*, Berlin, 1996. Springer-Verlag.

[14] Y. R. Shen. *The principles of nonlinear optics.* John Wiley and Sons, New York, 1984.

[15] Th. Rasing. Studies of buried interfaces by optical second-harmonic generation. *Appl. Phys. A*, **59**, 531–536, (1994).

[16] H. A. Wierenga *et al.* Interface magnetism and possible quantum well oscillations in ultrathin Co/Cu films observed by magnetization induced second harmonic generation. *Phys. Rev. Lett.*, **74**, 1462–1465, (1995).

[17] W. de Jong *et al.* Electric field dynamics at a metal-semiconductor interface probed by femtosecond optical second harmonic generation. *Surf. Sci.*, **331-333**, 1372–1376, (1995).

[18] C. Jacoboni and L. Reggiani. The Monte Carlo method for the solution of charge transport in semiconductors with applications to covalent materials. *Rev. Mod. Phys.*, **55**, 645–705, (1983).

[19] C. Jacoboni and P. Lugli. *The Monte Carlo Method for Semiconductor Device Simulation.* Computational Microelectronics. Springer-Verlag, Berlin, 1989.

[20] C. Moglestue. *Monte Carlo Simulation of Semiconductor Devices.* Chapman and Hall, London, 1st edition, 1993.

[21] L. Reggiani, editor. *Hot-Electron Transport in Semiconductors*, volume 58 of *Topics in Applied Physics.* Springer-Verlag, Berlin, 1985.

[22] M. Costato and L. Reggiani. Scattering probabilities for holes I. Deformation potential and ionized impurity scattering mechanisms. *Phys. Stat. Sol. B*, **58**, 471–482, (1973).

[23] R. Scholz and A. Stahl. Generation of LO-phonons in a time-dependent electric field at the surface of III-V materials. *Phys. Stat. Sol. B*, **168**, 123–138, (1991).

[24] O. Madelung. *Introduction to Solid-State Theory*, volume 2 of *Springer Series in Solid-State Sciences.* Springer-Verlag, Berlin, 1981.

[25] A. V. Kuznetsov and C. J. Stanton. Coherent phonon oscillations in GaAs. *Phys. Rev. B*, **51**, 7555–7565, (1995).

[26] R. R. Birss. *Symmetry and Magnetism*, volume 3 of *Selected topics in solid state physics.* North-Holland, Amsterdam, 1964.

[27] B. Koopmans. *Interface and bulk contributions in optical second-harmonic generation.* Ph.D. dissertation, Rijksuniversiteit Groningen, Groningen, 1993.

[28] J. E. Sipe, D. J. Moss, and H. M. van Driel. Phenomenological theory of optical second- and third-harmonic generation from cubic centrosymmetric crystals. *Phys. Rev. B*, **35**, 1129–1141, (1987).

Chapter 4

Anisotropy measurements

As stated already in the previous chapter, second harmonic generation is sensitive to almost everything which breaks the inversion symmetry. Since we are interested in a particular symmetry breaking event, namely a, possibly oscillating, electric field in the depletion region of the semiconductor, it should be demonstrated that we are probing this field and not another effect.

In this chapter experiments are presented where we probe a static electric field which is controlled by the bias applied to the sample, by measuring the SHG intensity versus the rotation of the sample. The results show that the electric field dependent part of the signal and the electric field independent part can be separated as proposed in section 3.4. Section 4.2 shows that the independent part behaves as normal SHG which gives the possibility to use this part for normalization. In section 4.3 the field dependent part is investigated. It is shown that under certain conditions of the sample orientation and polarization combination of the beams the change in SHG intensity is linearly proportional to the change in the electric field in the depletion region. This dependence makes SHG very suitable for measuring the dynamics of this electric field.

4.1 Experimental Results

The anisotropy experiments have been performed with the setup of figure 2.4. By doing anisotropy measurements some of the tensor elements which contribute to the SHG signal can be separated as argued in section 3.4. Figure 4.1 shows the results of anisotropy measurements from a sample with layer composition '2' (no cap layer) from section 2.1, for four different polarization combinations of the incoming fundamental and outgoing second harmonic beam and with two different values of the applied bias. The open squares present data at 0 V bias, the filled dots at a bias of -3.5 V. Since the intensity of the light at the second harmonic frequency differs between the different figures, the vertical scale is different for the figures (a) and (b) in comparison to (c) and (d). A very clear bias dependence of the SHG intensity $I_{2\omega}$ can be seen in the

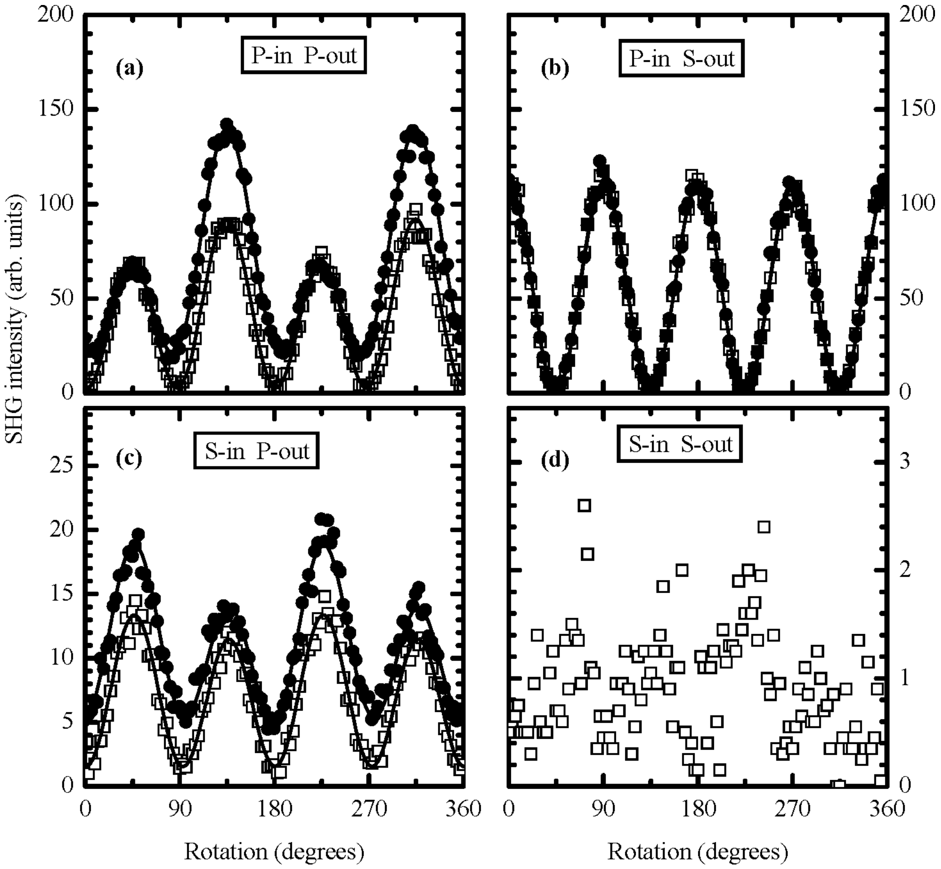

Figure 4.1: Anisotropy curves for four different combinations of the incoming and outgoing polarization, measured with a λ of 846 nm on sample 2A. The laser power is 3.5 mW for the P-in measurements in figures (a) and (b), 6 mW for the S-in P-out measurements in figure (c) and 20 mW for the S-in S-out measurement in figure (d). In the figures (a), (b), (c) and (d) the open squares are data with an applied bias of 0 V and the filled dots (absent in figure (d)) are data with a bias of -3.5 V applied to the sample. The solid lines in the figures are fits according to equation 4.1. Note that the vertical scales are different for the figures (a) to (d). At a rotation of 0° the (100) axis is in the plane of incidence.

figures (a) and (c), while there is hardly any difference in figure (b).

According to equation 3.11 the $I_{2\omega}$ can be described by:

$$I_{in,out} = \left| a_{io} + \sum_{m=1}^{4} \left[b_{io}^{(m)} \sin m\psi + c_{io}^{(m)} \cos m\psi \right] \right|^2 \tag{4.1}$$

The measured curves have been fitted to this equation with the complex amplitudes a_{io}, $b_{io}^{(2)}$, $c_{io}^{(2)}$, $b_{io}^{(4)}$ and $c_{io}^{(4)}$ as fitting parameters. We were able to fit most of the experimental data very well as is shown by the solid lines in the figures 4.1(a), 4.1(b) and 4.1(c). Due to the low signal level, the data of figure 4.1(d) could not be fitted. Table 4.1 shows the fit results for three different combinations of polarization and applied bias. According to table 3.1 the symmetry allowed amplitudes a_{pp}, $b_{pp}^{(2)}$ and $c_{pp}^{(4)}$ could be nonzero for the P-in P-out polarization combination. The fit results show that a_{pp} and $b_{pp}^{(2)}$ are indeed nonzero and measurable. However $c_{pp}^{(4)}$ is zero within the experimental error. For the P-in S-out combination $c_{ps}^{(2)}$ and $b_{ps}^{(4)}$ could be nonzero. The fit results show that here $b_{ps}^{(4)}$ is zero. The finite value of a_{ps} which appears in the fit is not symmetry allowed (table 3.1). The origin of this signal is probably a slight misalignment of the analyser in front of the photomultiplier tube (see figure 2.4). For the S-in P-out combination a_{sp} and $b_{sp}^{(2)}$ are nonzero according to table 3.1 while $c_{sp}^{(4)}$ is again zero. For the S-in S-out combination in figure (d) only the $b_{ss}^{(4)}$ term should be nonzero. The 'signal' which is visible in figure (d) has the same amplitude as the background signal in figure (b) and no good fit results could be obtained, even for a much larger laser power. The conclusion can thus be drawn that also the $b_{ss}^{(4)}$ term is close to zero.

	P-in P-out		P-in S-out		S-in P-out	
io	*pp*		*ps*		*sp*	
bias	0 V	-3.5 V	0 V	-3.5 V	0 V	-3.5 V
$\|a_{io}\|$	1.76 ± 0.11	5.03 ± 0.05	1.0 ± 0.2	1.0 ± 0.1	1.26 ± 0.03	2.35 ± 0.03
$\|b_{io}^{(2)}\|$	8.83 ± 0.04	8.84 ± 0.05	-	-	3.29 ± 0.03	3.30 ± 0.04
$\|c_{io}^{(2)}\|$	-	-	10.42 ± 0.04	10.47 ± 0.03	-	-
$\|b_{io}^{(4)}\|$	-	-	0.01 ± 0.04	0.01 ± 0.04	-	-
$\|c_{io}^{(4)}\|$	0.01 ± 0.04	0.06 ± 0.05	-	-	0.03 ± 0.02	0.01 ± 0.03

Table 4.1: Results from fitting the data of the figures 4.1(a), 4.1(b) and 4.1(c) to equation 4.1. For all parameters a_{io}, $b_{io}^{(m)}$ and $c_{io}^{(m)}$ the same arbitrary units have been used. Note however that the value of the parameters in the first two columns cannot be compared with those of the last two since different values of the laser power have been used for the P-in and the S-in measurements.

The fit results show that the $|b_{io}^{(2)}|$ and $|c_{io}^{(2)}|$ terms are independent of the applied bias, and thus of the electric field behind the interface. Comparison with table 3.1 shows that $\chi_{xyz}^{(eff)}$ and $\chi_{zxy}^{(eff)}$ are thus independent from changes in the static electric field, which means that the following tensor elements, with $i \neq j \neq k$ from equation A.11 are zero:

$$\Delta_{ijkz}^{(3)} = \Delta_{ijkzz}^{(4)} = \chi_{ijkzz}^{(4)} = 0 \tag{4.2}$$

This observation is in contradiction with the work of Qi *et al* [1] where a field dependence of $\chi_{xyz}^{(eff)}$ and $\chi_{zxy}^{(eff)}$ was observed. In their experiments however the field was changed by performing measurements on samples with different doping concentrations instead of applying a bias. Moreover the experiments were performed at only two fixed orientations of the sample instead of measuring the full anisotropy. In this way it is difficult to separate the different contributions. Probably Qi measured another, doping related, effect than the electric field.

The fit results from the P-in P-out and S-in P-out combinations show that a_{pp} and a_{sp} are bias dependent which means that only $\chi_{zxx}^{(eff)}$ and the combination of $\chi_{zzz}^{(eff)}$ and $\chi_{xxz}^{(eff)}$ are bias dependent (see table 3.1 and equation. A.11). These three tensor elements have a bulk part which depends linearly on the electric field in the bulk and an interface part (given by equation A.12) which depends quadratically on the electric field at the interface. These two parts can not be separated here, however the results of Monte Carlo simulations which will be presented in chapter 6 (figure 6.11 and figure 6.16) suggest that the bulk part has a considerable contribution in these tensor elements.

In conclusion an electric field dependence can be measured with second harmonic generation. This field dependence can be separated from a contribution which does not depend on the electric field by performing anisotropy measurements and fitting the results. Since the field dependence only appears with P-out polarization, and the largest SHG signal is measured with a P-polarized fundamental beam, the P-in P-out polarization combination is the most useful for time resolved experiments. For that reason the results of the P-in P-out measurements are analyzed in more detail in the following sections of this chapter.

4.2 The anisotropic contribution

The measurements presented in this and the following section have been performed on a sample with a layer composition '1' (with cap layer) from section 2.1. In these measurements the wavelength of the laser beam was 770 nm. Figure 4.2 shows the results for the absolute value of the anisotropic amplitude $|b_{pp}^{(2)}|$ for different combinations of the reverse bias, the laser power and the temporal width of the used laser pulses. The relative errors in the shown data are less than 1%.

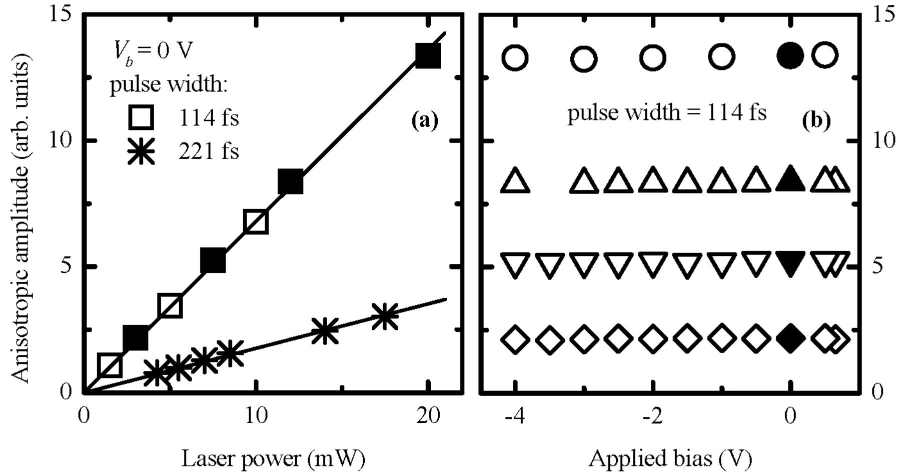

Figure 4.2: Fit results for the anisotropic amplitude $|b_{pp}^{(2)}|$, versus the laser power (a) and versus the reverse bias (b). The straight lines in figure (a) are fits. In figure (b) the circles present data at 20 mW laser power, the up triangles at 12 mW, the down triangles at 7.5 mW and the diamonds at 3 mW.

Combining the equations 2.1 and 3.11 gives for the second harmonic intensity $I_{2\omega}$ as a function of the laser intensity I_ω:

$$\sqrt{I_{2\omega}} = \left| a_{pp} + b_{pp}^{(2)} \sin 2\psi \right| = \sqrt{\eta_0} \left| \chi^{(2)} \right| I_\omega \tag{4.3}$$

When this equation is split into an isotropic and an anisotropic part, the anisotropic part is given by:

$$\left| b_{pp}^{(2)} \right| = \eta_1 \left| \chi_A^{(2)} \right| I_\omega \tag{4.4}$$

where η_1 is a constant and $\chi_A^{(2)}$ is the anisotropic part of $\chi^{(2)}$. Figure 4.2(a) shows $|b_{pp}^{(2)}|$ versus the laser power, which is directly proportional to I_ω, for two different values of the laser pulse width, at a constant applied bias of 0 V. The straight lines are linear fits through the origin of the figure. They show that the anisotropic amplitude, $|b_{pp}^{(2)}|$ is directly proportional to I_ω in equation 4.4. From this observation follows that the anisotropic part of the susceptibility tensor, $\chi_A^{(2)}$, and thus the tensor elements $\chi_{xyz}^{(eff)}$ and $\chi_{zxy}^{(eff)}$ from table 3.1 do not depend on the used laser power and thus on the excited density of carriers[1]. This observation is important as other people [1] claim that $\chi_{xyz}^{(eff)}$ and $\chi_{zxy}^{(eff)}$ depend on the doping concentration and thus could also depend on light induced carrier density.

The second harmonic output in terms of number of photons per pulse, $S_{2\omega}$, is given by:

$$S_{2\omega} = I_{2\omega}\ A\tau = \eta_0 \left| \chi^{(2)} \right|^2 I_\omega^2\ A\tau \tag{4.5}$$

where A is the area of the laser spot and τ is the temporal width of the laser pulses. Together with:

$$S_\omega = I_\omega\ A\tau \tag{4.6}$$

equation 4.5 gives:

$$\left| b_{pp}^{(2)} \right| = \eta_2 \sqrt{S_{2\omega}} = \eta_2 \sqrt{\frac{\eta_0}{A\tau}} \left| \chi_A^{(2)} \right| S_\omega \tag{4.7}$$

where η_2 is a constant. Figure 4.2(a) shows that the anisotropic amplitude is inversely proportional to the square root of the pulse width τ as is expected from equation 4.7.

Figure 4.2(b) shows results for four different values of the laser power, versus the reverse bias, measured with a laser pulse width of 114 fs. This figure again shows, for more values of the applied bias than in table 4.1, that the anisotropic amplitude and thus the anisotropic tensor elements are independent of the applied bias, and thus of the DC electric field in the sample.

---

[1] Even if only a probe beam is used, this probe beam also excites charge carriers in the depletion region. When the laser power is increased, the excited density of carriers also increases.

The dependence of the anisotropic amplitude on the laser power and on the pulse width show that the anisotropic contribution behaves as expected for second harmonic generation and does not show any carrier density induced effect. Since the anisotropic contribution is also independent of the applied bias and thus of the DC electric field behind the SB interface, the anisotropic contribution can be used for normalization of the field dependent isotropic contribution as will be shown in the next section.

4.3 The isotropic contribution

In accordance with the theory of chapter 3 and appendix A we see an electric field dependence in the isotropic contribution a_{io} to the SHG intensity. Due to the collapse of the field by the excited carriers we could therefore also expect to observe a dependence on the used laser power[2]. To separate the 'normal' quadratic SHG dependence on laser power, as described above for $|b_{pp}^{(2)}|$ and shown in figure 4.2, from the dependence, via a_{pp}, due to laser power induced changes in the electric field we have to separate both effects. Since the anisotropic amplitude $|b_{pp}^{(2)}|$ is directly proportional to $|E_p|^2$ and the tensor elements $\chi_{xyz}^{(eff)}$ and $\chi_{zxy}^{(eff)}$ are constant, the isotropic amplitude $|a_{pp}|$ can be normalized by dividing it through $|b_{pp}^{(2)}|$. Using equations A.13, A.17 to A.29 and 3.11 the normalized isotropic contribution $|a_{pp}^{'}|$ is given by:

$$|a_{pp}^{'}| = C_1 + C_2 E_z(z=0) + C_3 E_z^2(z=0) \tag{4.8}$$

In the following subsections the dependence of this normalized contribution on the relevant experimental parameters will be investigated to determine which conditions are optimal for the time resolved measurement of the electric field dynamics.

---

[2] See footnote 1.

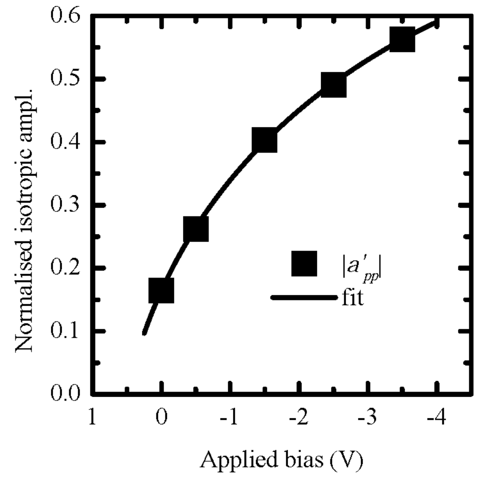

Figure 4.3: Fit results for the normalized (to $|b_{pp}^{(2)}|$) isotropic amplitude $|a'_{pp}|$, versus the reverse bias.

4.3.1 Bias dependence

Figure 4.3 shows the normalized interface contribution $|a'_{pp}|$ versus the applied bias. Substitution of the bias dependence of the electric field E_z in the depletion region a few nm behind the Schottky Barrier:

$$E_z(z=0) = \sqrt{\frac{2eN_D}{\varepsilon_0\varepsilon_r}(V_{bi} - V_b - \frac{k_BT}{e})} \tag{4.9}$$

in equation 4.8 gives the following expected bias dependence of $|a'_{pp}|$:

$$|a'_{pp}| = C_1 + C_2\sqrt{\frac{2eN_D}{\varepsilon_0\varepsilon_r}(V_{bi} - V_b - \frac{k_BT}{e})} + C_3\left(\frac{2eN_D}{\varepsilon_0\varepsilon_r}(V_{bi} - V_b - \frac{k_BT}{e})\right) \tag{4.10}$$

In these equations $\varepsilon_0\varepsilon_r$ is the dielectric constant of the semiconductor, N_D is the doping concentration (10^{17}cm^{-3}), $V_{bi} = e\phi_B - (E_C - E_F)$ is the built in potential (see figure 3.1(b)), V_b is the externally applied bias (see figure 3.1(c)), k_B is the Boltzmann constant and T is the temperature. Using formulas from Sze [2] $V_{bi} - (k_BT)/e$ at room temperature is calculated to be equal to 0.8 V. The line in figure 4.3 is a fit, according to equation 4.10 with C_1, C_2 and C_3 as fitting parameters. The fit results are given in table 4.2. These fit results show that the measured data points agree with the expected bias dependence of $|a'_{pp}|$. This agreement indicates that the isotropic component indeed

parameter	value		
C_1	-0.28 ± 0.02		
C_2	(34 ± 2)	$\times10^{-9}$	m/V
C_3	(-27 ± 2)	$\times10^{-17}$	m^2/V^2

Table 4.2: Results from fitting the data of figure 4.3 to equation 4.10.

measures the electric field in the depletion region just behind the interface[3].

In the time resolved experiments (chapters 5 and 6) the rotation angle ψ of the sample will be kept constant at an angle where the largest sensitivity to changes in the electric field is observed. For P-in P-out this angle is 135° (see figure 4.1(a)). At this rotation angle the (110) axis of the sample is in the plane of incidence. In this situation the anisotropic, electric field independent, signal is maximal. Due to the cross term between this large contribution and the smaller isotropic contribution also a relatively large electric field dependent signal can be measured. With equation 4.1 and the results of table 4.1 the E-field dependent second harmonic intensity $I_{2\omega}$ at this rotation angle is given by:

$$I_{pp}(E_z) = \left|a_{pp}(E_z) - b_{pp}^{(2)}\right|^2 \tag{4.11}$$

After normalization to $|b_{pp}^{(2)}|$ equation 4.11 transforms to:

$$I_{pp}(E_z) = \left|b_{pp}^{(2)}\right|^2 \left(\left|a'_{pp}(E_z)\right|^2 - 2\left|a'_{pp}(E_z)\right|\cos(\phi) + 1\right) \tag{4.12}$$

where ϕ is the phase angle between a_{pp} and $b_{pp}^{(2)}$, which is 135° in this case[4]. Figure 4.4 gives the result when equation 4.8 and the values of table 4.2 are substituted in equation 4.12. This figure clearly shows that the second harmonic intensity $I_{2\omega}$ depends linearly on changes in the electric field. This linear dependence is only valid for the P-in P-out polarization combination, at an rotation angle of 135°and for the field range which is shown in the figure. In the experiments with the samples '1' and '2' however the field will never be higher[5] than 400 kV/cm.

This linear dependence of $I_{2\omega}$ on the DC field in the depletion region is a big advantage for the time resolved measurement of the electric field dynamics. In those experiments a pump and a probe beam will be used and the aim is to measure the variations of the electric field versus the time delay between the pump and probe beam. Since for the above given polarization combination and sample orientation the

---

[3] Remember that the escape depth for the SHG light is less than 20 nm and thus only the field just behind the interface can be probed.

[4] This phase angle follows from fitting a full anisotropy curve with equation 4.1.

[5] The doping concentration in sample '3' is five time higher and consequently the field is more than two times higher. For this sample also the coefficients C_1 to C_3 are different.

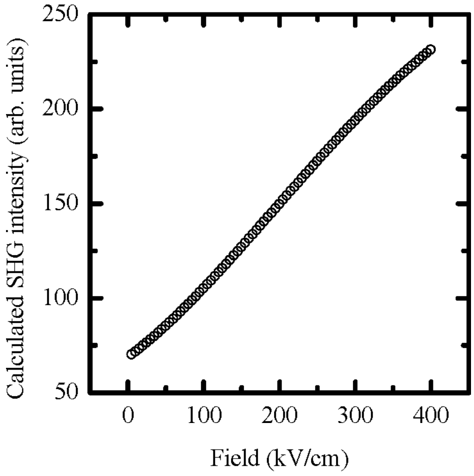

Figure 4.4: Calculated field dependence of $I_{2\omega}$ for a P-in P-out polarization combination and at a fixed rotation angle of 135°.

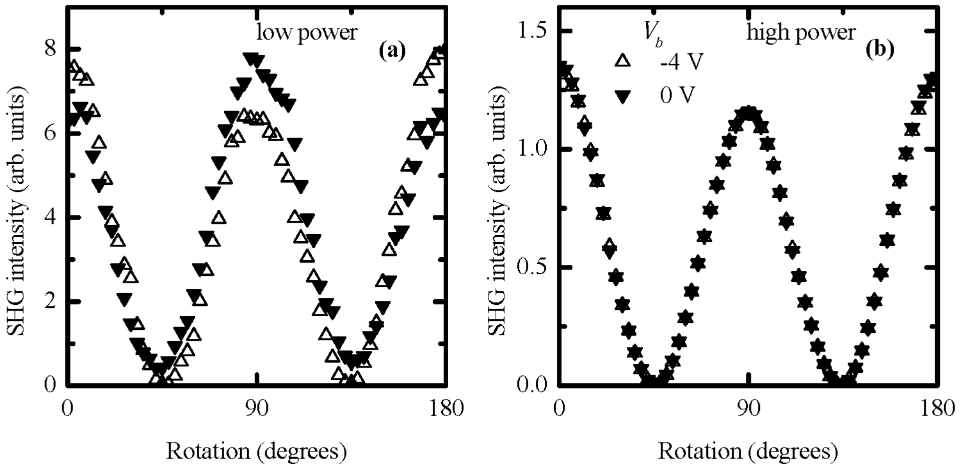

Figure 4.5: Anisotropy results with two different values of the applied bias and two different values of the laser power. The polarization is P-in P-out. In figure (a) the laser power is 4.5 mW and in figure (b) it is ten times larger. Only one half of the full anisotropy curve has been plotted.

$I_{2\omega}$ depends linearly on the electric field, it is no longer necessary to measure full anisotropy curves at every time delay step and fit them to equation 4.1 afterwards to separate the field dependent and field independent part. The field variations can now be determined directly from the changes in $I_{2\omega}$.

4.3.2 Laser intensity and pulse width dependence

As mentioned before, the probe beam will not only generate a field dependent SHG signal, but will also excite charge carriers. These carriers will influence the electric field and the probe beam can thus disturb the correct measurement of the electric field. To determine the influence of this effect, anisotropy experiments have been performed with different values of the probe beam intensity. The results, which are plotted in figure 4.5, show that the bias dependence of the SHG intensity decreases when the laser power is increased. This decrease can be understood as follows: The excited carriers will cause a collapse of the electric field as is explained in chapter 3. The time period in which this collapse takes place can be as short as the laser pulse width as is schematically illustrated in figure 4.6 for two different values of the excitation intensity and the pulse width. The hatched area represents the width of the laser pulse which excites the carriers, as well as probes the field. In figure 4.6(a) the pulse is short, 40 fs, and the effect of excitation of carriers on the SHG signal generated by the same pulse is minimal since it takes a finite time after the onset of the pulse before the field

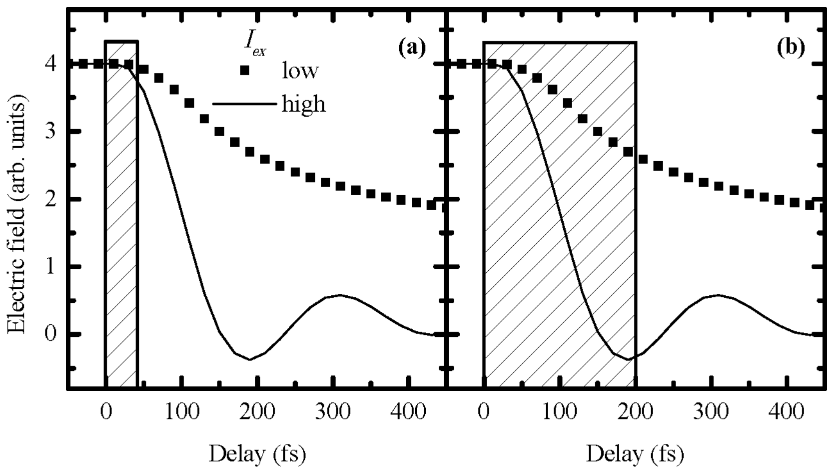

Figure 4.6: Schematic time dependence of the electric field after excitation of carriers for two different values of the excitation intensity. The hatched boxes represent the width of the used laser pulses. In figure (a) this pulse width is about 40 fs and in figure (b) it is five times larger. In both figures 0 fs along the horizontal axis is the onset of the laser pulse.

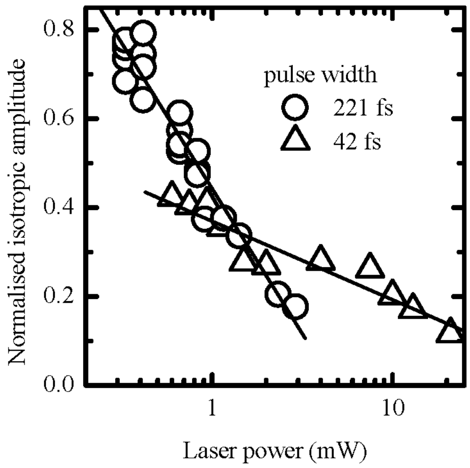

Figure 4.7: Fit results for the normalized isotropic amplitude $|a'_{pp}|$, versus the value of the laser power for two different values of the laser pulse width. In these experiments a bias of -4 V has been used.

collapses. Figure 4.6(b) shows the same for a laser pulse which is five times longer. In this figure the field collapses during the pulse and the effect of a higher density of excited carriers will be clearly visible on the amplitude of the SHG signal. The pulse width in the experiments of figure 4.5 was in between these two extrema. From these schematic figures we expect that the dependence on the excitation intensity is much stronger when long pulses are used.

To check this idea, anisotropy measurements have been performed with short, 42 fs, and long, 221 fs, pulses. Figure 4.7 shows the excitation dependence of the normalized interface contribution, for the two values of the pulse width. As expected the dependence on the excitation intensity is much stronger for the long pulses.

Since in pump probe experiments, the probe pulse should only measure changes in the electric field due to the pump pulse and not due to the probe pulse itself, we can conclude that the pulse width of the probe should be kept well below 70 fs.

4.3.3 Wavelength dependence

To check if spectral features appear in the electric field induced second harmonic generation, the wavelength dependence of the electric field induced SHG has been studied. P-in P-out anisotropy measurements have been performed for fundamental wavelength values ranging from 720 nm to 1140 nm[6]. The spectral response of the optical filters is not flat, and also the sensitivity of the photomultiplier tube depends on the wavelength of the SHG light. This wavelength dependence of the setup makes the direct comparison of the SHG intensity at different wavelengths difficult. To solve this problem the isotropic contribution is again normalized by dividing through the anisotropic contribution and in this way the spectral variations due to the measurement setup are divided out[7]. Figure 4.8(a) shows the results for the normalized isotropic contribution versus the wavelength for two different values of the applied bias. Figure 4.8(b) shows the results for the fit of the phase angle between the isotropic and anisotropic contributions a_{pp} and $b_{pp}^{(2)}$ of equation 4.1. The -3 V curve in figure 4.8(a) shows a resonance like feature at a fundamental wavelength of about 850 nm. The same feature is visible in figure 4.8(b) for both values of the applied bias. In other materials excitons are giving such kind of resonances [5]. The photon energy however at which the resonance appears in our experiments is about 50 meV higher than the value of the direct bandgap E_g^Γ. Also the fact that our experiments have been performed at 300 K excludes excitons to be the origin of the resonance. The energy of the resonance, 1.47 eV, is much smaller than the $\Gamma_8 - \mathrm{L}_6$ indirect gap[8] (1.71 eV, [6]) or the $\Gamma_8 - \mathrm{X}_6$ indirect gap (1.90, eV [6]). The width of the direct gap at the L-point is 2.97 eV [6], which is 40 meV higher than the energy of a second harmonic photon at the resonance. Till now we have no idea what is the origin of this resonance.

In the time resolved experiments of the following chapters a wavelength of 850 nm has been chosen for the measurements on sample 2A since at this wavelength the SHG dependence on changes of the electric field appears to be largest (see figure 4.8(a)).

---

[6] From 720 nm to 980 nm the different mirror sets available for the Ti:Sapphire laser have been used. To generate the longer wavelengths from 1040 nm to 1140 nm, a homebuilt OPO system has been used [3]. For all wavelengths the laser power was between 3 mW and 6 mW and the pulse width was about 150 fs.

[7] When normalization is not possible, a reference crystal like quartz, which is known to have no spectral features in this spectral region, could be used to correct for spectral variations in the setup [4]. This last method however is much more complicated.

[8] See figure 3.2.

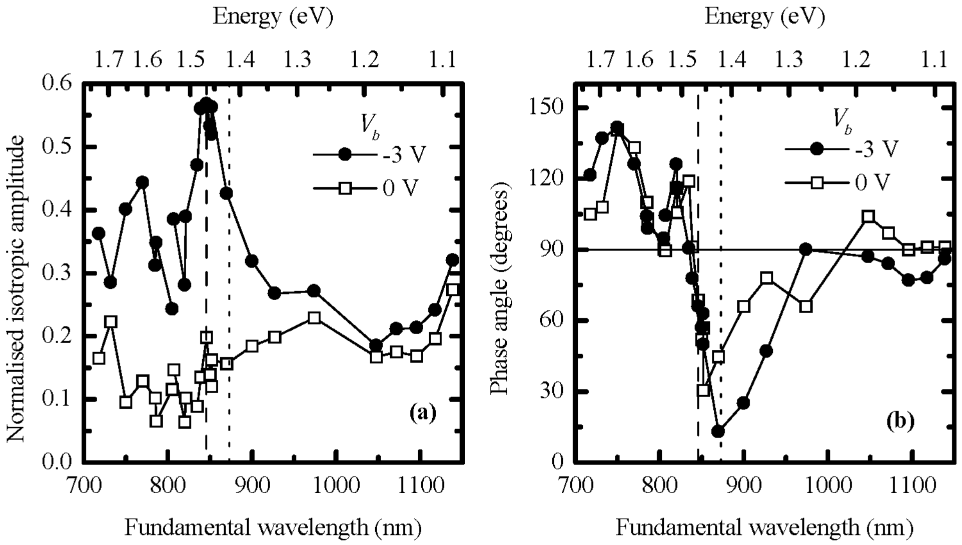

Figure 4.8: Fit results for: (a) the normalized isotropic amplitude $|a'_{pp}|$ and (b) the phase angle between the isotropic and anisotropic contributions a_{pp} and $b^{(2)}_{pp}$ versus the wavelength of the laser for two different bias values. The dashed line denotes a resonance like feature. The dotted line gives the position of the direct bandgap E^{Γ}_{g}. These experiments have been performed on sample 2A.

4.4 Conclusion

We have shown that SHG is a useful tool to probe the electric field dynamics in the depletion region behind a metal-semiconductor interface. By selecting the proper polarization combinations the different contributions to the SHG intensity are separable in anisotropy experiments. It appears that the anisotropic contribution which mainly comes from the bulk of the semiconductor is independent of the bias voltage or the laser intensity, and does not show any carrier density induced effect. The anisotropic contribution can thus be used to normalize the isotropic contribution which is dependent on the electric field. This normalized isotropic contribution (generated in the bulk and at the interface) appears to be proportional to the static electric field in the depletion region just behind the Schottky barrier interface. For some special polarization combinations and rotation angles of the sample the second harmonic intensity appears to be proportional to changes in the electric field due to an interference term between the anisotropic and the field dependent isotropic contribution. This proportionality gives the possibility to probe electric fields without measuring every time a full anisotropy curve. The power and pulse width dependence of this isotropic contribution shows that in time resolved pump probe experiments the power and the pulse width of the probe pulse should be kept as small as possible. An additional advantage above linear techniques, like reflective electro optic sampling (REOS) [7] is that these techniques only work in non centrosymmetric materials [8], while SHG also probes the electric field at silicon Schottky barrier interfaces [4, 9].

References

[1] J. Qi *et al.* Depletion-electric-field-induced changes in second-harmonic generation from GaAs. *Phys. Rev. Lett.*, **71**, 633–636, (1993).

[2] S. M. Sze. *Physics of Semiconductor Devices.* John Wiley and Sons, New York, 2nd edition, 1981.

[3] A. Anema. Ph.D. dissertation, Katholieke Universiteit Nijmegen, Nijmegen. to be published.

[4] P. Godefroy *et al.* Electric field induced second harmonic generation spectroscopy on a metal-oxide-silicon structure. *Appl. Phys. Lett.*, **68**, 1981–1983, (1996).

[5] A.-M. Janner. *Second-Harmonic Generation, a Selective Probe for Excitons.* Ph.D. dissertation, Rijksuniversiteit Groningen, Groningen, 1998.

[6] J. S. Blakemore. Semiconducting and other major properties of gallium arsenide. *J. Appl. Phys.*, **53**, R123–R181, (1982).

[7] L. Min and R. J. Dwayne Miller. Subpicosecond reflective electro-optic sampling of electron-hole vertical transport in surface-space-charge fields. *Appl. Phys. Lett.*, **56**, 524–526, (1990).

[8] C.-C. Shih and A. Yariv. A theoretical model of the linear electro-optic effect. *J. Phys. C*, **15**, 825–846, (1982).

[9] C. W. van Hasselt. *Nonlinear and linear optical studies of Si-SiO$_2$ interfaces.* Ph.D. dissertation, Katholieke Universiteit Nijmegen, Nijmegen, 1997.

Chapter 5

Time resolved measurement of electric field dynamics

In the previous chapter we have demonstrated that SHG is sensitive to bias induced variations in the depletion electric field of a Schottky barrier sample. In this chapter time resolved measurements of the electric field dynamics will be presented. These measurements have been performed at relatively low excitation intensities. The first paragraph starts with some experimental details and a demonstration that also in time resolved experiments only the isotropic contribution to the SHG signal is field dependent. In section 5.2 the results obtained from an $Al_{.2}Ga_{.8}As$ sample are discussed. In section 5.3 the results from a GaAs sample are discussed and compared with simulations. The experimental observations from this last sample are in good qualitative agreement with simulations.

5.1 Experimental details

The experimental setup for the time resolved experiments has been given in figure 2.5. As described in section 2.2.4, the SFG signal is measured to determine the temporal width of the laser pulses, < 70 fs, and to optimize the spatial overlap on the sample. With this SFG measurement also the zero-delay point between pump and probe pulses can easily be determined. Since the P-in P-out polarization is most useful to probe electric field dynamics[1], this combination has been used for all experiments presented in this chapter.

Two different kind of samples have been used. The first one has an $Al_{.2}Ga_{.8}As$ active layer (sample 3 from figure 2.1). This specific composition has a bandgap of 1.66 eV [1], which corresponds to a wavelength of 747 nm. The wavelength of the laser can be varied around this wavelength. During the experiments the current flow

---

[1] See the discussion on page 38.

through the sample is monitored. When the laser wavelength is varied around the 747 nm the effect on the current flow is clearly visible. Since only one wavelength is used for both the pump and the probe beam, and the pump beam has to excite charge carriers, a wavelength of 740 nm has been used to perform the time resolved experiments. This wavelength corresponds to a photon energy of 1.68 eV which is less than one LO phonon (36 meV) above the bandgap.

The other sample has a GaAs active layer (sample 2 from figure 2.1). This sample has a smaller bandgap of 1.42 eV, which corresponds to 873 nm. It is difficult to set the laser wavelength at this value while keeping the pulses short ($<$ 70 fs). Measurements on this sample have thus been performed at a wavelength of 840 nm, which gives the photons an excess energy above the bandgap of 50 meV. This second sample has no cap layer, which is an advantage for second harmonic generation. A cap layer consisting of two extra layers inherently gives two extra interfaces which means that there are two extra sources of second harmonic generation which makes it more difficult to interpret the results.

To estimate the density of charge carriers that is excited by the pump beam, the following procedure has been followed. First the power of the pump beam and the area of the laser spot is measured with the procedure described on page 14. Next the fraction of the incident power that is absorbed in the GaAs or $Al_{.2}Ga_{.8}As$ layer is calculated with a model developed by Prins and Wierenga [2]. This model takes multiple reflections in the different layers of the sample into account. Input parameters for the laser beam are wavelength, polarization state and angle of incidence. For the sample the thickness of the different layers (as given in figure 2.1) and their optical constants are input for the model. Every photon from the absorbed fraction is supposed to excite one electron to the conduction band. The amount of excited electrons, divided by the thickness of the layer and the area of the laser spot gives the density of excited carriers I_{ex}.

5.1.1 Comparison with anisotropy measurements

To determine the sensitivity to electric field changes on the sample with the $Al_{.2}Ga_{.8}As$ active layer, first an anisotropy measurement without a pump beam has been performed. Two anisotropy curves with 0 V and -3 V applied bias respectively, have been plotted in figure 5.1. These measurements are identical to the ones described in chapter 4. Fitting of the data to equation 4.1[2], shows that also at this sample, only the isotropic contribution a_{pp} is sensitive to electric field changes. From figure 5.1 it is clear that at a rotation angle of 135° the sensitivity to changes of the electric field is at a maximum[3]. In all time resolved experiments presented in this chapter the rotation angle of the sample is kept at this value.

Figure 5.2 shows typical results of such a time resolved experiment. In this

---

[2] $I_{pp} = \left| a_{pp} + b_{pp}^{(2)} \sin 2\psi \right|^2$. See chapters 3 and 4 and appendix A for details on the fit and the meaning of the different parameters.

[3] At this rotation angle the (110) axis of the sample is in the plane of incidence.

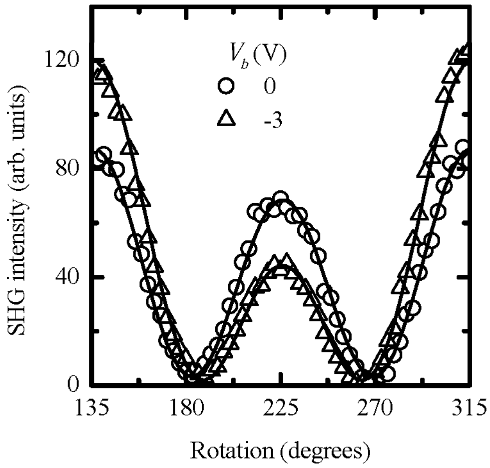

Figure 5.1: Anisotropy measurements without a pump beam on the $Al_{.2}Ga_{.8}As$ sample at a wavelength of 740 nm. The applied bias is 0 V for one curve and -3 V for the other. Only one half of the full anisotropy curve has been plotted.

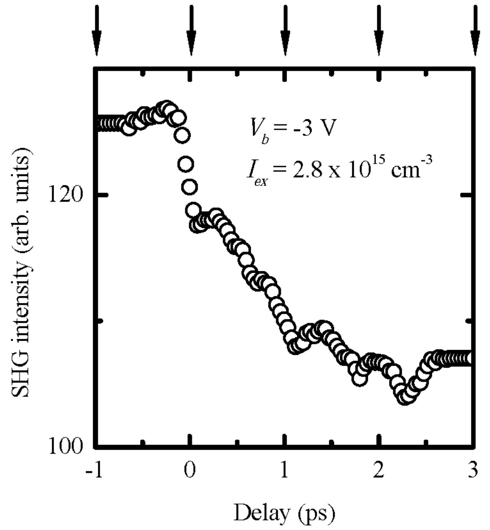

Figure 5.2: Typical pump probe measurement from -1 ps to 3 ps. The arrows denote the delay times where anisotropy measurements have been performed.

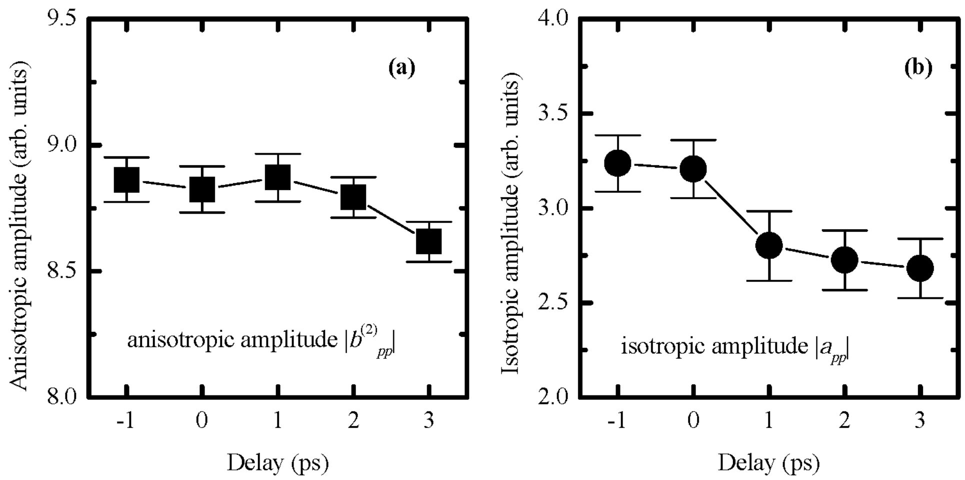

Figure 5.3: Fit results of the anisotropy measurements for different values of the delay between the probe and the pump beam. Figure (a) gives the anisotropic amplitude and figure (b) the isotropic amplitude. Note that the scales are different for the figures (a) and (b).

experiment the pump beam is also P-polarized. This pump beam was focused to about 120 μm diameter on the sample and the probe beam to about 65 μm diameter. The intensity of the pump is twelve times larger than the probe, giving an excited carrier density of 2.8×10^{15} cm^{-3}. For negative delay times the signal appears to be constant and the intensity of the pump beam is not influencing the signal at negative delay times[4]. Since the applied bias is -3 V in this experiment, the initial field and thus the SHG signal before excitation of the carriers are relatively high. After excitation of the electrons and holes the electric field in the depletion region drops fast due to separation of the carriers, resulting in a decreasing SHG signal. The final value at 3 ps consists mainly of the electric field independent (and thus time independent) anisotropic bulk contribution.

To check that also in the time resolved experiment only the isotropic contribution is changing, and not the anisotropic, again anisotropy measurements are performed, now with both a pump and a probe beam. These measurements have been performed for several, fixed, delay times between the beams. These delay times are: -1 ps, 0 ps, 1 ps, 2 ps and 3 ps. They are denoted by arrows in figure 5.2. The obtained data are again fitted to equation 4.1. The results for the anisotropic amplitude $|b^{(2)}_{pp}|$ and the isotropic amplitude $|a_{pp}|$ are shown versus the delay time in figures 5.3(a)

---

[4] The time between two pump pulses is 12 ns (= 12,000 ps) The fact that the pump is not influencing the signal at negative delay times means that the signal is fully recovered within these 12 ns.

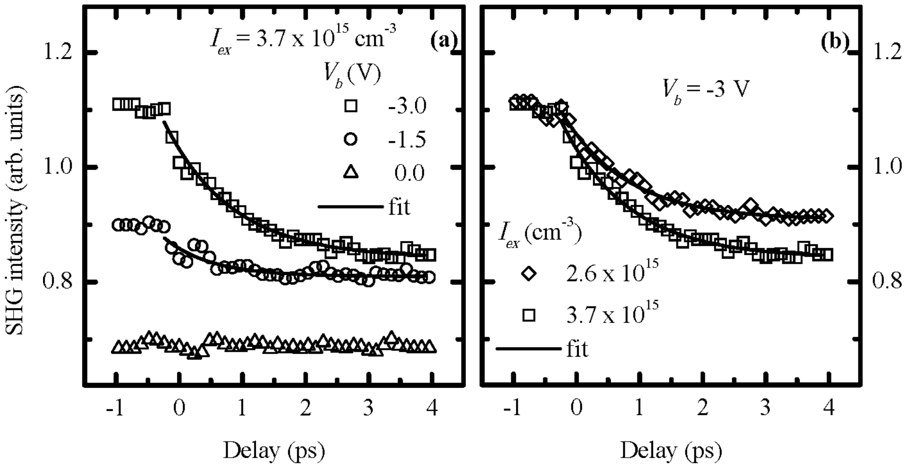

Figure 5.4: Time resolved experiments for: (a) different values of the applied bias and (b) the excitation intensity.

and 5.3(b). Figure 5.3(a) shows that the anisotropic amplitude is constant with in 3 %. This small variation is comparable with the fit results from figure 5.1 and figure 4.1. As expected, the isotropic amplitude changes much more, namely more than 15 %. From this observation it can be concluded that only the isotropic contribution decreases when the depletion field collapses due to the excitation of carriers, which is consistent with the experiments of chapter 4, where the depletion field was manipulated by changing the applied bias.

5.2 Results on the AlGaAs sample

Figure 5.4 shows time resolved measurements performed for different values of the applied bias and of the excitation intensity. Figure 5.4(a) shows results with a constant excitation intensity of 3.7 × 10^{15} cm^{-3} and three different values of the applied bias. For the top curve the applied bias is -3 V, corresponding to an initial field of about 700 kV/cm at the metal-semiconductor interface. In the middle curve the applied bias is -1.5 V, resulting in a lower initial field, and thus a lower SHG signal before excitation. In the lowest curve, with an applied bias of 0 V, the initial field is again lower, but not zero due to the Schottky effect. In this curve no effect of the excitation of carriers is visible, most probably due to the low excitation intensity. The 'final' values at a delay of 4 ps are not equal for the three curves, which means that the excited density of carriers is not high enough to screen the field at the interface completely. Figure 5.4(b) shows time resolved measurements with a fixed value for

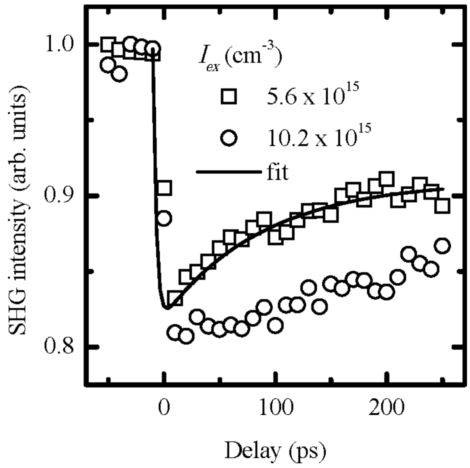

Figure 5.5: Time resolved experiments, with very long delay times, for different values of the excitation intensity. The curves are normalized to 1 at negative time delays.

the applied bias, but different values for the excitation intensity. These results indeed show that, in this intensity regime, the final value of the electric field is lower when the excitation intensity is higher.

In figure 5.5 results have been plotted which have been measured for much longer time delays than shown in figure 5.4. Here also the recovery of the signal can be followed. From this figure it is clear that for higher excitation intensity the minimum is still lower, and the recovery is slower than in the case of two times lower excitation.

The measured time dependence of the $I_{2\omega}$ data can be fitted with a double exponential (solid lines in the figures 5.4 and 5.5). These fits give one time constant for the collapse, τ_c, and one for the recovery, τ_r, of the electric field. Experimentally, τ_c is found to be 400 fs for the highest intensity used and 1 ps for the lowest one, which is the lower curve in figure 5.4(b). The measured τ_r appears to be 90 ps for the fit which has been shown in figure 5.5.

Monte Carlo simulations have been performed to calculate the time dependence of the electric field for different values of the incident laser intensity. The subsequent transport and energy relaxation of the photo-excited carriers in the $Al_{.2}Ga_{.8}As$ layer are computed, accounting for the various scattering mechanisms[5]. Both electron-heavy- and -light-hole pairs are considered, including hole inter band transitions. The results of the simulations have also been fitted with an exponential decay and recovery to compare them with the experimental results. The time constants for the collapse

---

[5] The details of these simulations have been described in section 3.3.

which follow from the simulations, are about 2 times shorter than the constants from the experiments. From the simulations the recovery of the electric field is expected to have a time constant of 20 ps, which is almost five times faster than experimentally observed.

A possible explanation of the longer time constants τ_c and τ_r found in the experiment when compared to the simulations is the existence of DX centers in n-doped $\mathrm{Al}_x\mathrm{Ga}_{1-x}\mathrm{As}$. In $\mathrm{Al}_x\mathrm{Ga}_{1-x}\mathrm{As}$ with $x > 0.22$ the DX center is a donor level lying below the Γ minimum of the conduction band [3]. For $x = 0.2$ as is the case in our sample, the energy level of the DX center lies just above the band edge. However in the presence of an electric field it can still trap electrons [4]. When illumination of the $\mathrm{Al}_{.2}\mathrm{Ga}_{.8}\mathrm{As}$ sample was started, the current through the sample increased exponentially with a time constant in the order of seconds. When the illumination was stopped the current also decreased in an exponential like way. This effect is the so called persistent photoconductivity (PPC) which is a strong evidence for the existence of DX centers [3, 5]. These DX-centers will also influence the ultrafast electric field dynamics. When the pump pulse excites electrons, part of these electrons are trapped immediately. These trapped electrons delay the charge separation and thus the collapse of the field. Electrons which are moving away from the interface (due to the internal depletion field) can be trapped further in the bulk of the $\mathrm{Al}_{.2}\mathrm{Ga}_{.8}\mathrm{As}$. These electrons will delay the recovery of the signal considerably. In future simulations the effect of these DX-centers could be incorporated to obtain a better quantitative description of the experimental results obtained on $\mathrm{Al}_{.2}\mathrm{Ga}_{.8}\mathrm{As}$ samples [6, 7].

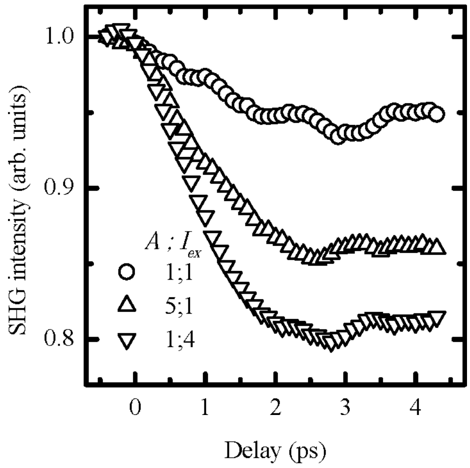

Figure 5.6: Time resolved experiments for different values of the excitation intensity and the spot size of the pump beam. $A = 1$ corresponds to an area of $3.7{\times}10^{-5}$ cm^2, $A = 5$ corresponds to $19.6{\times}10^{-5}$ cm^2. $I_{ex} = 1$ corresponds to an excitation density of $1.0{\times}10^{16}$ cm^{-3}, and $I_{ex} = 4$ corresponds to $4.0{\times}10^{16}$ cm^{-3}.

5.3 Excitation intensity and spot size dependence

The recovery of the surface charge, which also determines the recovery of the collapsed field, depends among other things on the thickness of the Au-layer and the area of the excitation laser spot (see chapter 3). The thickness of the Au-layer could not easily be varied, but the area of the laser spot could.

In this section results will be presented for different excitation intensities and different sizes of the laser beam. To avoid the problems with the DX centers which have been described in the previous section the experiments which will be described in this section have been performed on a sample with a GaAs active layer; 'Sample 2A'. A wavelength of 840 nm has been used, corresponding to a photon energy of 1.47 eV, which is about 50 meV above the direct bandgap of GaAs. The pulse width is 60 fs. Figure 5.6 shows experimental results for three different combinations of the pump spot area, A, and the excitation intensity, I_{ex}, of the pump laser beam. The diameter and intensity of the probe beam are kept constant at 65 μm (probe area = 3.3×10^{-5} cm^2) and 1.5 mW respectively. In these measurements the applied bias is -3 V. In the upper curve the area A of the pump beam is 3.7×10^{-5} cm^2, or in a short hand notation 1 arb. unit. The excitation intensity I_{ex} for this curve is 1.0×10^{16} cm^{-3} (1.3 mW), or 1 arb. unit. In the middle one these values are 19.6×10^{-5} cm^2 (= 5 arb. units) and 1.0×10^{16} cm^{-3} (6.5 mW laser power, = 1 arb. unit), and in the lower one 3.7×10^{-5} cm^2 (= 1 arb. unit) and 4.0×10^{16} cm^{-3} (6.0 mW laser power, =

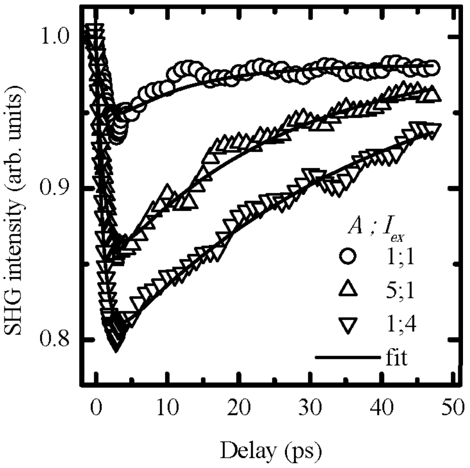

Figure 5.7: Time resolved experiments for different values of the excitation intensity and the spot size of the pump beam. The first 4 ps have been plotted on an extended scale in figure 5.6.

4 arb. units). The measured collapse of the SHG intensity can be fitted with a single exponential decay plus an offset. The results for τ_c are presented in the middle column of table 5.1. The two curves with the intensity '1' have more or less the same τ_c, and the curve with the intensity '4' has a little shorter τ_c. These values suggest that the collapse time only depends on the excitation intensity and not on the area of the pump beam.

A ; I_{ex}	τ_c (ps)	τ_r (ps)
1 ; 1	0.9±0.1	10.7±1.4
5 ; 1	0.86±0.05	24.6±2.7
1 ; 4	0.74±0.04	38.0±6.2

Table 5.1: Results from fitting the data of the figures 5.6 and 5.7 with a double exponential.

Figure 5.7 gives experimental results for the same combinations of area and intensity, but now also the recovery of the signal has been measured. These data have been fitted with a double exponential, yielding one time constant for the collapse (τ_c) and one for the recovery (τ_r) of the electric field. In these fits the collapse time constants τ_c were not varied but the results which were obtained from figure 5.6 have been used. The results of this fitting are presented in the last column of table 5.1.

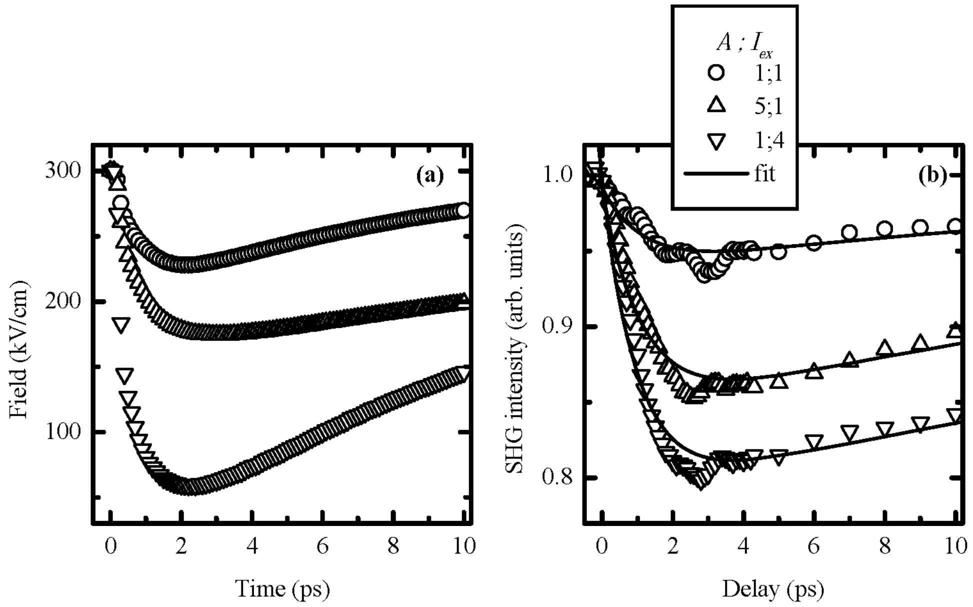

Figure 5.8: (a) Simulation results for different values of the excitation intensity and the spot size of the pump beam. (b) Experimental results for the same combinations of intensity and spot size. The results in this figure (b) have already been plotted in the figures 5.6 and 5.7 but have now been plotted on the same scale as the simulation results.

From these values it can be seen that the recovery time is considerably longer when the spot size is bigger while the excitation intensity is kept the same.

The measured time dependence of the SHG can be compared with the time dependent electric field which has been calculated with Monte Carlo simulations. The only adjustable parameter in these simulations is the regeneration time, which influences the recovery of the field after excitation. Based on the capacitance per area of the metallic top contact (520 μF/m^2), the sizes of the excitation beam (3.7×10^{-5} cm^2 and 19.6×10^{-5} cm^2) and the square resistance of the Au film (a few Ohms), the RC time constant of this process (the regeneration time) was estimated to be in the order of 10 to 30 ps. For $A = 1$ a regeneration time τ_{reg} of 8 ps has been used in the calculations. For $A = 5$ a time of 25 ps has been used.

Figure 5.8(a) shows the calculated time evolution of the electric field for an initial applied bias of -3 V for the same three combinations of the area A of the exciting spot and the intensity I_{ex} of the excitation as used in the experiment[6]. Comparison of this figure with figure 5.8(b) shows that for the upper and lower curve the measured decrease is equal to the calculated one. For the middle curve the measured minimum is lower than calculated, and the measured recovery is faster. These simulation results have also been fitted with a double exponential, giving the time constants τ_c and τ_r. These constants are presented in table 5.2, together with the time constants obtained from the experiment. Comparison of these time constants shows that the order of magnitude of the time constants appears to be correct. In almost all cases the measured time constants are longer than the ones from the simulation. Only in the case, where the spot area is five times larger than in the other cases, the measured τ_r is smaller than the one from the calculation as is also observable in the figure. In this case the simple RC time constant in the simulation is maybe too simple.

A ; I_{ex}	τ_c (ps)		τ_r (ps)	
	simulation	experiment	simulation	experiment
1 ; 1	0.49±0.02	0.9±0.1	11.4±0.3	10.7±1.4
5 ; 1	0.60±0.02	0.86±0.05	42.4±1.5	24.6±2.7
1 ; 4	0.32±0.01	0.74±0.04	21.7±0.7	38.0±6.2

Table 5.2: Results from fitting the data of the figures 5.8(a) and 5.8(b) with a double exponential.

5.4 Conclusion

The experimental results show a collapse and recovery of the time dependent SHG signal, after excitation of charge carriers. The magnitude of the collapse and the collapse time constant depend mainly on the excitation intensity. The recovery time constant of the system not only depends on the excitation intensity but also on the spot size as is predicted by the simulations and demonstrated in the experiments. Comparison of the experiments with Monte Carlo simulations shows that the decoupling constant which has been introduced in the simulations results in a very good description of the electric field dynamics. In the next chapter experiments with higher pump intensity are presented, to reach the regime where oscillations in the electric field are predicted by the simulations.

---

[6] The curves in this figure have already been corrected for the finite escape depth of the SHG light (see section 3.4).

References

[1] S. Adachi. GaAs, AlAs, and $Al_xGa_{1-x}As$: Material parameters for use in research and device applications. *J. Appl. Phys.*, **58**, R1–R29, (1985).

[2] H. A. Wierenga, M. W. J. Prins, and Th. Rasing. Magnetization-induced optical second-harmonic generation from magnetic multilayers. *Physica B*, **204**, 281–286, (1995).

[3] P. M. Mooney. Deep donor levels (*DX* centers) in III-V semiconductors. *J. Appl. Phys.*, **67**, R1–R26, (1990).

[4] T. N. Theis, B. D. Parker, P. M. Solomon, and S. L. Wright. Hot-electron capture to *DX* centers in $Al_xGa_{1-x}As$ at low Al mole fractions ($x < 0.2$). *Appl. Phys. Lett.*, **49**, 1542–1544, (1986).

[5] S. Ghosh and V. Kumar. Stretched exponential relaxation of persistent photoconductivity due to the Si-related DX centre in $Al_xGa_{1-x}As$. *Europh. Lett.*, **24**, 779–784, (1993).

[6] P. J. van Hall and E. A. E. Zwaal. Impact ionisation in the AlGaAs layer of GaAs/AlGaAs heterojunctions. *Superlatt. M.*, **13**, 323, (1993).

[7] P. J. van Hall and H. Kökten. A model for the current instabilities in GaAs-AlGaAs heterojunctions. *J. Appl. Phys.*, **79**, 1955–1960, (1996).

Chapter 6

Coherent plasmon phonon oscillations

In this chapter we present experiments using very intense laser excitation to reach the regime where plasma oscillations are expected. The first section gives experimental details and describes the problems with scattered light from the pump beam. In the second section we show that the expected oscillations indeed occur directly in the time resolved second harmonic signal. The dependence of the oscillation frequency on several experimental parameters is analyzed, which leads to the conclusion that the observed oscillations are plasmons. In the third section the experimental observations are compared with simulations. The simulations, in which the time dependent electric field is calculated, reproduce the oscillations very well. When in these Monte Carlo simulations the coupling between plasmons and phonons is included also the excitation intensity dependence of the frequency agrees perfect with the experimental results. In these simulations the only free parameter is the decoupling time constant, which has been determined in chapter 5.

6.1 Experimental details

In the experiments with a high excitation intensity, samples with the layer composition which is called 'sample 2' in figure 2.1 have been used. Since the Au-layers on the different samples were not deposited at the same time, their thicknesses may vary between 8 nm and 10 nm for the different samples. Due to multiple reflections of the fundamental light and the light at the second harmonic frequency the thickness of the gold layer can influence the amount of SHG light which is measured [1–4].

In most of the experiments described in this chapter, the wavelength of both the pump and the probe beam is 845 nm. The corresponding photon energy is 1.467 eV, which is about 47 meV above the bandgap of the sample. This excess energy is 11 meV more than the energy of an LO-phonon, which is 36 meV [5].

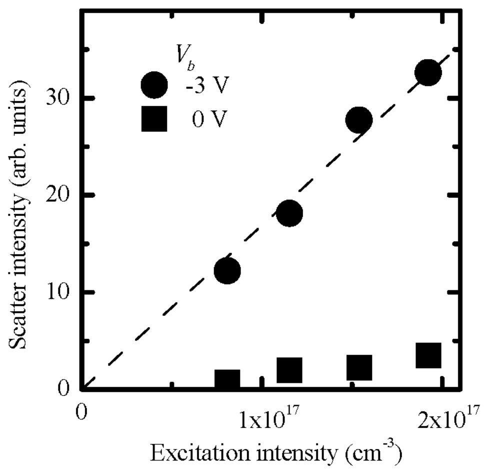

Figure 6.1: 'Scattered' light from the pump beam for different values of the excitation intensity and applied bias. In these experiments the probe beam was blocked.

Unless otherwise stated the following conditions have been used for the experiments presented in this chapter. The pump beam is S-polarized, the probe beam is P-polarized and the P-component of the second harmonic intensity is measured. Sample 2A is used, at a fixed rotation angle of 135°(with the (110) axis of the sample in the plane of incidence), and with an applied bias of -3 V.

6.1.1 Pump induced contribution

While increasing the excitation intensity to much higher values than used for the experiments of chapter 5 we encountered a problem, the origin of which is unknown up till now. At the excitation intensities which were used, the PMT was not only detecting SHG light generated by the probe beam, but also some kind of scattered light from the pump beam. The intensity of this signal was of the same order of magnitude as the SHG light generated by the probe beam. Figure 6.1 shows the power and bias dependence of this pump induced light. The effect of applying a bias is clearly visible: the intensity increased with a factor of 10 when the applied bias was increased from 0 V to 3 V reverse bias. The SHG bias dependence, which has been shown in figure 4.3, is much smaller. The intensity of this scattered signal increased almost linearly with the intensity of the pump beam, which is different from the expected quadratic behavior for the SHG signal intensity as shown in figure 4.2[1].

---

[1] Figure 6.1 shows intensity versus laser power while figure 4.2 gives amplitude versus laser power, and the intensity is the amplitude squared.

Measurements with different color filters in front of the PMT showed that the wavelength of this signal was in the same range as the SHG signal, which excludes normal photo luminescence to be the origin, since the photon energy of light at the second harmonic frequency is much higher than the band gap of GaAs[2]. The temporal width of the signal has not been measured. At a p-type sample (doping concentration = 10^{19} cm^{-3}) without a gold layer, the same phenomenon was observed. At the relatively low excitation intensities which were used in the experiments presented in the previous chapter this effect was negligible. In conclusion this background signal is generated at the sample, but the mechanism is unknown at the moment.

To subtract this signal from the SHG signal which is generated by the probe beam, the chopped counting technique which was described in section 2.2.4 has been used for all measurements which will be presented in this chapter.

6.2 Experimental results

Figure 6.2(a) shows the time evolution of the SHG signal for two different values of the excitation intensity. The solid lines in this figure are fits with a single exponential. The fit results for the collapse time constant are shown in figure 6.2(b) as a function of the excitation intensity.

From the figures (a) and (b) it is clear that when the excitation intensity is increased the collapse time is decreasing. This phenomenon has already been shown in chapter 5 for the low excitation intensities (10^{15} cm^{-3}), and continues at the higher intensities (10^{17} cm^{-3}). The difference between both intensity regimes is shown in figure 6.3(a). This figure shows experimental data with an excitation intensity of 4.6×10^{17} cm^{-3}, measured with much smaller time steps than figure 6.2(a). An oscillatory structure is clearly visible. After subtraction of a single exponential for the overall collapse, the oscillations become very pronounced, as is shown in figure 6.3(b). These oscillations are expected to be due to plasma oscillations, as described in chapter 3.

The solid line through the data points of figure 6.3(b) is an, exponentially, damped sine fit[3]. This fit shows that there is only one dominant frequency. To obtain the frequency of the oscillations a discrete Fourier transform (DFT) [6] is performed on the data[4]. Figure 6.4 shows the DFT of the data of figure 6.3(b). It shows a clear peak at 7.5 THz. The small peak below 2 THz is an artefact which depends on the agreement between the overall decay of the measured data and the single exponential which is subtracted[5]. The finite width of the peak at 7.5 THz is due to the finite length of the time domain signal. Figure 6.3(b) clearly shows that the oscillation is damped

---

[2] 1.42 eV versus 3 eV.

[3] The small peak at the left of figure 6.3(b) represents the laser pulses used for both the pump and the probe, which both have the same width of 50 fs.

[4] Before performing the DFT a single exponential is subtracted from the measured data points. In the DFT calculations a Hamming window [7] is used to minimize artifacts due to the finite extent in the time domain of the experimental data.

[5] This small peak also depends on the kind of window which is used while calculating the DFT.

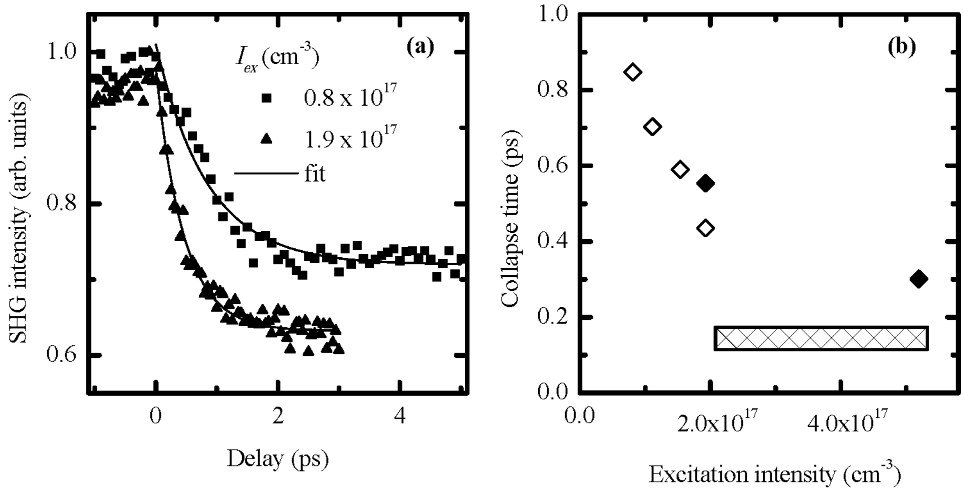

Figure 6.2: (a) Time resolved SHG signal for two different values of the excitation intensity, with an applied bias of -3 V. The solid lines are single exponential fits. (b) Fit results from the single exponential fits, for different values of the excitation intensity. The hatched bar indicates the region where oscillations occur.

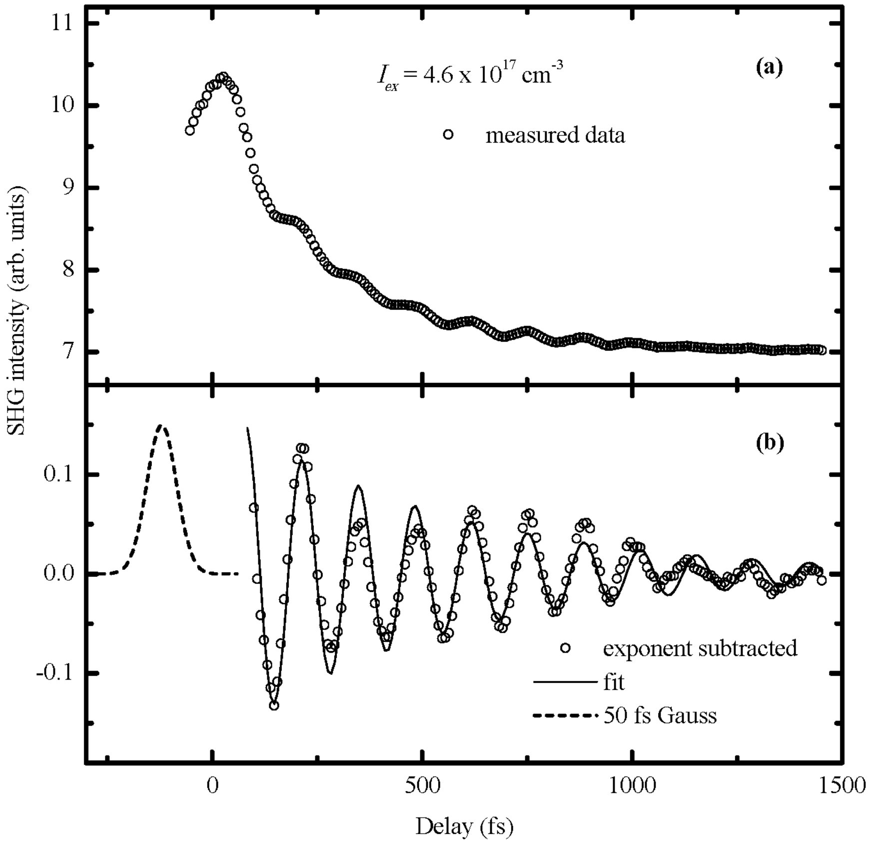

Figure 6.3: (a) Typical result from a pump probe measurement at high excitation intensity (measured on sample 2B). (b) Result after subtraction of a single exponential from the data of figure (a), the solid line is a fit with an exponentially damped sine with only one frequency. (The peak on the left hand side of figure (b) represents a 50 fs Gaussian laser pulse.)

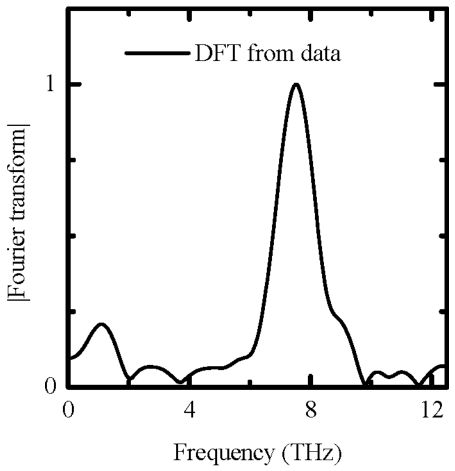

Figure 6.4: DFT results from the experimental data of figure 6.3(b).

and thus the length in the time domain, where the oscillation amplitude is larger than the noise, is not more than 2 ps.

To check that the observed oscillations are caused by plasmons and not by other phenomena, a series of time resolved experiments have been performed. In these experiments the following parameters were varied:

- The sample, to see how well the oscillations reproduce in different samples.
- The polarization of the pump beam and the orientation of the crystallographic axes of the sample. Plasma oscillations should not depend on the polarization of the excitation laser beam, while phonon oscillations do [8].
- The wavelength of the pump and probe beams. The wavelength of the pump beam influences the excess energy of the excited carriers and is supposed to influence the plasma oscillations [9].
- The bias applied to the sample, which affects the driving force for the excited carriers, see chapters 3 and 5.
- The excitation intensity. The frequency of plasma oscillations depends on the density of excited carriers, while the frequency of phonon oscillations does not [10, 11].

The experimentally observed dependence on each of these parameters is presented in the following paragraphs.

6.2.1 Sample dependence

In the figures 6.5(a) and 6.5(b) experimental results obtained from two different samples are given. Both samples are from the same wafer, however the gold layers on both samples have not been deposited at the same time, which means that the gold layers, and the intermediate oxide layers, may differ in thickness. Figures 6.5(c) and (d) show the result after subtraction of a single exponential from the data of figures 6.5(a) and (b). Comparison of the figures (c) and (d) shows that on both samples the same oscillations, with comparable frequencies, have been measured. A difference however between the figures 6.5(a) and (b) is the peak around 0 fs in figure (a), which is absent in figure (b). This phenomenon can be due to multiple reflections in the thin gold layer, or due to interference in this gold layer. An explanation for the observed time dependence of this peak could be the relative phase between the different SHG contributions. As presented in figure 4.8, this phase angle depends sometimes on the electric field which is present at the Au-GaAs interface. This field is time dependent due to the excitation of the carriers.

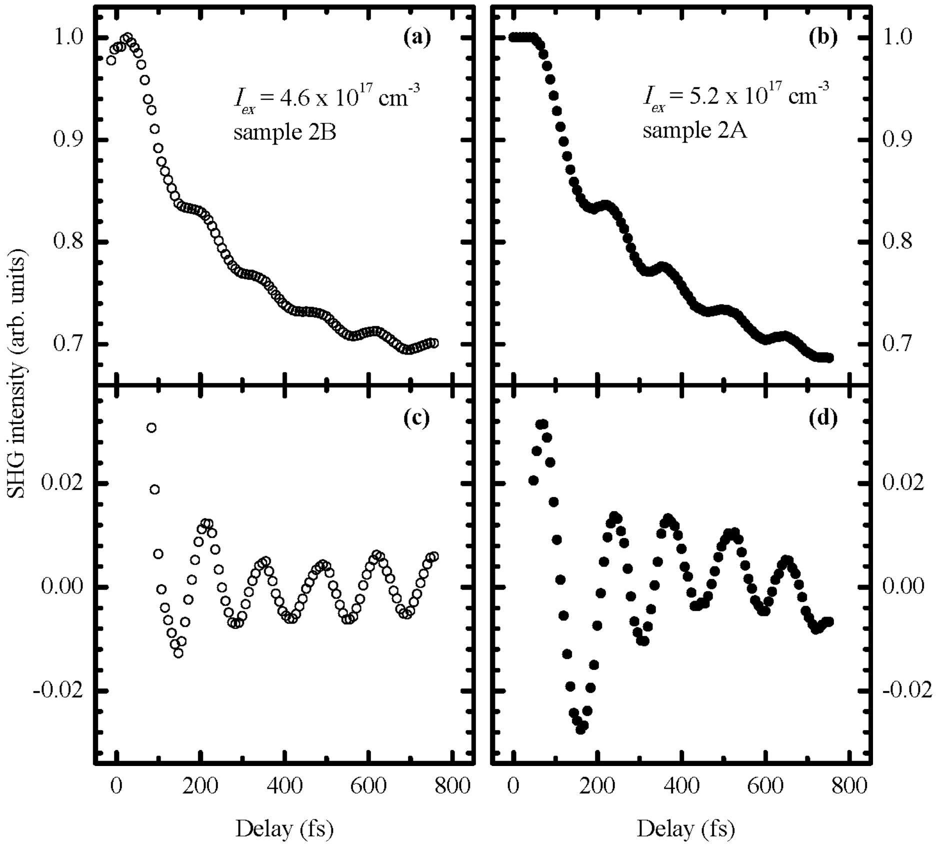

Figure 6.5: Experimental results from two different samples. The figures (c) and (d) show the oscillations after subtraction of a single exponential from the data shown in (a) and (b).

6.2.2 Polarization and orientation dependence

Figure 6.6 shows experimental results for four different combinations of the polarization of the pump beam and the rotation angle ψ of the sample. The rotation angles[6] 90° and 135° refer to figure 4.1. The bottom panels of the figures 6.6(a) to 6.6(d) show the oscillations after subtraction of a single exponential. These figures show that oscillations appear for all four combinations of the pump beam polarization and rotation of the sample[7]. With equation 3.11 and table 3.1 the Second Harmonic Intensity $I_{p,p}$ for P-in, P-out polarization and $\psi = 90°$ is given by:

$$I_{p,p} = \left| a_{pp} + b^{(2)}_{pp} \sin 2\psi + c^{(4)}_{pp} \cos 4\psi \right|^2 = \left| a_{pp} + c^{(4)}_{pp} \right|^2 \tag{6.1}$$

From the fits to the data of figure 4.1 we found that $c^{(4)}_{pp}$ is zero which means that $I_{p,p}$ reduces to:

$$I_{p,p} = \left| a_{pp} \right|^2 \tag{6.2}$$

For $\psi = 135°$ $I_{p,p}$ is given by:

$$I_{p,p} = \left| a_{pp} + b^{(2)}_{pp} \sin 2\psi + c^{(4)}_{pp} \cos 4\psi \right|^2 = \left| a_{pp} - b^{(2)}_{pp} \right|^2 \tag{6.3}$$

As shown in figure 4.2(b), the anisotropic amplitude $b^{(2)}_{pp}$ is independent of the applied static electric field. The field dependence of a'_{pp} is described by equation 4.8. The absence of the $b^{(2)}_{pp}$ term in the figures (c) and (d) explains the weaker signal, which goes to zero, in these two figures[8].

Fourier analysis of the data of figures (a) and (c) gives the same shape of the Fourier transform and the same frequency of 6.6 THz for both cases, indicating that the oscillations are not dependent on the orientation of the sample. Comparison of the figures (a) and (b) and their Fourier transforms shows that the oscillations do not depend on the polarization of the pump beam which excites the carriers. This independence on pump beam polarization means that the driving mechanism for the oscillations cannot be stimulated Raman Excitation [8, 12] or the Franck-Condon effect [8, 13, 14]. Oscillations driven by these two mechanisms were observed recently by Chang *et al* [8] on clean GaAs(110) surfaces. In their measurements clear differences were observed for the different combinations of pump beam polarization and sample orientation.

A striking difference between the figures (a) and (b) ($\psi = 135°$) on the one hand, and the figures (c) and (d) ($\psi = 90°$) on the other hand, is the time delay where the collapse of the signal starts. In the figures (a) and (b) it is about 50 fs after the

---

[6] At 90° the (100) axis of the sample is in the plane of incidence and at 135° the (110) axis is in this plane.

[7] In figure (d) the oscillations are not very clear, but in the DFT they appear.

[8] $b^{(2)}_{pp}$ is a complex quantity so $\left| a_{pp} - b^{(2)}_{pp} \right|$ is not necessarily the difference between $|a_{pp}|$ and $\left| b^{(2)}_{pp} \right|$.

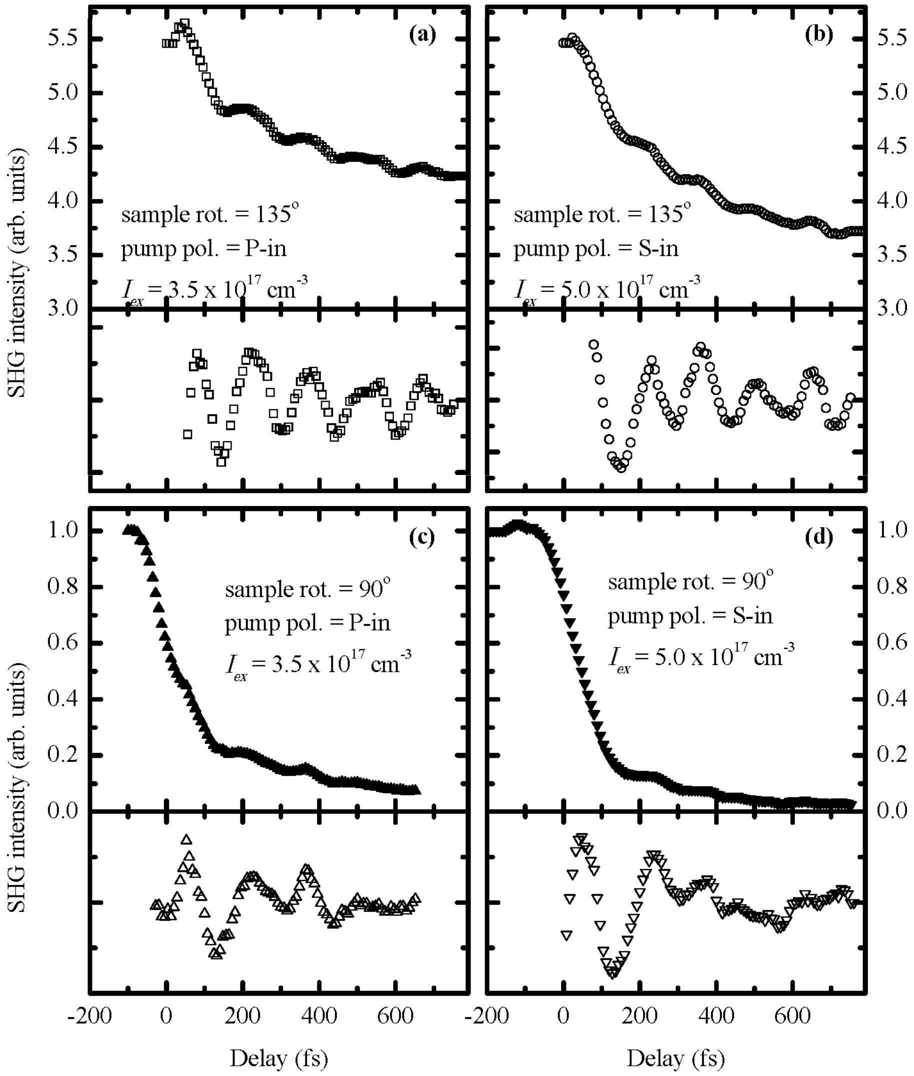

Figure 6.6: Experimental results for four different combinations of the sample orientation and the polarization of the pump beam. In the figures (a) and (b) the rotation of the sample is 135°. In the figures (c) and (d) the rotation is 90°. These angles refer to figure 4.1 on page 36. In the figures (a) and (c) the pump beam is P-polarized while in the figures (b) and (d) it is S-polarized. The bottom panels of the figures (a) to (d) show the oscillations after subtraction of a single exponential. Note that the vertical scales are different for the different figures, and that the signal in figures (c) and (d) goes to zero.

zero delay point, while in the figures (c) and (d) it is about 50 fs before this point. The only explanation we can think of at this moment is interference between the a_{pp} term and the $b_{pp}^{(2)}$ term.

In the P-in S-out polarization combination for the probe beam, with the sample rotation at 90° the second harmonic intensity $I_{p,s}$ is given by:

$$I_{p,s} = \left| c_{ps}^{(2)} \cos 2\psi + b_{ps}^{(4)} \sin 4\psi \right|^2 = \left| c_{ps}^{(2)} \right|^2 \tag{6.4}$$

In the time resolved experiments with this probe polarization combination no oscillations have been observed. This result is consistent with the observation in figure 4.1(b), were no effect of the static applied field was observed in the P-in S-out configuration.

6.2.3 Wavelength dependence

In figure 6.7(a) results are shown obtained with a wavelength for both the pump and the probe beam of 800 nm instead of the 850 nm which has been used in most experiments. A wavelength of 800 nm corresponds to a photon energy of 1.550 eV which is about 130 meV above the bandgap, or more than 3 LO-phonons. At this wavelength also oscillations appear. Figure (c) shows the result after subtraction of a single exponential. For comparison figures (b) and (d) show results obtained with a wavelength of 850 nm. The smaller amplitude of the oscillations in figure (c) is only partly due to the lower excitation intensity. It is mainly due to the lower sensitivity for changes in the electric field at a wavelength of 800 nm as is shown in figure 4.8(a). The observation of oscillations when the carriers are excited with a wavelength of 800 nm is in contradiction with results from Fischler *et al* [9]. In their work reflectivity changes of a probe beam, which has the same wavelength as the pump beam, have been measured. In their results oscillations were no longer observed at wavelengths shorter than 813 nm. The authors gave as an explanation, that at high excitation energies, where the excess energy is more than the LO-phonon energy, the electron-hole and electron-phonon scattering rates are increased. These increased scattering rates lead to a shorter momentum relaxation time and to a stronger damping, which explains the disappearance of the oscillations [9].

However the simulation results (which will be discussed in section 6.3) show that in the strong electric field (100 kV/cm), which exists in the interface region of the Schottky barrier samples, the excited carriers gain enough energy to scatter to the L and X side valleys within 100 fs after excitation. This time is comparable to the electron-phonon scattering time, and the energy needed to scatter to the side valleys is more than 7 LO-phonon energies. So we think that the higher excitation energy is not the reason for the disappearing oscillations. Moreover oscillations are observed with EFISHG at a wavelength of 800 nm. It would be interesting to use other wavelengths. However the range of wavelengths which could be used in our experiments was limited by the possibility to make short (50 fs) laser pulses which are necessary to measure the oscillations, especially when the amplitude of the oscillations is becoming smaller due to a lower sensitivity to changes in the electric field as is shown in figure 4.8(a).

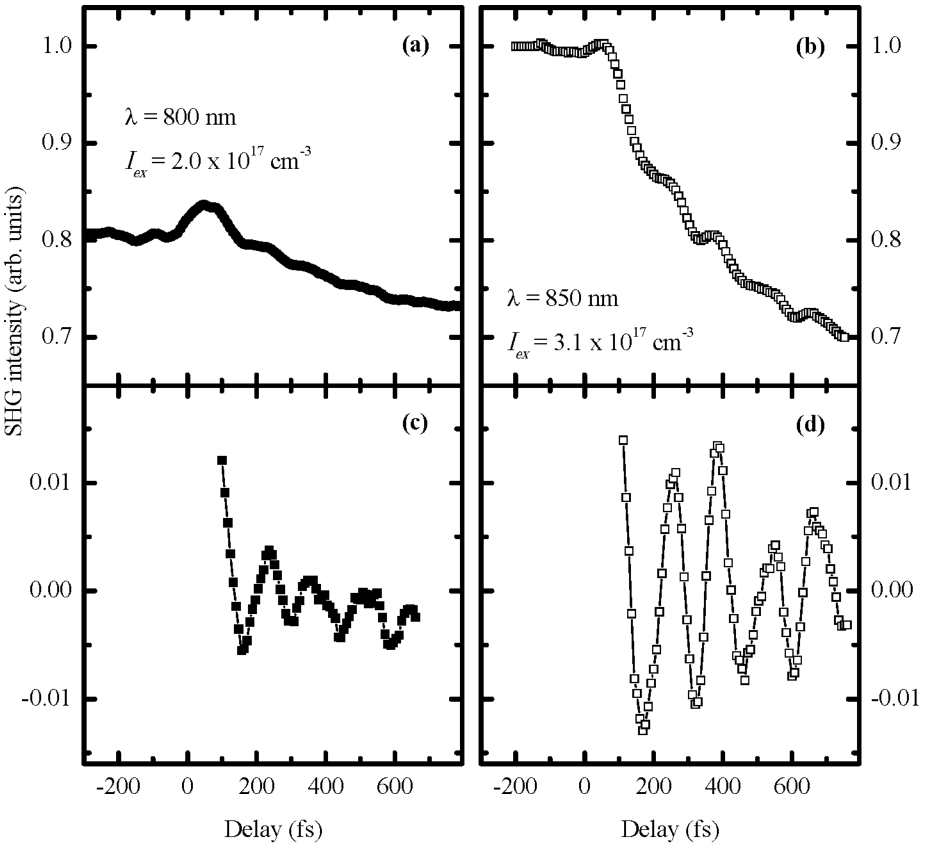

Figure 6.7: Experimental results for two different wavelengths of the laser beams. The top panels show the measured data points. The lower panels show the data after subtraction of a single exponential.

6.2.4 Bias dependence

The influence of the applied bias on the oscillations is shown in figure 6.8(a). Here the results for 0 V and -3 V applied bias are shown. The frequency of the oscillations is almost the same as can be seen in figure (b). In the case of 0 V applied bias only the amplitude is a bit smaller compared with the -3 V case. In both cases the excitation intensity is the same. These observations can be understood as follows: In a simple picture of plasma oscillations the frequency is only determined by the density of carriers, which is the same in both cases. The amplitude depends on the driving force of the oscillation, namely the electric field in the depletion region before excitation. When a bias of -3 V is applied this field is larger than when no bias is applied[9].

6.2.5 Intensity dependence

Figure 6.9 shows the dependence on the excitation intensity. As already shown in figure 6.2 the collapse is becoming faster when the excitation intensity is increased. As expected for plasma oscillations the frequency of the oscillations increases with increasing intensity: 5.7 THz in figure 6.9(c) and 7.1 THz in figure 6.9(d). The amplitude of the oscillations is also expected to increase with increasing intensity, however in the figures hardly any increase is visible. The finite width of the laser pulses that have been used to probe the oscillations, causes an observed amplitude which is decreasing while the frequency is increasing. We will come back to this point when discussing (on page 79) the figures 6.12 and 6.13.

In figure 6.10 the frequencies as obtained by Fourier transforming the experimental data have been plotted versus the square root of the density of carriers. The density range is limited on the low side by the signal to noise ratio of the measurement technique. On the high intensity side sample damage is the limitation[10].

The dashed line in figure 6.10 gives the density dependence of pure plasma oscillations, given by [15]:

$$\omega_p^2 = \frac{ne^2}{\varepsilon_0 \varepsilon_r m^*} \tag{6.5}$$

where ω_p is the plasma frequency, n is the carrier density, e is the electronic charge, $\varepsilon_0 \varepsilon_r$ is the dielectric constant, and m^* is the effective mass. This figure shows that the observed frequencies are quite near the values which are expected for pure plasma oscillations without effects of an inhomogeneous field. However the agreement is becoming less good for carrier densities below $5 \times 10^{17} \text{cm}^{-3}$.

---

[9] When no bias is applied the electric field is not zero, due to the Schottky field at the interface between the Au and the GaAs.

[10] When the excitation intensity is too much increased the sample is damaged, resulting in an increase of the current flow through the sample, and an irreversible decrease of the generated second harmonic light, even after blocking the pump beam.

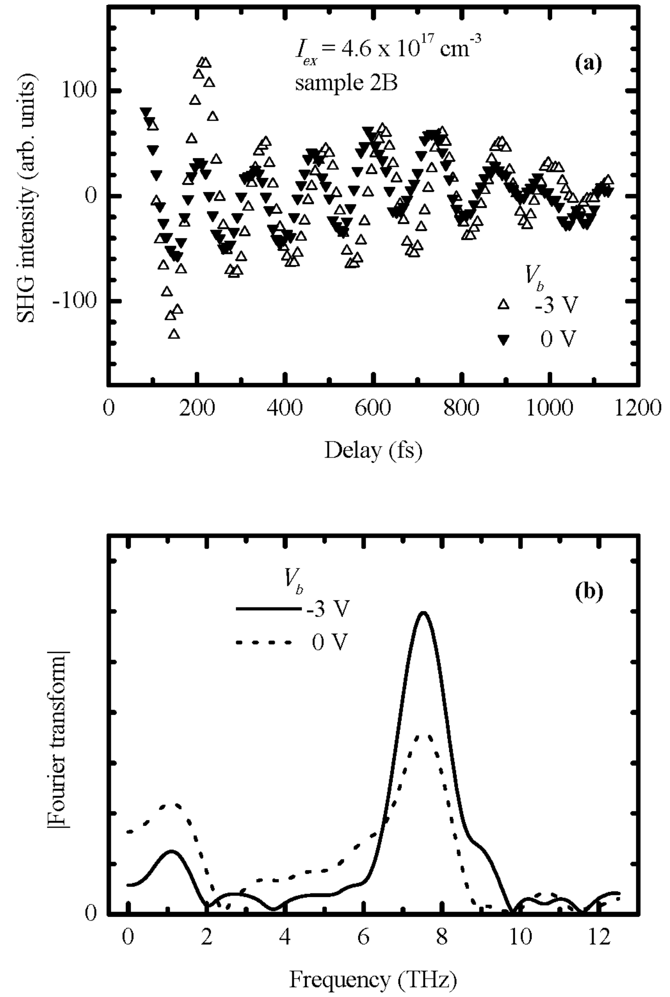

Figure 6.8: (a) Experimental data (from sample 2B) after subtraction of a single exponential, for two different values of the applied bias. The excitation intensity is identical. (b) DFT results for both curves of figure (a).

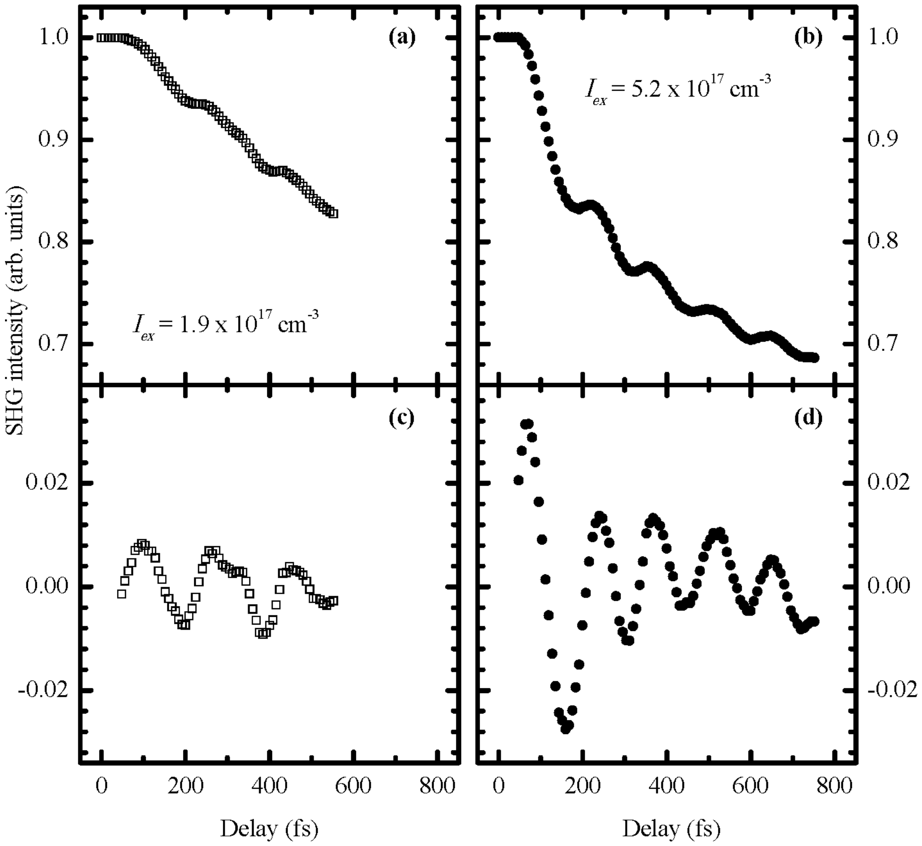

Figure 6.9: The upper panels show the time resolved SHG intensity for two different values of the excitation intensity. The applied bias is -3 V. The rotation of the sample is 135°. The pump beam is S-polarized. The lower panels show the same experimental results after subtraction of a single exponential.

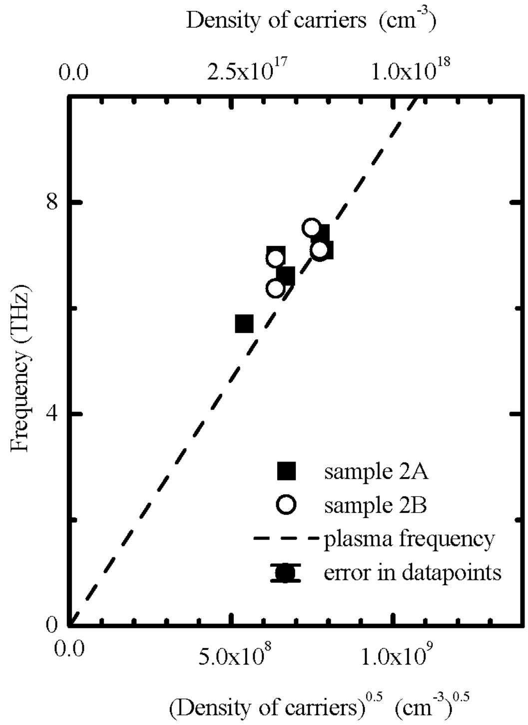

Figure 6.10: DFT results from the experimental curves for different values of the excitation intensity versus the square root of the excited density of carriers. The dashed line is the frequency dependence on density of carriers for a pure plasma as given by equation 6.5. The size of the markers is equal to the error bars in the data points.

6.3 Monte Carlo simulations

To analyse and interpret the results of the previous section quantitatively, Monte Carlo simulations have been performed. The ingredients of these simulations have been described in section 3.3 and are shortly repeated throughout this chapter.

Due to the large number of created carriers the electric field inside the GaAs region collapses within one pico second. It then will take some time before the charge on the Au contact rearranges itself to restore the equipotential plane [16]. From the recovery of the SHG signal at low excitation densities as described in chapter 5, we deduced a value of 25 ps for this restoring time, which has been used for all the calculations presented in this section. The effect of this restoring time is a temporary decoupling of the photo excited electron-hole plasma from the outside world. Since we are interested in the first two ps only, its precise value is highly irrelevant provided it is long enough to achieve this decoupling. The electric field is calculated every 1 fs as a function of the position in the depletion layer and of the time after excitation. Figure 6.11 shows typical results of these calculations. This figure, calculated for a density of carriers of $6.4 \times 10^{17}\text{cm}^{-3}$, clearly shows that the field starts oscillating after 200 fs, when the field has collapsed. At the Au-GaAs interface (at 0 nm in the figure) the field is more or less pinned due to the large amount of holes which is collected at the interface during the recovery time of about 25 ps. Starting at several tens of nanometers from the interface the field is oscillating and changes from positive to negative values.

To compare the simulation results with the EFISHG experiments a finite probe depth has to be taken into account. Since the absorption length for the SHG light is very small, the escape depth is not more than 17 nm. The calculated field is averaged over this region. The dotted line in figure 6.12(a) gives the result of this averaging over the interface region. The final value of 30 kV/cm at 2.0 ps is due to the pinning of the electric field at the interface as is explained above. Figure 6.12(b) shows the result after subtraction of a single exponential from the dotted curve of figure (a). The solid line in figure (b) is a fit to an exponentially damped sine. This fit shows that the calculated oscillations have only one frequency, as was also observed in the experiments.

The amplitude of the oscillations in the dotted line in figure 6.12(a) however is much larger than the experimentally observed amplitude (see figure 6.9(b) for a comparable density). This difference is caused by the following: in the experiment the oscillations in the electric field are probed with a laser pulse which is not infinitesimally short, but has a finite width of 50 fs. This width can be taken into account by calculating the convolution between the Monte Carlo results and a Gaussian with a width of 50 fs. When the dotted line in figure 6.12(a) is convoluted with a Gaussian pulse of 50 fs the amplitude of the oscillations becomes much smaller. The solid line in figure 6.12(a) gives the results after this convolution. Now the calculated curve looks quite similar to the experimental curve of figure 6.9(b).

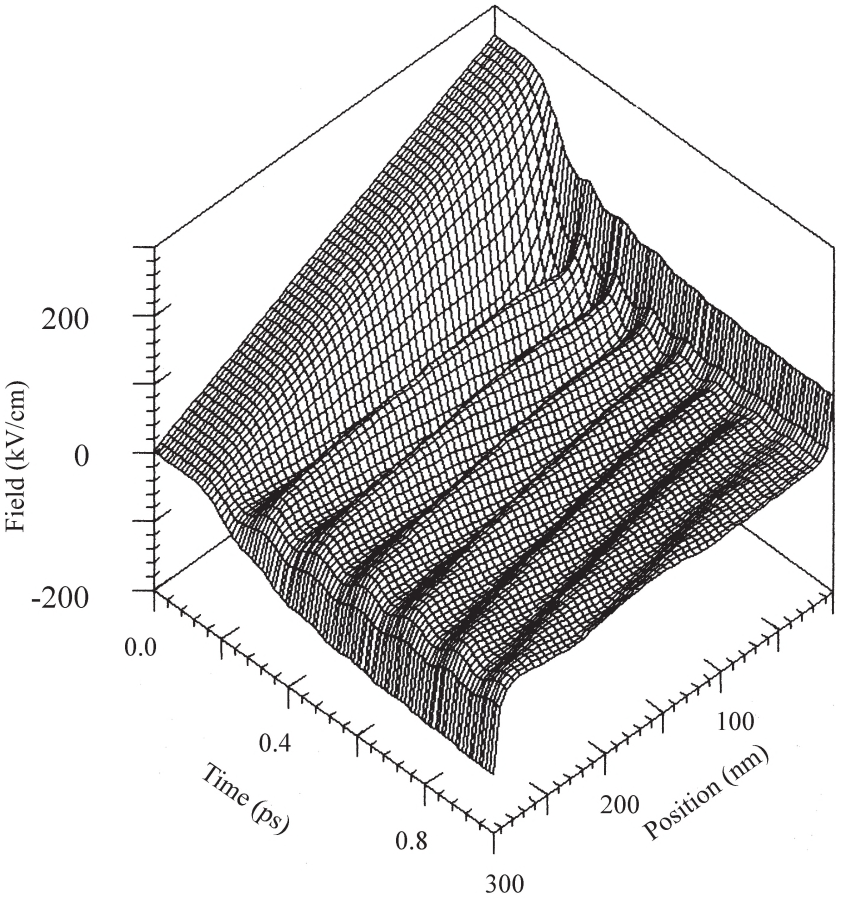

Figure 6.11: Calculated time evolution of the electric field in the depletion region of the Schottky Barrier sample. The Au-GaAs interface is at the position of 0 nm. The center of the excitation pulse is at 0.15 ps.

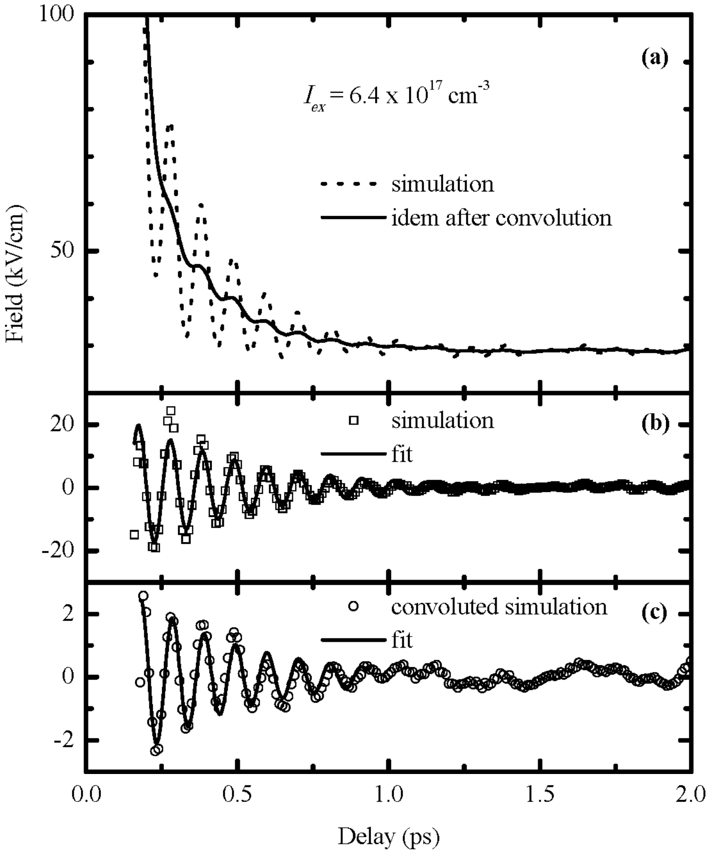

Figure 6.12: (a) The dotted line gives the calculated time evolution of the electric field averaged over the first 15 nanometers of the sample. The solid line is the convolution of the dotted line with a 50 fs Gaussian probe pulse. (b) The squares represent the simulation results of figure (a) after subtraction of a single exponential. The solid line is a single frequency damped sine fit. (c) The dots represent the convoluted simulation results of figure (a), also after subtraction of a single exponential. The solid line is a single frequency damped sine fit.

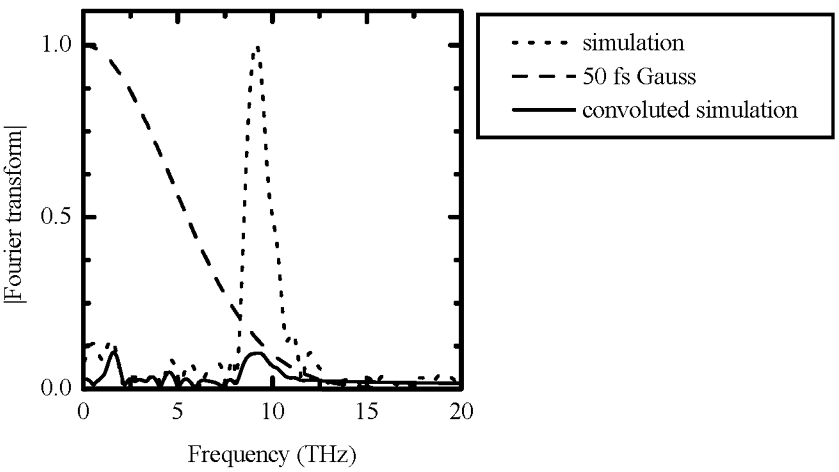

Figure 6.13: Fourier transform of the simulation results as shown in figures 6.12(b)(dotted line) and 6.12(c)(solid line). The dashed line is the DFT of a 50 fs Gaussian. At 5.5 THz its value is 0.5, at 6.9 THz it is 0.33 and at 10 THz it is 0.1.

Convolution in the time domain is similar to multiplication in the frequency domain. Figure 6.13 shows the result of the Fourier transform of both curves of figure 6.12(a) and the discrete Fourier transform (DFT) of a 50 fs Gaussian laser pulse. The DFT of this laser pulse is less than 0.1 for frequencies above 10 THz. Which means that with the used laser pulses it is almost impossible to measure frequencies above 10 THz.

Figure 6.12(c) shows the result after subtraction of an exponential from the convoluted solid curve of figure 6.12(a). Again the solid line is a fit to a damped sine. From figures 6.12(b), 6.12(c) and 6.13 it is clear that the frequency is not changed when the simulation results are convoluted with a Gaussian pulse. Only the amplitude and the phase of the oscillations changes.

6.3.1 Bias and intensity dependence

The simulations have been performed for different values of the carrier density. After subtraction of an exponential, the Fourier transform of all curves has been calculated. Figure 6.14(a) shows the frequencies versus the square root of the density for an applied bias of -3 V. As expected for plasma oscillations the results follow a straight line, which, however, does not intercept the horizontal axis at the origin. This offset is due to the fact that a part of the created carriers does not participate in the plasma oscillation. Their function is to screen the charge on the Au top contact.

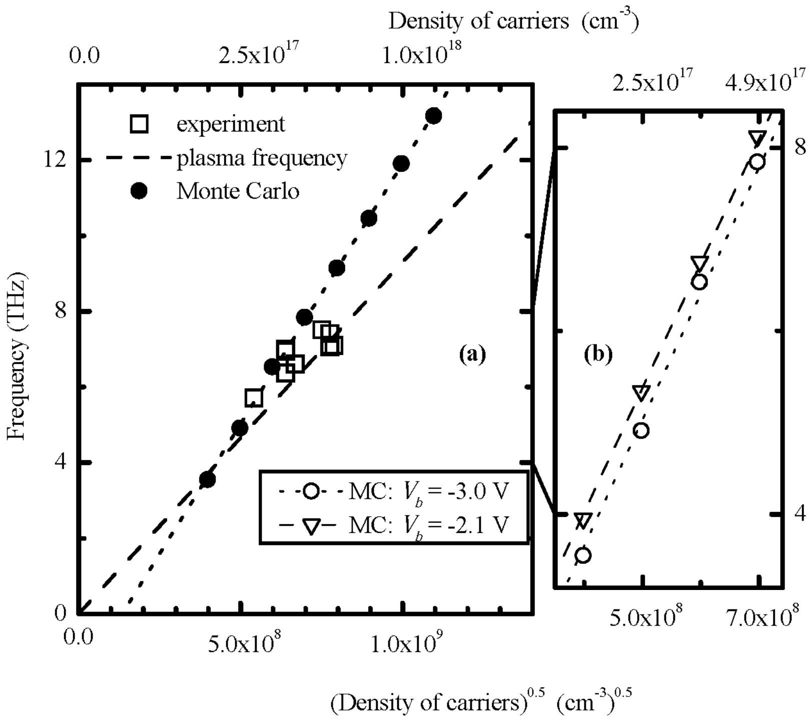

Figure 6.14: Oscillation frequencies versus the square root of the density, obtained by Fourier transforming the simulation results. The circles in the figures (a) and (b) give the frequency values for an applied bias of -3.0 V. The triangles in figure (b) give the frequencies for an applied bias of -2.1 V. The straight lines through the circles and the triangles are linear fits. The dashed line through the origin in figure (a) is the density dependence of a pure plasma oscillation as given by equation 6.5. The squares are the experimental points.

This explanation is corroborated by the displacement of the intercept to lower carrier concentrations with decreasing applied voltage as is shown in figure 6.14(b).

Also, the plasma frequency which is found from the Monte Carlo simulations is higher than the dashed line which gives the predicted frequency from the simple standard equation for plasma oscillations as given by equation 6.5. Again the field is responsible. From the simulations it was found that due to interband scattering about 20–25% of the holes are light holes. Also about 10% of the electrons have been scattered into the higher satellite valleys. These two effects lead to a smaller reduced electron-hole mass with a corresponding higher frequency. This effect is clearly visible in figure 6.11, where in the high field interface region (about 50 nm from the interface) the frequency appears to be higher than far from the interface (about 250 nm), where the field is much lower. The experimentally obtained values for the frequency have also been plotted in figure 6.14(a). This figure shows that for carrier densities below $4 \times 10^{17}\mathrm{cm}^{-3}$ the Monte Carlo simulations fit better to the experimental points. For densities above $5 \times 10^{17}\mathrm{cm}^{-3}$ the line given by equation 6.5 fits better, but both are not perfect.

6.3.2 Plasmon-phonon coupling

The origin of the difference between the simulation results and the experiments is the coupling with the bulk optical phonons. Because optical phonon frequencies[11] are in the same range as the observed plasma frequencies, coupled plasma-phonon oscillations can be expected [10]. Figure 6.15 gives an example of this well known coupling. In this figure the plasma frequency is calculated using the $\omega_p^2 \sim n$ relation of equation 6.5. However this relation is not correct when a very inhomogeneous electric field drives the oscillations, as is clear from figure 6.15. This figure clearly shows that the coupled modes which are calculated in this way give a worse description of the experiments than the uncoupled plasma oscillations.

To obtain the plasmon-phonon coupling in the simulations the procedure of Scholz and Stahl [17] is followed. This procedure of calculating the plasmon-phonon coupling differs fundamentally from the textbook situation shown in figure 6.15 since in our case the plasma frequency is calculated locally in the whole depletion region[12]. Figure 6.16 gives an example of the simulation with the plasmon phonon coupling included. In comparison with figure 6.11 the oscillations of figure 6.16 look quite irregular. In both calculations the same density of carriers has been used. In figure 6.17 the result after averaging over the interface region is given. The dotted line in figure (a) gives the result before convolution with the 50 fs Gaussian pulse. The solid line is the result after convolution. The open symbols in figures (b) and (d) show the oscillations after subtraction of a single exponential from the unconvoluted and convoluted simulation results respectively. Figure (b) shows that with the plasmon-phonon coupling included the oscillation now consists of more than one frequency. Figure (c) shows for

---

[11] 8.046 THz for the bulk TO and 8.745 THz for the bulk LO phonon in GaAs.

[12] See section 3.3 for a description of this procedure.

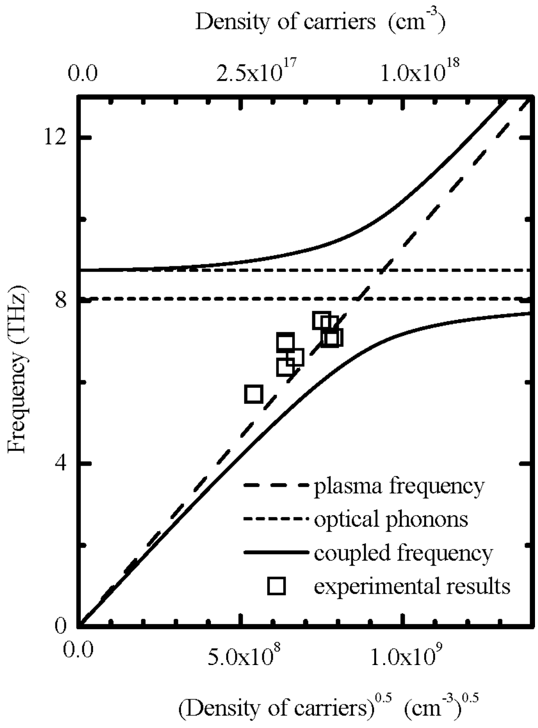

Figure 6.15: Plasmon phonon coupling, using equation 6.5 for the plasma frequency, after [10].

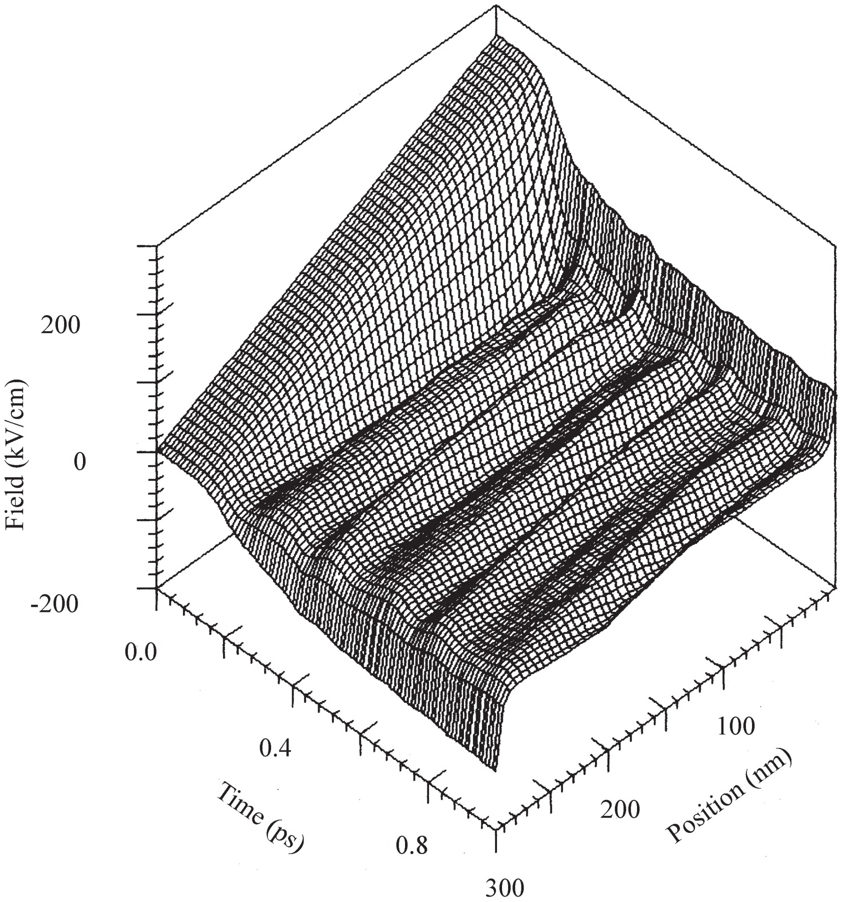

Figure 6.16: Calculated time evolution of the electric field in the depletion region of the Schottky Barrier sample, with plasmon-phonon coupling included. The Au-GaAs interface is at the position of 0 nm. The excitation is at 0.15 ps.

comparison again the uncoupled case of figure 6.12, which clearly has only one frequency. The solid line in figure (b) is a fit to two damped sines, with two frequencies and two damping constants. One frequency corresponds to the upper branch and the other to the lower branch of the plasmon-phonon coupling. An example of these two branches is given in figure 6.15.

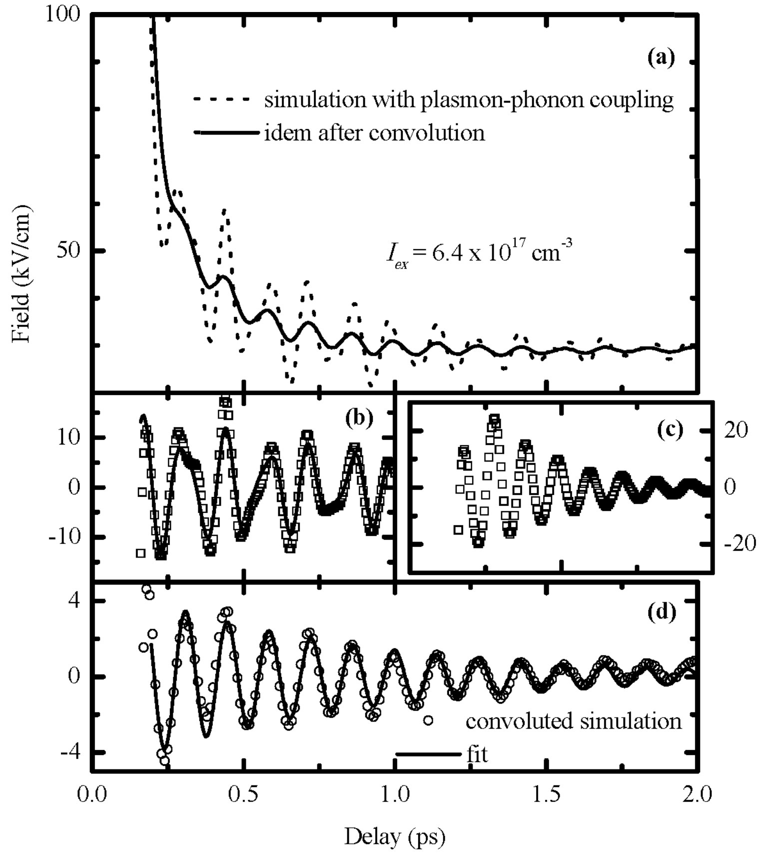

Figure 6.17: (a) The dotted line gives the calculated time evolution of the electric field, averaged over the first 15 nanometers of the sample. In this calculation the plasmon-phonon coupling is included. The solid line is the convolution of the dotted line with a 50 fs Gaussian probe pulse. (b) The squares represent the simulation results of figure (a) after subtraction of a single exponential. The solid line is a damped sine fit with two frequencies. (c) Shows for comparison the results without coupling (see figure 6.12). (d) The dots represent the convoluted simulation results of figure (a), also after subtraction of a single exponential. The solid line is a single frequency damped sine fit.

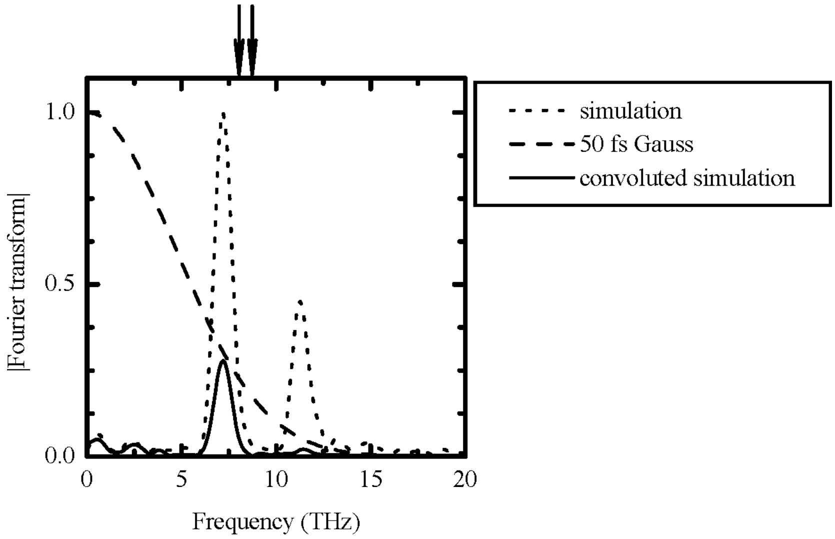

Figure 6.18: DFT results of the simulation results shown in figures 6.17(b) (dotted line) and 6.17(d) (solid line). The dashed line is the DFT of the 50 fs Gaussian probe pulse. The two arrows represent the position of the optical phonons.

The Fourier transform of the results of figure 6.17(b) which is shown by the dotted line in figure 6.18 also shows two peaks, one below and one above the optical phonon frequencies. The solid line in figure 6.18 is the Fourier transform after convolution with a 50 fs Gauss. Now the second peak at 11 THz is almost disappeared and is thus not observable in the experiments. As a result only one frequency remains in figure 6.17(d), which shows the oscillations after convolution. Due to the coupling the remaining peak below the phonon frequencies is at a lower frequency than the uncoupled one in figure 6.13.

If we compare figures 6.12(c) and 6.17(d) or 6.17(b) and 6.17(c) we also can conclude that due to the coupling with the lattice modes, the effective plasmon damping has become significantly less.

Figure 6.19(a) shows the frequencies obtained from the Fourier transformation of a series of simulations at different excitation densities. The two branches which result from the coupling between the optical phonons and the plasmons are clearly visible. It is clear that with our experimental time resolution of 50 fs we only could observe the lower branch. The agreement between experiment and theory is excellent. It has to be emphasized that this result has been obtained without any fitting parameter. The only free parameter, the LO phonon lifetime has a value which does not really influence the results, as it is quite long (4 ps) compared to the period of the combined

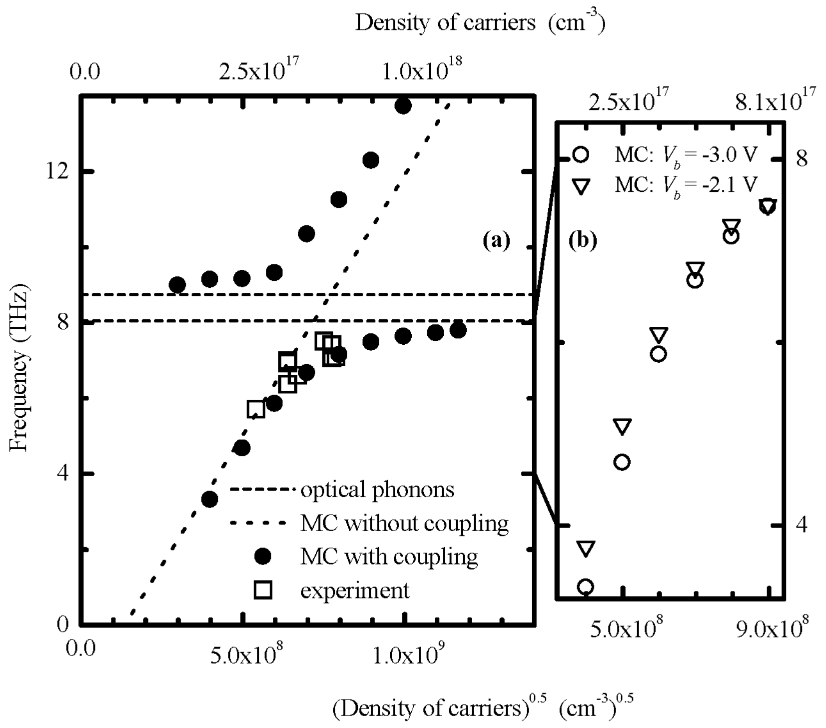

Figure 6.19: (a) Oscillation frequencies versus the square root of the density, obtained by Fourier transforming the simulation results. The dots give the frequency values of the simulation results with plasmon-phonon coupling. The upper and lower branch are clearly visible. The straight dotted line is the result of the simulations without plasmon-phonon coupling (see figure 6.14). The squares are the experimental points. (b) Frequencies for two different values of the applied bias: The circles are the same as in figure (a), with a bias of -3.0 V. For the triangles the bias is -2.1 V.

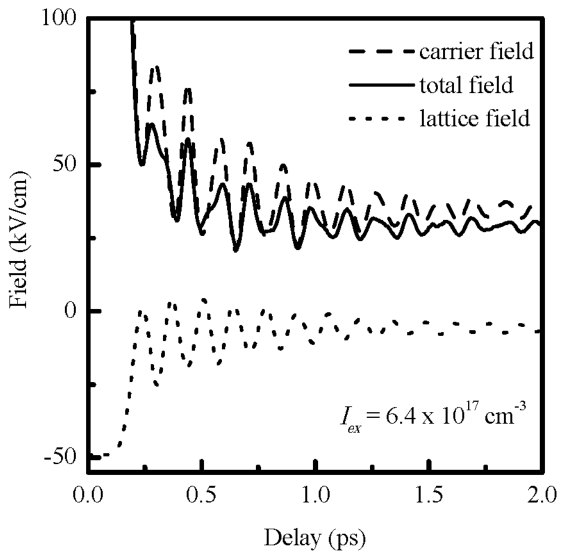

Figure 6.20: The different field components which contribute to the total field in the case of plasmon-phonon coupling. Part of the 'total field' curve is shown in figure 6.17(a).

plasmon-phonon oscillations (< 0.2 ps).

Figure 6.19(b) shows the frequencies with the plasmon-phonon coupling included for two different values of the applied bias. This figure shows that due to the plasmon-phonon coupling the shift, which appeared in figure 6.14(b), disappears in the lower branch at densities above $n = 4 \times 10^{17} cm^{-3}$. At lower densities the shift is of the same order as the experimental uncertainty. In agreement with this result, no difference in frequency was found in the experiments which were shown in figure 6.8.

In order to obtain more insight in the details of the electric field dynamics, we can inspect the various contributions to the driving field E, which has been done in figure 6.20. Here we plot the field due to the space charge as followed from solving the Poisson equation, the field due to the lattice polarization P_L as a solution of the equation of motion 3.4 and the total field. The last one is also plotted in figure 6.17(a). It is obvious that the total field is a combination of the two fields, which in the beginning are out of phase. The lattice polarization clearly cannot follow the sudden collapse of the field at the onset. It strongly counteracts the motion of the free carriers. As a result the space charge field and the lattice field gradually get the same oscillation period which is the eigen frequency of the lattice. It is interesting to see that, though the direct coupling of the field is with the LO phonons, the coupled plasmon-phonon mode converges to the TO frequency, which is in agreement with reference [10].

6.4 Conclusion

Coherent THz plasmon-phonon oscillations have been observed using time resolved SHG measurements. The experimental data has been compared with ensemble Monte Carlo simulations. In these simulations the time dependent electric field throughout the whole depletion region has been calculated in time steps as small as 1 fs. Since this space charge field varies inhomogeneously in space and time, microscopic calculations like the ensemble Monte Carlo simulations are absolutely required. When the finite pulse width in the experiment, and the escape depth of the SHG light are taken into account, the results of the simulations can be compared directly with the experiments and show an excellent agreement, without any adjustable parameter.

The dependence of the oscillations on different parameters has been determined. The oscillations do not depend on the polarization of the pump beam, which is normal for plasma oscillations, and excludes other driving mechanisms [8]. With different wavelengths of the laser beams, even with a carrier excess energy of more than 7 LO phonons, the oscillations have been observed. This result is in agreement with the simulations, since they show that the excess energy does not influence the oscillations very much. The excited carriers are accelerated by the electric field and gain in this way much more energy.

In the simulations a frequency shift is observed when the applied bias is changed. This shift is due to the fact that part of the excited carriers is needed to screen the applied field at the gold GaAs interface, thus leaving a lower density of carriers to oscillate, resulting in a lower frequency. The amount of carriers which is needed for the screening depends on the applied bias. The experimental resolution however is too low to measure this shift. With shorter laser pulses, about 10 fs, and a better signal to noise ratio it may be possible to measure this shift.

The plasmon-phonon coupling in the Monte Carlo simulations has been calculated locally in the whole depletion region, taking into account the (time dependent) amount of carriers scattered to the side valleys. This procedure differs fundamentally from the phenomenological description and gives results which agree better with the experiments. The lower branch of the calculated dispersion agrees very well with the measured dispersion. With shorter laser pulses the upper branch and oscillations at a lower excitation intensity can also be measured.

With this combined experimental and theoretical investigation we have obtained a thorough understanding of all the processes playing an important role. Due to its intrinsic surface sensitivity, femto second EFISHG could become an excellent tool to study interface and surface phonons, as was recently demonstrated for a clean GaAs surface [8].

References

[1] M. Born and E. Wolf. *Principles of Optics.* Pergamon Press, Oxford, 1980.

[2] C. W. van Hasselt *et al.* Oxide-thickness dependence of second harmonic generation from thick thermal oxides on Si(111). *Surf. Sci.*, **331-333**, 1367, (1995).

[3] C. W. van Hasselt, M. A. C. Devillers, Th. Rasing, and O. A. Aktsipetrov. Second-harmonic generation from thick thermal oxides on Si(111): the influence of multiple reflections. *J. Opt. Soc. B*, **12**, 33–36, (1995).

[4] C. W. van Hasselt. *Nonlinear and linear optical studies of Si-SiO$_2$ interfaces.* Ph.D. dissertation, Katholieke Universiteit Nijmegen, Nijmegen, 1997.

[5] S. Adachi. GaAs, AlAs, and Al$_x$Ga$_{1-x}$As: Material parameters for use in research and device applications. *J. Appl. Phys.*, **58**, R1–R29, (1985).

[6] A. V. Oppenheim, A. W. Willsky, and I. T. Young. *Signals and Systems.* Prentice-Hall Signal Processing Series. Prentice-Hall International, London, 1983.

[7] W. H. Press, B. P. Flannery, S. A. Teukolsky, and W. T. Vetterling. *Numerical Recipes, The Art of Scientific Computing.* Cambridge University Press, Cambridge, 1986.

[8] Y. M. Chang, L. Xu, and H. W. K. Tom. Observation of coherent surface optical phonon oscillations by time-resolved surface second-harmonic generation. *Phys. Rev. Lett.*, **78**, 4649–4652, (1997).

[9] W. Fischler, P. Buchberger, R. A. Höpfel, and G. Zandler. Ultrafast reflectivity changes in photoexcited GaAs Schottky diodes. *Appl. Phys. Lett.*, **68**, 2778–2780, (1996).

[10] A. Mooradian and A. L. McWhorter. Polarization and intensity of Raman scattering from plasmons and phonons in gallium arsenide. *Phys. Rev. Lett.*, **19**, 849–852, (1967).

[11] W. Sha, A. L. Smirl, and W. F. Tseng. Coherent plasma oscillations in bulk semiconductors. *Phys. Rev. Lett.*, **74**, 4273–4276, (1995).

[12] Y.-X. Yan, E. B. Gamble, and K. A. Nelson. Impulsive stimulated scattering: General importance in femtosecond laser pulse interactions with matter, and spectroscopic applications. *J. Chem. Phys.*, **83**, 5391–5399, (1985).

[13] D. Menzel and R. Gomer. Desorption from metal surfaces by low-energy electrons. *J. Chem. Phys.*, **41**, 3311–3328, (1964).

[14] P. A. Redhead. Interaction of slow electrons with chemisorbed oxygen. *Can. J. Phys.*, **42**, 886–905, (1964).

[15] O. Madelung. *Introduction to Solid-State Theory*, volume 2 of *Springer Series in Solid-State Sciences.* Springer-Verlag, Berlin, 1981.

[16] P. C. M. Christianen *et al.* Ultrafast carrier dynamics at a metal-semiconductor interface. *J. Appl. Phys.*, **80**, 6831–6838, (1996).

[17] R. Scholz and A. Stahl. Generation of LO-phonons in a time-dependent electric field at the surface of III-V materials. *Phys. Stat. Sol. B*, **168**, 123–138, (1991).

Appendix A

Electric field induced second harmonic generation

In this appendix the tensor elements are derived which play a role in electric field induced second harmonic generation from GaAs(100) surfaces and interfaces. GaAs belongs to the $\bar{4}3$m symmetry class. The crystal structure is shown in figure A.1(a). The coordinate system in this figure is natural to $\bar{4}3$m symmetry where, by convention the Ga-As bonds point in the [111],$[\bar{1}\bar{1}1]$,$[\bar{1}1\bar{1}]$ and $[1\bar{1}\bar{1}]$ directions.

In $\bar{4}3$m, six of the 27 bulk elements χ_{ijk} of $\overset{\leftrightarrow}{\chi}^{(2)}$, are nonzero. All are equivalent by symmetry and have the following combinations of indices i, j and k [1–5]:

$$\chi^{(2)}_{xyz} = \chi^{(2)}_{xzy} = \chi^{(2)}_{yxz} = \chi^{(2)}_{yzx} = \chi^{(2)}_{zxy} = \chi^{(2)}_{zyx} \tag{A.1}$$

Figure A.1(b) shows the (001) face of GaAs. The atomic positions of the Ga and the As are projected on a cube face; fractions denote the distance below the surface in units of a cube edge. This face has mm2 symmetry, $\hat{x}'$ and $\hat{y}'$ in the figure are the basis vectors usually associated with the mm2 group [1]. The basis vectors $\hat{x}$ and $\hat{y}$ which are also shown in the figure are identical to the basis vectors of the $\bar{4}3$m system. In its own coordinate system, mm2 symmetry gives 7 independent tensor elements of the interface susceptibility tensor $\overset{\leftrightarrow}{\Delta}^{(2)}$ [1]:

$$\Delta^{(2)}_{x'x'z}, \Delta^{(2)}_{x'zx'}, \Delta^{(2)}_{y'y'z}, \Delta^{(2)}_{y'zy'}, \Delta^{(2)}_{zx'x'}, \Delta^{(2)}_{zy'y'}, \Delta^{(2)}_{zzz} \tag{A.2}$$

When the $\hat{x}'$, $\hat{y}'$ coordinate system of mm2 is transformed to the $\hat{x}$, $\hat{y}$ system of $\bar{4}3$m, the tensor elements of $\overset{\leftrightarrow}{\Delta}^{(2)}$ transform to:

$$\begin{gathered}\Delta^{(2)}_{xyz} = \Delta^{(2)}_{yxz}, \Delta^{(2)}_{xzy} = \Delta^{(2)}_{yzx}, \Delta^{(2)}_{zxy} = \Delta^{(2)}_{zyx}, \\ \Delta^{(2)}_{xxz} = \Delta^{(2)}_{yyz}, \Delta^{(2)}_{xzx} = \Delta^{(2)}_{yzy}, \Delta^{(2)}_{zxx} = \Delta^{(2)}_{zyy}, \Delta^{(2)}_{zzz}\end{gathered} \tag{A.3}$$

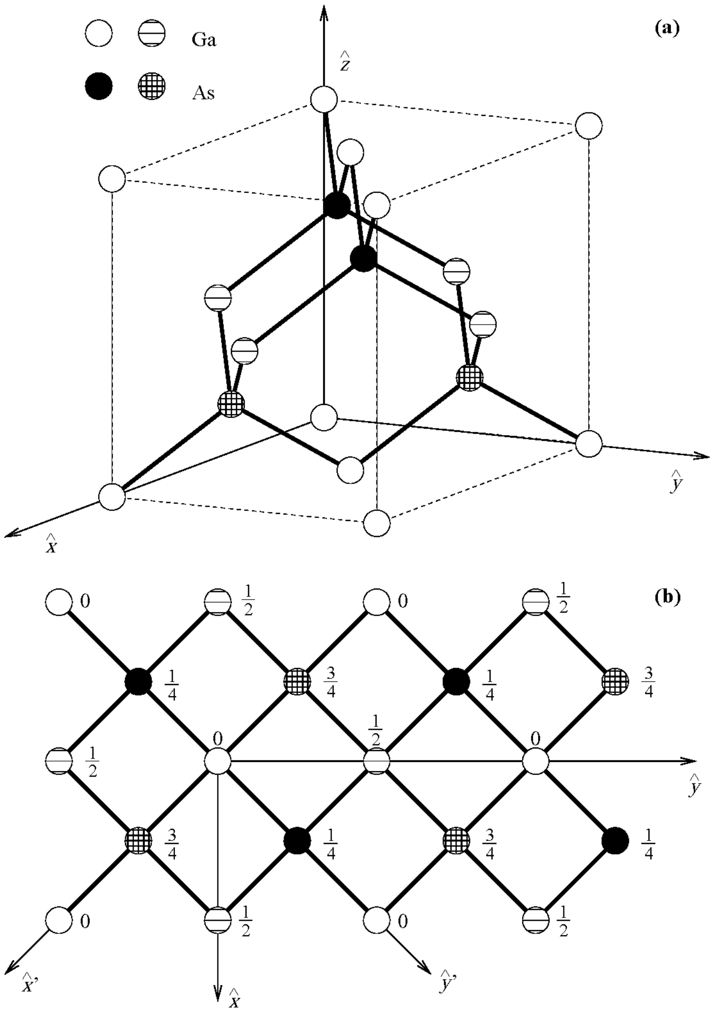

Figure A.1: (a) Crystal structure of GaAs with the $\hat{x}$, $\hat{y}$ coordinate system natural to the $\bar{4}3$m symmetry class. (b) The (001) plane which also shows the $\hat{x}'$, $\hat{y}'$ coordinate system associated with the mm2 symmetry. The fractions denote the distance below the surface in units of a cube edge.

Now we have 13 nonzero elements, with still 7 of them independent. The first six elements are equal to the bulk $\bar{4}3$m elements from equation A.1, but due to the symmetry lowering at the interface these six elements are no longer identical. Due to the symmetry reduction also 7 new elements appear.

In second harmonic generation the second and third index of all tensor elements can be interchanged since the generating fields are identical, which reduces the number of independent elements of $\overset{\leftrightarrow}{\Delta}^{(2)}$ to 5:

$$\begin{gathered}\Delta^{(2)}_{xyz} = \Delta^{(2)}_{yxz} = \Delta^{(2)}_{xzy} = \Delta^{(2)}_{yzx}, \Delta^{(2)}_{zxy} = \Delta^{(2)}_{zyx}, \\ \Delta^{(2)}_{xxz} = \Delta^{(2)}_{yyz} = \Delta^{(2)}_{xzx} = \Delta^{(2)}_{yzy}, \Delta^{(2)}_{zxx} = \Delta^{(2)}_{zyy}, \Delta^{(2)}_{zzz}\end{gathered} \tag{A.4}$$

A.1 Electric field induced second harmonic generation

For electric field induced second harmonic generation (EFISHG) not only optical electric fields at the frequency ω play a role, but also quasi static electric fields at zero frequency or a frequency much lower than the optical frequency. Now the induced polarization at the second harmonic frequency can be written as an expansion of the static electric field $\mathbf{E}(0)$ as [2]:

$$\mathbf{P}(2\omega) = \overset{\leftrightarrow}{\chi}^{(2)} : \mathbf{E}(\omega)\mathbf{E}(\omega) + \overset{\leftrightarrow}{\chi}^{(3)} \vdots \mathbf{E}(\omega)\mathbf{E}(\omega)\mathbf{E}(0) + \overset{\leftrightarrow}{\chi}^{(4)} \mathbin{\substack{\cdot\\ \cdot\\ \cdot\\ \cdot}} \mathbf{E}(\omega)\mathbf{E}(\omega)\mathbf{E}(0)\mathbf{E}(0) + .. \tag{A.5}$$

Where $\overset{\leftrightarrow}{\chi}^{(3)}$ and $\overset{\leftrightarrow}{\chi}^{(4)}$ have symmetry properties of the $\bar{4}3$m bulk crystal. There are 22 non-zero bulk elements of $\overset{\leftrightarrow}{\chi}^{(3)}$, four of which are unique: [1]

$$\chi^{(3)}_{iijj}, \chi^{(3)}_{ijij}, \chi^{(3)}_{ijji}, \chi^{(3)}_{iiii}, (i \neq j) \tag{A.6}$$

When contracted with a static electric field $\mathbf{E}(0)$ which only has a z-component E_z and interchanging the second and third index, these elements give rise to three unique non-zero bulk elements of $\chi^{(3)}_{ijkz}E_z$, in a shorthand notation denoted by $\chi^{(2)*}_{ijk}$:

$$\chi^{(2)*}_{xxz} = \chi^{(2)*}_{yyz} = \chi^{(2)*}_{xzx} = \chi^{(2)*}_{yzy}, \chi^{(2)*}_{zxx} = \chi^{(2)*}_{zyy}, \chi^{(2)*}_{zzz} \tag{A.7}$$

Similarly, there are two independent bulk elements of $\chi^{(4)}_{ijkzz}E^2_z$, in a shorthand notation denoted by $\chi^{(2)**}_{ijk}$:

$$\chi^{(2)**}_{xyz} = \chi^{(2)**}_{xzy} = \chi^{(2)**}_{yxz} = \chi^{(2)**}_{yzx}, \chi^{(2)**}_{zxy} = \chi^{(2)**}_{zyx} \tag{A.8}$$

The mm2 interface of the crystal can also contribute to this process. After transformation to the $\hat{x}$, $\hat{y}$ coordinate system, $\Delta^{(3)}_{ijkz}E_z$ (=$\Delta^{(2)*}_{ijk}$) and $\Delta^{(4)}_{ijkzz}E^2_z$ (=$\Delta^{(2)**}_{ijk}$) have the following interface elements [1]:

$$\begin{aligned} \Delta^{(2)*}_{xyz} = \Delta^{(2)*}_{yxz} = \Delta^{(2)*}_{xzy} = \Delta^{(2)*}_{yzx}, \Delta^{(2)*}_{zxy} = \Delta^{(2)*}_{zyx}, \\ \Delta^{(2)*}_{xxz} = \Delta^{(2)*}_{yyz} = \Delta^{(2)*}_{xzx} = \Delta^{(2)*}_{yzy}, \Delta^{(2)*}_{zxx} = \Delta^{(2)*}_{zyy}, \Delta^{(2)*}_{zzz} \end{aligned} \tag{A.9}$$

$$\begin{aligned} \Delta^{(2)**}_{xyz} = \Delta^{(2)**}_{yxz} = \Delta^{(2)**}_{xzy} = \Delta^{(2)**}_{yzx}, \Delta^{(2)**}_{zxy} = \Delta^{(2)**}_{zyx}, \\ \Delta^{(2)**}_{xxz} = \Delta^{(2)**}_{yyz} = \Delta^{(2)**}_{xzx} = \Delta^{(2)**}_{yzy}, \Delta^{(2)**}_{zxx} = \Delta^{(2)**}_{zyy}, \Delta^{(2)**}_{zzz} \end{aligned} \tag{A.10}$$

Comparison with equation A.4 shows that the same elements are nonzero as for the normal SHG from an mm2 interface.

Taking equations A.1, A.4, A.7, A.8, A.9 and A.10 together, the effective susceptibility elements become:

$$\begin{aligned} \chi^{(eff)}_{xxz} = \chi^{(eff)}_{xzx} = \chi^{(eff)}_{yyz} = \chi^{(eff)}_{yzy} &= \Delta^{(2)\dagger}_{xxz} + \chi^{(3)}_{xxzz}E_z \\ \chi^{(eff)}_{zxx} = \chi^{(eff)}_{zyy} &= \Delta^{(2)\dagger}_{zxx} + \chi^{(3)}_{zxxz}E_z \\ \chi^{(eff)}_{zzz} &= \Delta^{(2)\dagger}_{zzz} + \chi^{(3)}_{zzzz}E_z \\ \chi^{(eff)}_{xyz} = \chi^{(eff)}_{xzy} = \chi^{(eff)}_{yxz} = \chi^{(eff)}_{yzx} &= \Delta^{(2)\dagger}_{xyz} + \chi^{(2)}_{xyz} + \chi^{(4)}_{xyzzz}E_zE_z \\ \chi^{(eff)}_{zxy} = \chi^{(eff)}_{zyx} &= \Delta^{(2)\dagger}_{zxy} + \chi^{(2)}_{zxy} + \chi^{(4)}_{zxyzz}E_zE_z \end{aligned} \tag{A.11}$$

with:

$$\Delta^{(2)\dagger}_{ijk} = \Delta^{(2)}_{ijk} + \Delta^{(3)}_{ijkz}E_z + \Delta^{(4)}_{ijkzz}E_zE_z \tag{A.12}$$

These equations show that for the bulk elements the linear electric field dependence and the quadratic electric field dependence appear in different tensor elements, while for the interface elements the linear and quadratic dependence appear in the same elements.

A.2 Radiated fields

The total field radiated by the nonlinear polarization $\mathbf{P}(2\omega)$ will depend on the orientation of the crystal, the polarization state of the incoming radiation, the angle of incidence, and the dielectric properties of the crystal. The derivation of the radiated field follows the discussions of references [6–8]. For linearly polarized input fields incident on a GaAs(001) surface, it can be shown that the radiated second harmonic fields $E_{in,out}$[1] are given in terms of the input electric fields E_p and E_s measured outside the

---

[1] '*in*' is the polarization state of the incoming light and '*out*' the polarization state of the generated light at the second harmonic frequency. For both only 'P' and 'S' polarization has been measured in the experiments.

material by [8]:

$$\begin{aligned}
E_{pp} &= E_p^2 t_p^2 \{-f_s^2 F_s (B_p^{(3)} \chi^{(3)}_{zzzz} + K_p \Delta_{zzz}) + 2 f_c f_s F_c (B_p^{(3)} \chi^{(3)}_{xxzz} + K_p \Delta_{xxz}) \\
&\quad - f_c^2 F_s (B_p^{(3)} \chi^{(3)}_{zxxz} + K_p \Delta_{zxx}) && \text{(A.13)} \\
&\quad + [2 f_c f_s F_c (B_p^{(2)} \chi^{(2)}_{xyz} + B_p^{(4)} \chi^{(4)}_{xyzzz} + K_p \Delta_{xyz}) \\
&\quad - f_c^2 F_s (B_p^{(2)} \chi^{(2)}_{xyz} + B_p^{(4)} \chi^{(4)}_{zxyzz} + K_p \Delta_{zxy})] \sin 2\psi \} \\
E_{ps} &= 2 E_p^2 f_c f_s t_p^2 (B_s^{(2)} \chi^{(2)}_{xyz} + B_s^{(4)} \chi^{(4)}_{xyzzz} + K_s \Delta_{xyz}) \cos 2\psi && \text{(A.14)} \\
E_{sp} &= -E_s^2 F_s t_s^2 [B_p^{(3)} \chi^{(3)}_{zxxz} + K_p \Delta_{zxx} \\
&\quad - (B_p^{(2)} \chi^{(2)}_{xyz} + B_p^{(4)} \chi^{(4)}_{zxyzz} + K_p \Delta_{zxy}) \sin 2\psi] && \text{(A.15)} \\
E_{ss} &= 0 && \text{(A.16)}
\end{aligned}$$

with:

$$K_{p,s} \Delta_{ijk} = K_{p,s} \left(\Delta^{(2)}_{ijk} + \Delta^{(3)}_{ijkz} E_z(z=0) + \Delta^{(4)}_{ijkzz} E_z^2(z=0) \right) \tag{A.17}$$

where ψ is the rotation of [100] direction out of the plane of incidence, $B^{(2)}_{p,s}$ is given by [8]:

$$B^{(2)}_{p,s} = -\frac{i\Omega^2 T_{p,s}}{2W} \int_0^\infty e^{-i\rho z} dz = \frac{\Omega^2 T_{p,s}}{2\rho W} \tag{A.18}$$

and the phase parameter $\rho = 2w + W$. For GaAs and a fundamental wavelength around 800 nm, ρ is of the order of (10 nm)$^{-1}$. The terms for $B^{(3)}_{p,s}$ and $B^{(4)}_{p,s}$ can be similarly derived to be [8]

$$B^{(3)}_{p,s} = -\frac{3i\Omega^2 T_{p,s}}{2W} \int_0^\infty E_z(z)\; e^{-i\rho z} dz \tag{A.19}$$

and

$$B^{(4)}_{p,s} = -\frac{3i\Omega^2 T_{p,s}}{W} \int_0^\infty E_z^2(z)\; e^{-i\rho z} dz \tag{A.20}$$

$$K_{p,s} = \frac{\Omega T_{p,s}}{2W} \tag{A.21}$$

The interface elements $\Delta^{(2)}_{ijk}$, $\Delta^{(3)}_{ijkz}$ and $\Delta^{(4)}_{ijkzz}$ are already integrated over the interface region (see reference [9] and references therein). The terms f_c, f_s, F_c and F_s are the complex cosine and sine of the fundamental and second harmonic internal angles, $\Omega = 2\omega/c$, w and W are the components of the wavevectors of the fundamental and second harmonic light in the direction perpendicular to the surface, and t_s (t_p) and T_s (T_p) are the transmission coefficients of the fundamental light into and the second harmonic light out of the crystal for s (p) polarized light respectively. Explicit expressions for these parameters are:

$$f_s = \frac{n_0}{n_S} \sin\theta \tag{A.22}$$

and

$$f_c = \sqrt{1 - {f_s}^2} \tag{A.23}$$

Here θ is the incident angle with respect to the surface normal, n_0 and n_S are the complex index of the incident media and the substrate at the fundamental wavelength. The transmission coefficients for s- and p-polarized light are given by [8]

$$t_s = \frac{2w_0}{w_0 + w} \tag{A.24}$$

and

$$t_p = \frac{2n_0 n w_0}{w_0 n_S^2 + w n_0^2} \tag{A.25}$$

where

$$w = \frac{\omega}{c}\sqrt{n_S^2 - n_0^2 \sin^2\theta} \tag{A.26}$$

and

$$w_0 = \frac{\omega n_0}{c}\sqrt{1 - \sin^2\theta} \tag{A.27}$$

Expressions for F_c, F_s, T_s, T_p, W and W_0 are readily derived from the above with the replacements $\omega \to 2\omega$, $n_S \to N_S$ and $n_0 \to N_0$. In the expressions for T_s and T_p, $w_0 \to W$ and $w \to W_0$, as the T's are the transmission factors for the excited harmonic.

A.3 Integration of the static electric field

The electric field in the depletion region, $0 < z < L_d$, of a Schottky barrier sample is given by equation 3.2. The depletion width L_d, as given by equation 3.1, is of the order 200 nm, which is much larger than $1/\rho$.

Inserting equations 3.2 and 3.1 into equations A.19 and A.20 and integrating, one obtains:

$$B^{(3)}_{p,s} = -\frac{3i\Omega^2 T_{p,s}}{2W\rho}\left(\frac{1 - e^{(i\rho L'_d E_z(z=0))}}{\rho L'_d} + iE_z(z=0)\right) \tag{A.28}$$

and

$$B^{(4)}_{p,s} = -\frac{3i\Omega^2 T_{p,s}}{W\rho}\left(\frac{2ie^{i\rho L'_d E_z(z=0))} - 2i}{(\rho L'_d)^2} + \frac{2E_z(z=0)}{\rho L'_d} + iE_z^2(z=0)\right) \tag{A.29}$$

References

[1] R. R. Birss. *Symmetry and Magnetism*, volume 3 of *Selected topics in solid state physics*. North-Holland, Amsterdam, 1964.

[2] Y. R. Shen. *The principles of nonlinear optics*. John Wiley and Sons, New York, 1984.

[3] T. Stehlin, M. Feller, P. Guyot-Sionnest, and Y. R. Shen. Optical second harmonic generation as a surface probe for non-centrosymmetric media. *Optics Lett.*, **13**, 389–391, (1988).

[4] R. W. J. Hollering. Bulk and surface second-harmonic generation in noncentrosymmetric semiconductors. *Opt. Comm.*, **90**, 147–150, (1992).

[5] J. Qi *et al.* Depletion-electric-field-induced changes in second-harmonic generation from GaAs. *Phys. Rev. Lett.*, **71**, 633–636, (1993).

[6] J. E. Sipe, D. J. Moss, and H. M. van Driel. Phenomenological theory of optical second- and third-harmonic generation from cubic centrosymmetric crystals. *Phys. Rev. B*, **35**, 1129–1141, (1987).

[7] J. E. Sipe. New green-function formalism for surface optics. *J. Opt. Soc. B*, **4**, 481–489, (1987).

[8] T. A. Germer, K. W. Kolasiński, J. C. Stephenson, and L. J. Richter. Depletion-electric-field-induced second-harmonic generation near oxidized GaAs(001) surfaces. *Phys. Rev. B*, **55**, 10694–10706, (1997).

[9] A. V. Petukhov. Sum-frequency generation on isotropic surfaces: General phenomenology and microscopic theory for jellium surfaces. *Phys. Rev. B*, **52**, 16901–16911, (1995).

Summary

This thesis describes time resolved second harmonic generation (SHG) experiments on a metal semiconductor interface, namely a Schottky barrier, and the interpretation of these experiments via Monte Carlo simulations. The Schottky barrier is formed by a thin layer of gold that is evaporated on n-type GaAs. In the GaAs layer near the interface charge carriers are excited by ultrashort laser pulses. The intensity of the time dependent second harmonic signal can be used to measure the time dependent electric field at the interface.

Chapter 2 describes the experimental setup, the techniques and the samples that have been used for the experiments.

The first section of chapter 3 describes the properties of the electric field at a Schottky barrier interface. The second section gives some parameters of the band structure of GaAs and further, it refers to the different scattering mechanisms for charge carriers in GaAs. In the third section the Monte Carlo simulation technique is shortly introduced. Subsequently the modeling of the Schottky barrier sample, which is used in the experiments, is described in more detail. In this model the following is important. At the Schottky barrier interface an electric field exists. This E-field will grow when the thin metal contact is negatively charged by an external voltage source. After excitation of charge carriers in the GaAs layer by an ultrashort laser pulse, which is focused on a spot of 100 μm diameter, the holes will move to the surface under the influence of the electric field and they will compensate the electric charge on the metal contact partly, or even completely, depending on the density of excited carriers. To recover the potential at the excitation spot, charge carriers have to flow through the metal layer to this place. Since this metal layer has a thickness of only a few nanometers, this transport takes several pico seconds and during this time the place where the carriers have been excited, is in principle decoupled from the external voltage source. In the Monte Carlo simulations this has been introduced as a time constant which determines the time needed to give the E-field its original value after partial or complete collapse. If the number of excited carriers is much larger than the number of electrons on the negative metal contact, an overshoot can occur and this introduces oscillations in the system of positive and negative charge carriers. These are plasma oscillations which have a frequency of about 7 THz. Bulk phonons in GaAs have a frequency which is of the same order of magnitude and a coupling between the plasma oscillations and the phonons will occur. This is well known, but till now it has been described in a

phenomenological way and it has never been incorporated in Monte Carlo simulations. In our simulations this coupling has been incorporated in the equations of motion in a fundamental way.

The fourth section of chapter 3 shortly describes the phenomenon optical second harmonic generation (SHG), and offers a more thorough description of electric field induced SHG. This so called EFISHG is the basis for the direct detection of the time dependence of the electric field at the Schottky barrier interface after excitation of charge carriers.

In chapter 4 anisotropy experiments are described in which only a probe beam and no pump beam has been used. With these experiments the various contributions to the SHG signal can be separated. The applied bias is varied to determine if, and to what extent, the SHG signal depends on the electric field at the Schottky barrier interface. The results of these experiments show that a certain component of the signal is proportional to the electric field at the interface. This component can be measured by choosing the right polarization of laser beams and by choosing the right orientation of the crystal axis of the sample relative to the laser beams.

Chapter 5 describes experiments where a probe and an excitation beam are used with a very accurately controlled time delay between both beams. In these experiments the excitation density has been varied but these densities have been kept relatively low. The spot diameter has also been varied. The results of these experiments have been compared with the results of the simulations to check the concept of the decoupling-time constant and to determine the magnitude of this constant.

Finally chapter 6 presents time resolved experiments where the excitation density is much higher than in chapter 5. The result is the observation of oscillations in the SHG signal, due to plasma oscillations. This is new since the plasma oscillations have been measured directly in the time domain. These oscillations are also compared with the simulations. In the simulations the only adjustable parameter is the recovery time constant which was determined in chapter 5. In chapter 6 this constant has not been varied. The oscillations in the electric field which are calculated by the simulations perfectly agree with the measured oscillations in the SHG signal. By means of Fourier analyses the frequency of measured and calculated oscillations has been determined as a function of the excitation density. If the plasmon phonon coupling is incorporated in the simulations, the experiment and the simulations agree perfectly well with each other.

In conclusion, time resolved SHG is a useful technique to measure the time dependent electric field at a metal semiconductor interface. Also the model used in the Monte Carlo simulations describes the system very well.

Samenvatting

Dit proefschrift beschrijft tijdsopgeloste tweede harmonische generatie (SHG) metingen aan een metaal halfgeleider grensvlak, namelijk een Schottky barrière, en de interpretatie daarvan door middel van Monte Carlo simulaties. De Schottky barrière wordt gevormd door een dunne goudlaag die op n-type gallium arseen (GaAs) is aangebracht. In de GaAs-laag achter het grensvlak worden ladingsdragers geëxciteerd met behulp van een ultrakorte laserpuls. De intensiteit van het tijdsafhankelijke tweede harmonische signaal is een maat voor het tijdsafhankelijke elektrische veld aan het grensvlak.

Hoofdstuk 2 beschrijft de experimentele opstelling, de technieken en de preparaten die gebruikt zijn in de experimenten.

Hoofdstuk 3 beschrijft in de eerste sectie de eigenschappen van het elektrische veld aan een Schottky barrière grensvlak. De tweede sectie geeft enkele parameters van de bandenstructuur van GaAs en verder verwijzingen naar de verschillende verstrooiingsmechanismen voor ladingsdragers in GaAs. In de derde sectie wordt de Monte Carlo simulatie techniek kort ingeleid, waarna meer uitvoerig wordt ingegaan op de modellering van het in dit proefschrift beschreven Schottky barrière preparaat. Hierbij is het volgende van belang.

Aan het Schottky barrière grensvlak staat een elektrisch veld. Dit E-veld wordt groter als met een externe spanningsbron negatieve lading op de dunne goudlaag wordt gebracht. Na excitatie van ladingsdragers in het GaAs door middel van een ultrakorte laserpuls, die gefocusseerd is op een punt met een diameter van 100 μm, zullen de gaten onder invloed van het elektrische veld naar het grensvlak bewegen en de negatieve lading op het goudcontact gedeeltelijk of geheel compenseren, afhankelijk van de hoeveelheid geëxciteerde ladingsdragers. Om de potentiaal ter plaatse van het excitatie punt te herstellen moet lading aangevoerd worden van elders. Aangezien de goudlaag waardoor dit ladingstransport plaatsvindt slechts enkele nanometers dik is, kost dit transport enkele picoseconden en gedurende die tijd is het stukje materiaal, waar de ladingsdragers geëxciteerd zijn, feitelijk losgekoppeld van de externe spanningsbron. In de Monte Carlo simulaties is dit ingevoerd als een tijdsconstante die bepaalt hoe lang het duurt voordat het veld dat geheel of gedeeltelijk ingestort is weer de initieel aangelegde waarde heeft.

Als nu het aantal geëxciteerde ladingsdragers veel groter is dan het aantal op de negatieve metalen elektrode, kan een overshoot optreden, waardoor het syteem van positieve en negatieve ladingsdragers gaat oscilleren. Dit zijn plasma oscillaties. Deze hebben een frequentie van rond de 7 THz. De frequentie van bulk phononen in GaAs is ongeveer even groot en een koppeling van de plasma oscillaties met de phononen zal optreden. Dit is al heel lang bekend, doch werd tot nu toe slechts op een fenomenologische manier beschreven en is nog niet eerder in Monte Carlo simulaties ingebouwd. In de Monte Carlo simulaties is deze koppeling in de bewegingsvergelijkingen ingebouwd op een fundamentele manier. De vierde sectie van hoofdstuk 3 beschrijft kort het verschijnsel optische tweede harmonische generatie en meer uitgebreid de elektrisch veld geïnduceerde SHG. Dit is de basis voor het direct detecteren van de tijdsafhankelijkheid van het elektrische veld aan het Schottky barrière grensvlak na excitatie van de ladingsdragers.

In hoofdstuk 4 worden anisotropie experimenten beschreven waarbij alleen een probebundel wordt gebruikt en geen excitatiebundel. Door middel van deze metingen kunnen de verschillende bijdragen aan het SHG signaal gescheiden worden. Bij deze metingen wordt de extern aangelegde spanning gevarieerd om te bepalen of, en hoe, het SHG signaal gevoelig is voor het elektrische veld aan het Schottky barrière grensvlak. Uit deze metingen blijkt dat een bepaalde component van het signaal evenredig is met het elektrische veld. Deze component kan gemeten worden door de juiste polarisatie van de laserbundels te kiezen en door de kristalassen van het preparaat ook de juiste oriëntatie ten opzichte van de laserbundels te geven.

Hoofdstuk 5 beschijft experimenten waarin een probebundel en een excitatiebundel worden gebruikt, waarbij de tijdvertraging zeer nauwkeurig geregeld wordt. In deze experimenten is de excitatiedichtheid gevarieerd, maar zijn de dichtheden relatief laag gehouden. Ook is de spotdiameter gevarieerd. De resultaten van deze experimenten zijn vergeleken met de resultaten van de Monte Carlo simulaties om het concept van de tijdsconstante te checken, en de grootte van deze ontkoppelingsconstante te bepalen.

In hoofdstuk 6 tenslotte worden tijdsopgeloste experimenten gepresenteerd waarbij de excitatiedichtheid veel hoger is dan in hoofdstuk 5. Het resultaat is dat oscillaties waargenomen worden in het SHG signaal ten gevolge van de plasma oscillaties. Het bijzondere hiervan is dat de plasma oscillaties direkt in het tijddomein gemeten zijn.

Deze oscillaties zijn ook weer vergeleken met de Monte Carlo simulaties. In deze simulaties is de in hoofdstuk 5 bepaalde tijdsconstante de enige vrije parameter. De oscillaties in het elektrische veld die door de Monte Carlo simulaties berekend worden komen perfekt overeen met de gemeten oscillaties in het SHG signaal. Door middel van Fourier analyse is de frequentie van de gemeten en berekende oscillaties bepaald als functie van de excitatiedichtheid. Wanneer in de Monte Carlo simulaties de plasmon phonon koppeling wordt meegenomen, is de overeenkomst tussen experiment en simulatie zeer goed.

De slotconclusie is dat tijdsopgeloste SHG een nuttige techniek is om het tijdsafhankelijke elektrische veld aan een metaal halfgeleider grensvlak te meten. Ook beschrijft het gebruikte model in de Monte Carlo simulaties het onderhavige systeem heel goed.

Curriculum vitae

Willem de Jong

geboren op 28 oktober 1969 te Stolwijk

1982 - 1988		Ongedeeld VWO op scholengemeenschap ’De Driestar’ te Gouda.
1988 - 1993		Studie Technische Natuurkunde aan de Technische Universiteit Delft.
	31 - 8 - 1989	Propedeutische examen.
	1 - 2 - 1991	Start afstudeeronderzoek in de subsectie ’halfgeleiders’ van de vakgroep ’Vaste Stof Supergeleiding’. Afstudeeronderwerp: ’Geleidings spectroscopie aan een kleine quantumdot in het Coulomb regime’.
	2 - 3 - 1993	Doctoraal examen.
1993 - 1997		In dienst van de Stichting FOM als Onderzoeker in Opleiding. Promotiewerk aan de Katholieke Universiteit Nijmegen, op de afdeling ’Experimentele Vaste-Stoffysica 2’ onder begeleiding van Prof. dr. Th.H.M. Rasing.
1997		Wetenschappelijk medewerker in de groep ’Elektro optische propagatie en signatuurmanagement’ van het TNO Fysisch en Elektronisch Laboratorium te Den Haag.

List of publications

- *Zero-Dimensional States and Single Electron Charging in Quantum Dots*, A.T. Johnson, L.P. Kouwenhoven, W. de Jong, N.C. van der Vaart, C.J.P.M. Harmans, and C.T. Foxon, Phys. Rev. Lett. **69**, 1592 (1992).

- *Charging effects in quantum dots at high magnetic fields*, N.C. van der Vaart, A.T. Johnson, L.P. Kouwenhoven, D.J. Maas, W. de Jong, M.P. de Ruyter van Steveninck, A. van der Enden, C.J.P.M. Harmans, and C.T. Foxon, Physica B **189**, 99 (1993).

- *Interface Magnetism and Possible Quantum Well Oscillations in Ultrathin Co/Cu Films Observed by Magnetization Induced Second Harmonic Generation*, H.A. Wierenga, W. de Jong, M.W.J. Prins, Th. Rasing, R. Vollmer, A. Kirilyuk, H. Schwabe and J. Kirschner, Phys. Rev. Lett. **74**, 1462 (1995).

- *Nonlinear and linear Kerr studies of Co/Cu multilayers*, H.A. Wierenga, W. de Jong, M.W.J. Prins, Th. Rasing, R. Vollmer, A. Kirilyuk, H. Schwabe, and J. Kirschner, Surf. Sci. **331-333**, 1294 (1995).

- *Electric field dynamics at a metal-semiconductor interface probed by femtosecond optical second harmonic generation*, W. de Jong, A.F. van Etteger, C.A. van 't Hof, P.J. van Hall, and Th. Rasing, Surf. Sci. **331-333**, 1372 (1995).

- *Direct comparison of nonlinear and linear Kerr-effect measurements on thin Co films on Cu(001)*, R. Vollmer, A. Kirilyuk, H. Schwabe, J. Kirschner, H.A. Wierenga, W. de Jong, and Th. Rasing, J. Magn. Magn. Mater. **148**, 295 (1995).

- *Electric field induced second harmonic generation spectroscopy on a metal-oxide-silicon structure*, P. Godefroy, W. de Jong, C.W. van Hasselt, M.A.C. Devillers and Th. Rasing, Appl. Phys. Lett. **68**, 1981 (1996).

- *Nonlinear magneto-optical Kerr effect study of quantum-well states in a Au overlayer on a Co(0001) thin film*,
  M. Groot Koerkamp, A. Kirilyuk, W. de Jong, Th. Rasing, J. Ferré, J.P. Jamet, P. Meyer and R. Mégy, J. Appl. Phys. **79**, 5632 (1996).

- *Generation of resonant second harmonic in multiple Si/SiO$_2$ quantum wells*,
  O.A. Aktsipetrov, A.N. Rubtsov, A.V. Zayats, W. de Jong, C.W. van Hasselt, M.A.C. Devillers, Th. Rasing and E.D. Mishina, Zh. Éksp. Teor. Fiz. **109**, 1240 (1996), *ibid.* JETP **82**, 668 (1996).

- *Time-resolved optical second harmonic generation study of the electric field dynamics at a metal-semiconductor interface*,
  W. de Jong, A.F. van Etteger, C.A. van 't Hof, P.J. van Hall, and Th. Rasing, Surf. Sci. **352-354**, 807 (1996).

- *Electric Field Dynamics at a Metal-Semiconductor Interface Probed by Time Resolved Femtosecond Optical Second Harmonic Generation*,
  W. de Jong, A.F. van Etteger, C.A. van 't Hof, P.J. van Hall, and Th. Rasing, in *Ultrafast Processes in Spectroscopy*, edited by O. Svelto, S. De Silvestri and G. Denardo (Plenum Press, New York, 1996), p.659-662.

- *Coherent plasmon-surface phonon oscillations in a GaAs Schottky barrier sample*,
  W. de Jong, A.F. van Etteger, P.J. van Hall, and Th. Rasing, Surf. Sci. **377-379**, 355 (1997).

- *Coherent Plasmon-Phonon Oscillations in a GaAs Schottky-Barrier Sample*,
  P.J. van Hall, W. de Jong, A.F. van Etteger, and Th. Rasing, Phys. Stat. Sol. B. **204**, 91 (1997).

- *Quantum-Confined Effects for Electron-States in Si/SiO$_2$ Quantum-Wells and 2nd-Harmonic Generation Spectroscopy*,
  O.A. Aktsipetrov, P.V. Elyutin, E.V. Malinnikova, E.D. Mishina, A.N. Rubtsov, W. de Jong, and Th. Rasing, Dokl. Akad. Nauk **355**, 178 (1997).

- *Coherent Plasmon-Phonon Oscillations in a GaAs Schottky Barrier Sample*,
  P.J. van Hall, W. de Jong, and Th. Rasing, in preparation.